

MASTER THESIS

# Plasticity and fracture modeling of composite steel Tribond 1200 for crash simulation



*Author:*

**K.A. RAMAKER**

Faculty of Engineering Technology (CTW)

Department of Mechanics of Solids, Surfaces & Systems (MS3)

Chair Nonlinear Solid Mechanics

*Graduation committee:*

Prof. Dr. Ir. A.H. van den Boogaard

Dr. Ir. J. Hazrati

Dr. Ir. D.T.A. Matthews

Dr. Ir. T.K. Eller

Document number: CTW.16/TM-5786

Enschede, December 7, 2016

**UNIVERSITY OF TWENTE.**

CONFIDENTIAL

CONFIDENTIAL

MASTER THESIS

# Plasticity and fracture modeling of composite steel Tribond 1200 for crash simulation

**UNIVERSITY OF TWENTE.**

**VOLKSWAGEN**

AKTIENGESELLSCHAFT

Kenneth Anthony Ramaker  
Enschede, December 7, 2016

Graduation committee:

Prof. Dr. Ir. A.H. van den Boogaard

University of Twente

Dr. Ir. J. Hazrati

University of Twente

Dr. Ir. D.T.A. Matthews

University of Twente

Dr. Ir. T.K. Eller

Volkswagen AG

CONFIDENTIAL

CONFIDENTIAL

# Declaration of confidentiality

Publications of the content of this thesis are not allowed without the prior written permission of Volkswagen AG. The results, opinions and conclusion of this thesis are not necessarily those of Volkswagen AG. This thesis shall only be made accessible to the employees of Volkswagen Group, the correctors and the members of the examination committee. Publication or forwarding the thesis, except evaluation within the Master-examination, outside of the Volkswagen AG is not permitted.

# Zustimmungsvorbehalt

Veröffentlichungen über den Inhalt der Arbeit sind nur mit schriftlicher Genehmigung der Volkswagen AG zugelassen. Die Ergebnisse, Meinungen und Schlüsse dieser Abschlussarbeit sind nicht notwendigerweise die der Volkswagen AG. Die vorliegende Arbeit ist nur den Mitarbeitern des Volkswagen Konzerns, den Korrektoren sowie den Mitgliedern des Prüfungsausschusses zugänglich zu machen. Eine Veröffentlichung oder Weitergabe der Abschlussarbeit, außer zur Bewertung im Rahmen der Master-Studienprüfung, außerhalb der Volkswagen AG ist nicht erlaubt.

CONFIDENTIAL

# Summary

The material Tribond 1200 uses a new development in steel manufacturing and provides a new approach to hot forming. It is a composite steel which combines high ductility and high strength in one material. Composite steel sheets are created by rolling different steel blanks together. These steel grades have different mechanical properties after hot forming. Hot forming is a heat treatment process in which steel sheets are first heated and then simultaneously formed and quenched. The automotive industry is investigating Tribond for its use in crash critical components, in the hopes of further reducing vehicle weight whilst maintaining crashworthiness. For this purpose, an accurate predictive model is required which describes the elastic, plastic and fracture behavior of Tribond.

A set of mechanical tests were performed to investigate the materials plastic and fracture behavior. The test set consisted of in-plane and out-of-plane loading of different specimens. Full-Tribond specimens were extracted from press hardened sheets of Tribond. Special core-only specimens were also fabricated by removing material from the top and bottom surface of full-Tribond specimens until only the core layer steel was left. Further material testing concentrated on strain and hardness measurements and metallography. From strain and hardness measurements, weak spots were found in the steel sheets, which caused premature necking and fracture in uni-axial tensile tests. With microscopy, fracture initiation was investigated in out-of-plane bending specimens.

The experimental results are used to calibrate a hardness-driven material model for Tribond. The materials plastic and fracture properties through the thickness are defined by the hardness. Material models are calibrated for the extreme values of the average hardness curve, so called core and surface layer models. A mixing rule is used to define the material models for all interpolated hardness values, these are the transition zone models. The plasticity model is defined by a stress-strain relationship or hardening curve. For the core layer, it is calibrated from the experimental results of core-only specimens. Experimental results of full-Tribond specimens are used to calibrate the plastic material model for the surface layer, assuming a linear relation between the hardness and hardening properties in the transition zone. The fracture model is defined by the modified Mohr-Coulomb (mMC) fracture surface. The core and surface layer fracture models are calibrated from experimental results of full-Tribond specimens. The transition zone fracture models are specified by a non-linear relationship between the hardness and fracture properties. Besides calibrating the fracture behavior for a 0.1 mm mesh, the Tribond fracture model is calibrated to account for mesh sizes of 0.2 mm and 0.5 mm. These coarser mesh sizes are more desirable in crash simulations. Different mesh sizes needed to be calibrated because the fracture model is strain-based and the strains are dependent on the mesh size.

The calibrated hardness-driven material model is validated with an L-section compression test. The test is simulated with different mesh sizes of 0.1 mm, 0.2 mm and 0.5 mm. This is done to investigate the influence of the hardness mapping through the thickness and the accuracy of the mesh size dependent fracture model. The simulations showed the material model gives a good prediction of the force-displacement curves and deformation modes for all mesh sizes.

CONFIDENTIAL

# Samenvatting

Het materiaal Tribond 1200 gebruikt een nieuwe ontwikkeling in staalproductie en biedt een nieuwe methode voor het warmomvorm proces. Het is een composiet staal die hoge ductiliteit en treksterkte combineert in één materiaal. Composiet staalplaten worden gemaakt door het op elkaar walsen van verschillende staalsoorten, die verschillende mechanische eigenschappen hebben na het warmomvorm proces. Het warmomvormen proces is een warmtebehandeling waarbij staalplaten worden verhit en vervolgens gelijktijdig worden gevormd en afgeschrikt. De auto-industrie onderzoekt Tribond wegens de toepasbaarheid in crash kritische componenten, in de hoop het gewicht van voertuigen verder te verminderen bij behoud van crashbestendigheid. Hiertoe is een voorspellend model vereist die het elastische, plastische en breuk gedrag van Tribond kan omschrijven.

Een reeks mechanische testen werden uitgevoerd om het materiaal gedrag te onderzoeken. De testen belasten verschillende materiaal specimens met krachten in- en uit-het-vlak van de plaat. Vol-Tribond specimens werden geëxtraheerd uit druk geharde Tribond platen. Puur-kern specimens werden vervaardigd door het verwijderen van materiaal van de bovenkant en onderkant van vol-Tribond specimens, totdat alleen de kernlaag van de staalplaat overbleef. Verdere materiaal testen concentreerden op rek en hardheidsmetingen en metallografie. Bij de rek- en hardheidsmetingen werden zwakke plekken aangetroffen in de staalplaten, die veroorzaakten vroegtijdige insnoering en breuk in uni-axiaal trekproeven. Met microscopie, werd breuk initiatie onderzocht in uit-het-vlak buig testen.

De experimentele resultaten worden gebruikt om een hardheids-gedreven materiaalmodel voor Tribond te kalibreren. De materiaal eigenschappen voor plastisch en breuk gedrag door de dikte van het materiaal worden bepaald door de hardheid. Modellen worden gekalibreerd voor de uiterste hardheidswaarden door de dikte, de zogenaamde kernlaag en oppervlaktelaag modellen. Een mengregel wordt gebruikt om de materiaalmodellen te definiëren voor tussen liggende hardheidswaarden, dit zijn de overgangszone modellen. Het plasticiteitsmodel wordt gedefinieerd door een spanning–rek relatie of verhardingscurve. Het materiaalmodel van de kernlaag wordt gekalibreerd met puur-kern specimens. De experimentele resultaten van vol-Tribond specimens worden gebruikt om het plastische gedrag van de oppervlaktelaag te kalibreren, hierbij worst uitgegaan van een lineaire relatie tussen de hardheid en verharding in de overgangszone. Het breukmodel wordt gedefinieerd door de modified Mohr–Coulomb fracture surface. De kernlaag en oppervlaktelaag breukmodellen zijn gekalibreerd met de experimentele resultaten van vol-Tribond specimens. De overgangszone breukmodellen worden gespecificeerd door een niet-lineaire relatie tussen de hardheid en het breukgedrag. Naast het kalibreren van het breukgedrag voor een 0.1 mm eindig-element-net, wordt het Tribond breukmodel ook gekalibreerd om rekening te houden met verschillende elementgroottes van 0.2 mm en 0.5 mm. De grotere elementgrootte zijn wenselijk in crash simulaties. Verschillende elementgroottes moesten ook gekalibreerd worden, omdat het breukmodel op de rek is gebaseerd en de rek op zijn beurt weer van de elementgrootte afhangt.

Het gekalibreerde hardheids-gedreven materiaalmodel is gevalideerd met een L-sectie compressie test. De test wordt gesimuleerd met verschillende elementgroottes, namelijk 0.1 mm, 0.2 mm and 0.5 mm. Dit wordt gedaan om te onderzoeken wat de invloed van de hardheidsmapping door de dikte is en wat de nauwkeurigheid van het elementgrootte afhankelijke breukmodel is. De simulaties toonden dat het materiaalmodel een goede voorspelling geeft van de kracht–verplaatsingscurven en vervormingsmodi voor alle elementgroottes.

CONFIDENTIAL

# Nomenclature

The symbols used in this thesis are classified in a Greek and Roman category. Some symbols appear more than once, their specific meaning follows from their context or from sub- and/or superscripts.

## Greek Symbols

$\alpha_{\text{shape}}$	shape parameter in the non-linear mixing rule of the hardening model
$\alpha_{\text{V}}$	Voce hardening law fraction, linear mixing parameter
$\varepsilon$	true strain
$\varepsilon_{0,\text{S}}$	initial strain in Swift hardening law
$\varepsilon_{0,\text{V}}$	initial strain in Voce hardening law
$\bar{\varepsilon}$	true equivalent strain
$\epsilon$	engineering strain
$\lambda_{\text{final}}$	final fraction in the non-linear mixing rule
$\lambda_{\text{initial}}$	initial fraction in the non-linear mixing rule
$\lambda_{\text{V}}$	Voce hardening law fraction, non-linear mixing parameter
$\sigma$	true stress
$\sigma_{\text{eng}}$	engineering stress
$\sigma_{\text{m}}$	mean stress
$\sigma_{\text{S}}$	true stress in the Swift hardening law
$\sigma_{\text{V}}$	true stress in the Voce hardening law
$\sigma_{\text{y}}$	yield stress
$\bar{\sigma}$	true equivalent stress

## Roman Symbols

$A$	cross section
$c_{1-4}$	four parameters of the modified Mohr–Coulomb fracture criterion
$d$	displacement
$D$	damage indicator
$F$	force
$HV$	Vickers hardness value
$k_{\text{S}}$	factor in the Swift hardening law
$k_{\text{V}}$	factor in the Voce hardening law

$l$	length
$l_0$	initial gauge length
$n_S$	exponent in the Swift hardening law
$n_V$	exponent in the Voce hardening law
$r$	Lankford coefficient
$t$	thickness

### Sub/superscripts

ax	in axial direction
t	in thickness direction
e	elastic
ep	end point
exp	experiment
p	plastic
w	in width direction
max	maximum
Rp0.2	offset proportional limit of 0.2 % (similar for 0.05 % and 0.1 %)
sim	simulation
tz	transition zone

### Abbreviations

A	austenite
AlSi	aluminum-silicon
AS	aluminum-silicon (ThyssenKrupp)
B	bainite
BB1.5	buckling bending, narrow (1.5 mm) specimen test
BB20	buckling bending, wide (20 mm) specimen test
BCC	body-centered cubic
BE1.5	3-point bending, narrow (1.5 mm) specimen test
BE20	3-point bending, wide (20 mm) specimen test
BT	bulge test
CCT	continuous cooling transformation
CH	central hole tensile test
CPU	central processing unit
DIC	digital image correlation
F	ferrite
FCC	face-centered cubic

---

FE	finite element
FEM	finite element method
HFS	hot formed structure (ThyssenKrupp)
M	martensite
mMC	modified Mohr–Coulomb
MMM	modular material model
NT	notched tensile test
P	pearlite
PIP	parameter identification procedure
SD	standard deviation
SH	shear test
SRI	selective reduced integration
URI	uniform reduced integration
UT	uni-axial tensile test
UTS	ultimate tensile strength
UHSS	ultrahigh-strength steel

CONFIDENTIAL

# Contents

<b>Summary</b>	<b>vii</b>
<b>Samenvatting</b>	<b>ix</b>
<b>Nomenclature</b>	<b>xi</b>
<b>1 Introduction</b>	<b>1</b>
1.1 Context and motivation . . . . .	1
1.2 Objective and scope . . . . .	1
1.3 Outline . . . . .	2
<b>2 Theory</b>	<b>5</b>
2.1 Introduction . . . . .	5
2.1.1 Production process . . . . .	5
2.1.2 Material description . . . . .	5
2.1.3 Hot forming . . . . .	5
2.2 Material modeling . . . . .	7
2.2.1 Yield criterion . . . . .	8
2.2.2 Hardening . . . . .	9
2.2.3 Fracture model . . . . .	12
2.2.3.1 Stress triaxiality and Lode angle parameter . . . . .	12
2.2.3.2 mMC Fracture surface . . . . .	12
2.2.3.3 Damage evolution rule . . . . .	13
<b>3 Experimental work</b>	<b>15</b>
3.1 Initial Metallographic analysis and hardness measurements . . . . .	15
3.2 Mechanical tests . . . . .	15
3.2.1 Uni-axial tensile test . . . . .	17
3.2.2 Notched tensile test . . . . .	18
3.2.3 Central hole tensile test . . . . .	20
3.2.4 Bulge test . . . . .	20
3.2.5 Shear test . . . . .	21
3.2.6 3-Point bending test . . . . .	23
3.2.7 Buckling bending test . . . . .	23
<b>4 Material modeling</b>	<b>29</b>
4.1 Modeling strategy . . . . .	29
4.2 Plasticity model . . . . .	31
4.2.1 Yield criterion . . . . .	31
4.2.2 Hardening law . . . . .	32
4.2.2.1 Core layer . . . . .	32
4.2.2.2 Surface layer . . . . .	36
4.3 Fracture model . . . . .	41
4.3.1 Fracture modeling strategy . . . . .	41
4.3.2 Core layer . . . . .	41
4.3.3 Surface layer . . . . .	44

4.3.4	Mesh size dependency . . . . .	50
<b>5</b>	<b>Model validation</b>	<b>53</b>
5.1	Experimental work . . . . .	53
5.2	Simulation results . . . . .	53
5.3	Comparison of the deformation modes and fracture . . . . .	56
<b>6</b>	<b>Conclusion and recommendations</b>	<b>59</b>
6.1	Conclusion . . . . .	59
6.2	Recommendations . . . . .	61
<b>A</b>	<b>Determination of the Lankford coefficients</b>	<b>63</b>
<b>B</b>	<b>Determination of the true stress–true equivalent plastic strain</b>	<b>65</b>
<b>C</b>	<b>Specimen drawings</b>	<b>67</b>
<b>D</b>	<b>Test setup images</b>	<b>69</b>
<b>E</b>	<b>Stress state traces of the BE20 test</b>	<b>71</b>
<b>F</b>	<b>Fracture plots</b>	<b>75</b>
<b>G</b>	<b>Fracture models</b>	<b>81</b>
<b>H</b>	<b>Side-by-side comparison L-section compression test</b>	<b>83</b>
	<b>Bibliography</b>	<b>85</b>
	<b>Acknowledgements</b>	<b>87</b>

# Chapter 1

## Introduction

### 1.1 Context and motivation

Car manufacturers are continuously looking to improve the overall performance of their products. The Volkswagen Group is in this respect no different. With its “TOGETHER - strategy 2025” future program, they want to become a global leading provider of sustainable mobility. This is a very general performance measure, more specifically this may be interpreted as a desire to decrease vehicle emissions. This work focuses on doing this by decreasing vehicle weight whilst maintaining crashworthiness. As a result, car manufacturers, and by extension their suppliers, are continuously searching for new and innovative materials. One such innovation is the manufacturing of composite steels. ThyssenKrupp Steel Europe is a leading steel manufacturer, continually innovating in the field of flat steels. With their development of composite steels, they can produce steels with “conflicting properties”. One such composite steel is Tribond, which combines ultrahigh-strength and ductile steel grades. The automotive industry is interested in this material for use in crash critical components. With the combined properties, high-strength and excellent bending, Tribond could replace other steels in light-weight vehicle manufacturing. Research is required to see if the use of Tribond would reduce vehicle weight whilst maintaining crashworthiness.

Tribond owes its mechanical properties to hot forming, a process which is currently used to fabricate crash critical components like A- and B-pillars, bumper beams and door intrusion beams, see Figure 1.1. With this heat treatment, boron steel blanks are formed and quenched into components with martensitic crystal structures. The ultimate tensile strength of these steels can increase from an initial 600 MPa to 1500 MPa. The composite steel Tribond is composed of different steel grades, with different hardenability, which have varying strength and ductility. In Tribond, these varying properties are arranged such as to retain the strength properties and also increase the ductility in bending over conventional ultrahigh-strength steels. Thereby, the combined properties in the composite steel Tribond extend the range of possible applications of ultrahigh-strength steels. The steel is suitable for use in crash critical components which show a lot of bending.

Research into the material Tribond is divided within the Volkswagen Group over multiple departments. The Volkswagen Group Research is mainly concerned with calibrating an accurate predictive model which describes Tribond’s elastic, plastic and fracture behavior. Other departments are concerned with crash simulations and deciding on whether or not the material will be implemented in the manufacturing of light-weight vehicles. This thesis is part of the ongoing calibration of the predictive model for use in crash simulation.

### 1.2 Objective and scope

The objective of this master thesis is to calibrate a hardness-driven material model of Tribond 1200 for use in crash simulations. The composite steel Tribond 1200 possesses varying properties through the thickness. These varying properties will be related to the materials hardness properties. This means the elastic, plastic and fracture behavior need to be accurately predicted for all hardness values. The main focus is the detailed modeling of the materials behavior with solid elements. It will be used to model virtual experiments from which a material model for shell elements can be derived. Shell element modeling is outside of the scope of this work.

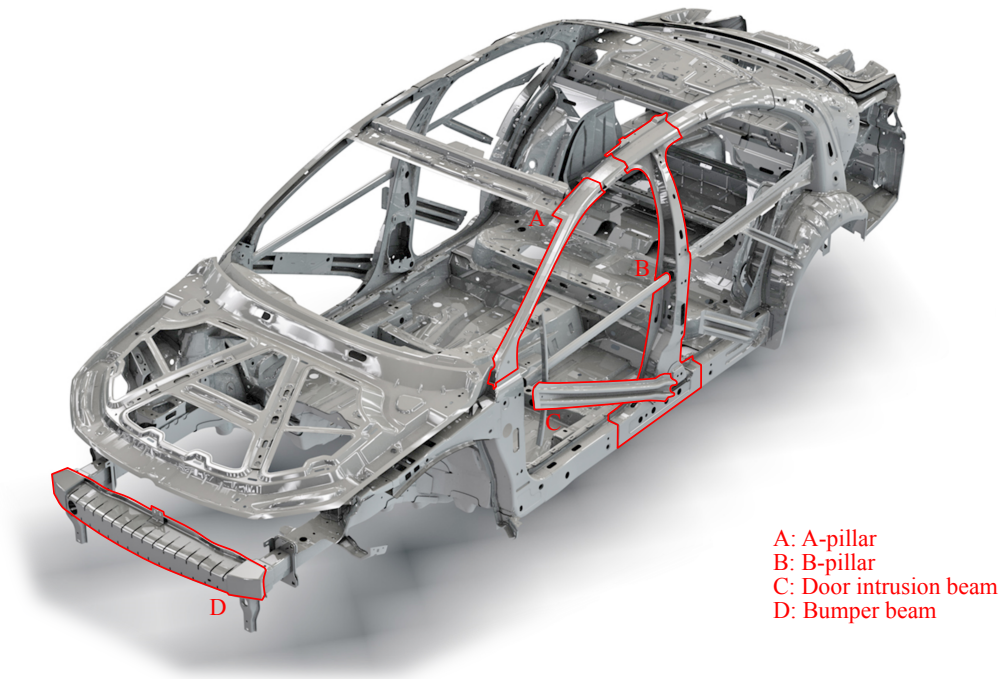


**Figure 1.1** *Volkswagen Jetta Body in White with highlighted crash critical components.*

An important factor in the calibration is the varying properties through the thickness of the material. Accurately modeling the through thickness properties of Tribond requires distinct material models for individual layers in the material. These layers are distinguished between according to their hardness values. With experimental results, the material behavior is studied and the hardness-driven model is calibrated. The material model will predict elastic behavior up to yielding, with a yield criterion to describe the point at which plastic deformation begins for different stress states. The plastic deformation must be accurately represented by a hardening curve, which specifies the stress–strain relationship. From the simulated stress state traces, the modified Mohr–Coulomb fracture criterion is calibrated. This in turn is used to define the damage accumulation due to plastic deformation. The model must define the material behavior in the case of complex loading experienced during a crash. This is validated in a validation test, which experiences complex loading.

Tribond 1200 is a hot formed steel. Different hot forming production process parameters such as the heat treatment temperature and cooling rate are proven to have a large influence on steel properties. The heating and quenching time will influence the materials hardness and ductility. These factors are outside of the scope of this work, because of the limited amount of prototype material available. Also, this prototype material had already been heat treated, not allowing for a second heat treatment.

### 1.3 Outline

This report details the experimental work, modeling and validation of Tribond 1200. It also discusses the background information to understanding the material behavior and modeling technique.

The theoretical background of this work is discussed in Chapter 2. It describes the hot forming process in general and the press hardening of the used Tribond steel sheets. The fundamentals of the material modeling process are also described, distinguishing between different yield criteria and with a description on how to model the plastic and fracture behavior. The current modeling processes within the parameter identification procedure (PIP) developed by the Volkswagen Group Research are also described.

The experimental work done to characterize the mechanical behavior of Tribond and generate data for the calibration of a material model are discussed in Chapter 3. It contains hardness measurements, metallographic studies and a set of mechanical tests performed to understand the behavior of Tribond under different load cases and stress states.

The material modeling is discussed in Chapter 4, which details the hardness-driven model and the calibration of the plasticity and fracture models. The section about the plasticity model details the core and surface layer calibration methods and results. The section about the fracture model details its calibration for the core and surface layer and shows different hardness-driven mixing rules used to define the fracture models for the interpolated hardness values.

The validity of the calibrated model is investigated in an L-section compression test, which is described in Chapter 5. Included are a description of the experimental results, the simulation approach and the validation results.

Chapter 6 concludes this work with an overview of important conclusions and recommendations. It also describes the future work required to further improve the material model.

CONFIDENTIAL

# Chapter 2

## Theory

In this chapter, the material Tribond and its forming process are introduced as well as the standard modeling method used by the Volkswagen Group Research.

### 2.1 Introduction

ThyssenKrupp Steel Europe is a worldwide leading supplier of high-grade flat steel. One recent innovation is the manufacturing of composite steels. ThyssenKrupp has many different prototype composite steels. Examples are Duobond, Tribond, Pentabond and Multibond, which have respectively two, three, five and multiple layers of different steels with a wide range of individual layer thicknesses [9].

#### 2.1.1 Production process

ThyssenKrupp's composite steel manufacturing process uses slabs of different metals rolled together to make one sheet. The slabs are bonded together during the hot rolling process. Before rolling, there is no bond between the different metals. The first mechanical adhesion occurs through interlocking as the material is forced between the rollers. Through lengthening of the material, new, highly reactive contact areas are created. During and after rolling these areas form a metallic bond by diffusion, recrystallization and recovery [9].

#### 2.1.2 Material description

Tribond has three layers made of two different steel types. The ductile surface layers consists of MBW 500 and the ultrahigh-strength core layer of MBW 1500, also known as 22MnB5. The chemical compositions of the two steel types are given in Table 2.1. ThyssenKrupp offers Tribond 1400 and Tribond 1200 for use in car body parts. The difference between these two grades is the ductile to ultrahigh-strength steel ratios. Tribond 1400 has a 10% – 80% – 10% distribution and Tribond 1200 has a 20% – 60% – 20% distribution [3]. The numerical values in the naming refer to the ultimate tensile strength of the composite steel after hot forming in MPa. With a larger ultrahigh-strength steel core layer fraction, the Tribond 1400 has a higher ultimate tensile strength than Tribond 1200. The composite steel sheets used in this work have a thickness of 1.5 mm and are in the press hardened state. The sheets have an Aluminum-Silicon coating (AlSi) to protect them against scale formation and decarburization, during hot forming. The coating also offers basic corrosion protection after hot forming [2].

The material considered in this thesis is Tribond<sup>®</sup> Car HFS V15H20+AS. ThyssenKrupp uses naming variations like V15H10 and V15H20, for Tribond 1400 and Tribond 1200, respectively. The material considered in this report is referred to as Tribond 1200 or simply Tribond.

#### 2.1.3 Hot forming

Hot forming or hot stamping is a process in which steel blanks are heated up to the austenization temperature and then simultaneously formed and quenched in an actively cooled die [24]. Its advantages over cold forming are higher shape accuracy and improved high strength properties of the final product. Shape accuracy of the final product after forming is increased as a result of less springback. The mechanical properties of

**Table 2.1** Tribond's core and surface layer chemical compositions (wt%) [3].

	C	Si	Mn	P	S	Al	Nb	Ti	Cr+Mo	B
	max.	max.	max.	max.	max.	min.	max.	max.	max.	max.
Ultrahigh-strength core layer	0.25	0.40	1.40	0.025	0.010	0.015	–	0.05	0.50	0.005
Ductile surface layers	0.10	0.35	1.00	0.030	0.025	0.015	0.10	0.15	–	0.005

hot formed steels are well suited for use in crash critical car components, because of their high intrusion resistance. Recent developments also allow tailoring of the quenching process and thereby the mechanical properties within a single part. By not hardening certain areas during the hot forming process, the steel remains ductile. This in turn has led to the development of Tribond.

Tribond composite steel is not only a material advancement, but also introduces a new approach to hot forming [3]. The current hot forming approach is to increase the tensile strength of a complete product. Take for example the widely used hot forming steel 22MnB5, its tensile strength increases from 600 MPa to 1500 MPa after hot forming. As mentioned above, tailored hot forming approaches introduce areas of lower strength and improved ductility in a monolithic steel product to enhance its crashworthiness. Figure 2.1 shows a possible application: a B-pillar tailored for optimal performance in a side crash, with a high strength top section for high intrusion resistance and a ductile bottom section for high energy absorption. Two common hot forming methods in which these tailored components can be created are differential heating in the furnace, thereby not fully austenitizing the part, and varying in-die cooling rates during forming [15]. Both examples partially prevent forming of martensite in the product, resulting in different mechanical properties throughout a monolithic steel. The resulting products have both high strength and high ductility, only these properties occur in different sections of the part, in this case the top and bottom sections of the B-pillar.

The new hot forming approach suggested by ThyssenKrupp is to combine these “conflicting properties” in the same section of a product. These products have both high strength and high ductility throughout, unlike tailored products with locally weaker, more ductile sections. The hot forming process does not change, instead the new approach depends on the ability of a composite steel to have different steel grades with different hardenability throughout its cross section. It is the carbon content, which determines the materials strength and the boron content, and somewhat less so the manganese and chromium content, which determine the ability of a steel to form martensitic crystal structures with technically feasible cooling rates [24]. Lowering the boron content decreases the materials ability to form martensite during quenching, meaning it will harden less. By creating a sandwich of two materials with different hardenability, a single material is created with seemingly conflicting properties. In the case of Tribond, a high strength core gives a high yield strength and the ductile surface layers allow for large bending angles before fracture.

For hot forming, a steel blank is first austenitized. This is done by heating the material to above its austenitization temperature and keeping it hot to assure a fully austenitic phase transformation. In the case the steel is coated with AlSi, it is kept at high temperatures for at about 5 min to ensure the aluminum diffuses into the base steel. In this process a protective Fe–Al alloy layer is created to stop scale formation on the surface of the steel sheet [29]. After a dwell time in the furnace, the sheet is quickly transferred from the furnace to the cooled forming die to quench the part. After a holding period to complete the quench, the sheet is removed. If the cooling rates are high enough, the metal will have fully hardened, by forming a martensitic microstructure.

The 1.5 mm thick Tribond sheets used in this work were austenitized at a furnace temperature of 950 °C with a dwell time of 6 min. After removing the blank from the furnace, it was manually moved to the forming press in 8 – 10 sec. The forming press applied a force of 2000 kN in a flat die and quenched the Tribond for 20 sec. The cooling curve of the blank is superimposed on the CCT-diagram of 22MnB5, see Figure 2.2. The measured temperature data was obtained from the furnace and Tribond sheet surface during the holding time in the flat die. No temperature data is known during the transfer time between the furnace and the press, this can however be estimated. The cooling rate was estimated assuming a lumped system cooled by convection and radiation. According to ThyssenKrupp [4], to properly hot form Tribond, the sheets must be austenitized at 920 °C and cooled faster than the critical cooling rate of 27 °C s<sup>-1</sup>. This critical cooling curve and the cooling curve of the blank are shown in Figure 2.2. It is important to note that, the time-axis starts at 1 sec and that no cooling transformation temperature, below which the austenite phase is unstable,

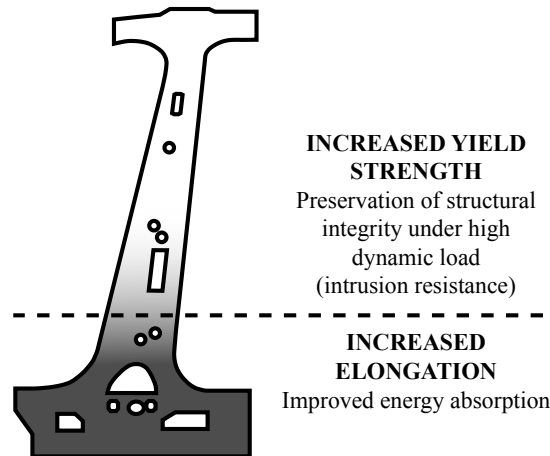


**Figure 2.1** Schematic view of a tailor hardened B-pillar, adapted from [15].

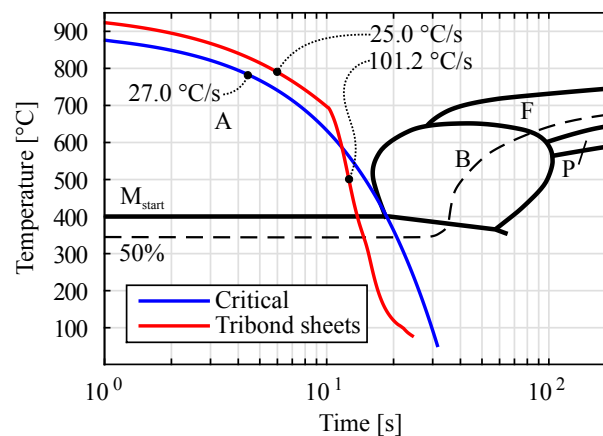


**Figure 2.2** CCT-diagram for 22MnB5 with two cooling curves superimposed upon it.

is known for Tribond. Therefore, both cooling curves start at their maximum temperature of 950 °C and 920 °C.

According to ThyssenKrupp [9], the composite steel sheets before hot forming had a small transition zone of 60  $\mu\text{m}$ . The hot forming process will cause further diffusion in a composite steel between the different steels. Micrographs of an etched specimen before and after hot forming were shown by the manufacturer, see Figure 2.3. In this figure, the etching before hot forming shows a very abrupt transition between the surface and core layer. After hot forming, the transition zone seems to have increased in thickness reducing the surface layer thickness. The dark etch hinders investigation into the change of the core layer thickness. After the hot forming process, the protective Fe–Al alloy layer has formed. Chapter 3 contains a hardness measurement through the thickness, illustrating the increase of the transition zone size for the above described hot forming process (Figure 3.2).

## 2.2 Material modeling

For crash simulations, a material model must accurately represent the elasto-plastic and fracture behavior of a material. A brief description of the theoretical background concerning the material model is given here. First, the yield criterion is described, which defines the stress states where the strains become irreversible. Secondly, strain hardening is described, which explains the yield stress evolution and the stress–strain relationship when a material plastically deforms. Lastly, the fracture model is described, which gives the fracture strains and the damage accumulation in the stress state.

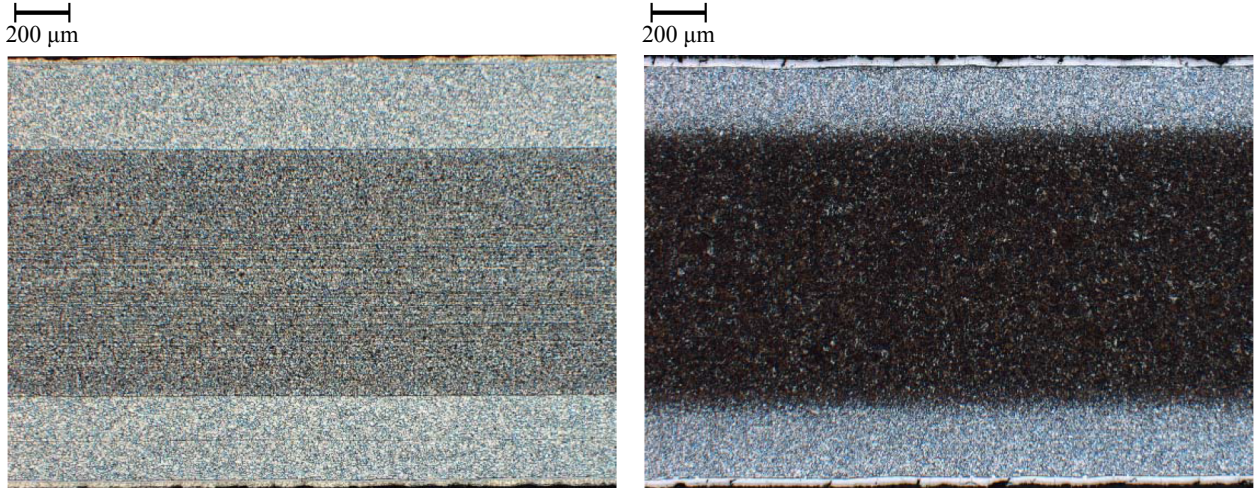


**Figure 2.3** *Micrographs of the etched surface of Tribond 1200 specimens before (a) and after hot forming (b). (Source: ThyssenKrupp [4])*

### 2.2.1 Yield criterion

The yield criterion specifies a convex surface in the 3D stress space, where the material behavior transitions from elastic to plastic. There are many different yield criteria to be found in the literature. For the hot formed steel 22MnB5, Mohr [26] uses a planar isotropic Hill [21] yield criterion, whereas Eller [13] uses an isotropic, modified version of the Yld2000-2d [8] yield criterion, with good results. Both studies first determine the amount of anisotropy in the material with the Lankford coefficients and conclude that a (planar) isotropic model suffices for crash simulation purposes.

For sheet metals, two well-known isotropic models are the Tresca and Von Mises yield criteria. In both of these yield criteria, the size of the yield surface is defined by a single variable: the yield stress  $\sigma_y$ . In principal stresses, the Tresca and Von Mises yield criteria are defined as:

$$\sigma_y = \max \{ |\sigma_1 - \sigma_2|, |\sigma_2 - \sigma_3|, |\sigma_3 - \sigma_1| \} \quad (2.1)$$

$$2\sigma_y^2 = (\sigma_1 - \sigma_2)^2 + (\sigma_2 - \sigma_3)^2 + (\sigma_3 - \sigma_1)^2. \quad (2.2)$$

The Tresca and Von Mises plane stress yield surfaces in the normalized principle stress space are shown in Figure 2.4a. The figure also shows different stress states, these are further detailed in Table 2.2. When the Tresca and Von Mises yield criteria are calculated with the same value of  $\sigma_y$ , they give dissimilar yield points for different stress states. This shows that characterizing a yield surface with the yield stress of the uni-axial tensile test does not conclusively specify which yield criterion to use when trying to model a materials plane strain tension or shear behavior. For this, the yield point in a notched tensile or shear test needs to be known as well.

For 22MnB5, Eller [13] found that the Von Mises yield criterion overestimates the yield stress in plain strain tension. An alternative isotropic yield surface is the Hershey [20] yield criterion. This criterion is more flexible than the Tresca or Von Mises criteria as it depends on two variables. The Hershey yield criterion is isotropic and lies somewhere in between the Tresca and Von Mises yield criteria, see Figure 2.4b. In principal stresses, the Hershey yield criterion is defined as:

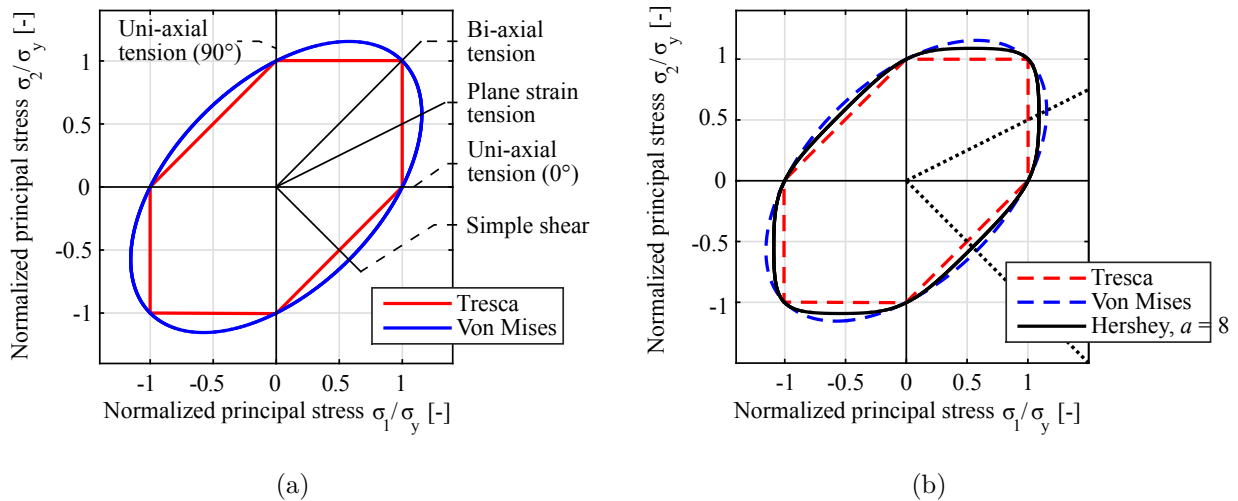
$$2\sigma_y^a = (\sigma_1 - \sigma_2)^a + (\sigma_2 - \sigma_3)^a + (\sigma_3 - \sigma_1)^a \quad (2.3)$$

in which exponent  $a$  must be an even number. For  $a = 2$  or as  $a$  goes to  $\infty$ , the Hershey yield criterion reduces to the Von Mises or the Tresca yield criteria, respectively. According to Hosford [23], a Hershey parameter of  $a = 6$  or  $a = 8$  is well suited for modeling the yield surface of BCC or FCC materials, respectively. When calibrating the Hershey yield criterion, the experimental results of uni-axial tension tests and plane strain tension or simple shear tests will be needed.

The Hershey yield criterion is an expansion on the Tresca and Von Mises yield criteria. These yield criteria are all isotropic, an example of an anisotropic yield criterion is the Yld2000-2d [8]. This yield criterion has eight variables and thus more flexibility to describe material anisotropy. In the isotropic case, the Yld2000-2d criterion simplifies to a 2D Hershey yield criterion.

**Table 2.2** Overview of the mechanical tests principal stresses and stress states for different in-plane loading cases.

Plane stress ( $\sigma_3 = 0$ )	Mechanical test	Principal stresses	Stress state
Uni-axial tension	Uni-axial tensile test	$\sigma_1 = \sigma; \sigma_2 = 0$	$\eta = \frac{1}{3}; \theta = 1$
Plane strain tension	Notched tensile test	$\sigma_1 = \sigma; \sigma_2 = \frac{1}{2}\sigma$	$\eta = \frac{1}{\sqrt{3}}; \theta = 0$
Bi-axial tension	Bulge test	$\sigma_1 = \sigma_2 = \sigma$	$\eta = \frac{2}{3}; \theta = -1$
Simple shear	Shear test	$\sigma_1 = \sigma; \sigma_2 = -\sigma$	$\eta = 0; \theta = 0$

**Figure 2.4** Plane stress representations of the Tresca and Von Mises yield criteria, with different in-plane loading cases marked (a) and with the Hershey yield criterion (b).

To quantify the amount of anisotropy in a metal, the Lankford coefficients are used. The calculation method is presented in Appendix A. In Section 3.2.1, the  $r$ -values are shown, calculated for the full-Tribond specimens extracted at  $0^\circ$ ,  $45^\circ$  and  $90^\circ$  angles to the sheet rolling direction. A sheet metals anisotropy is a consequence of the rolling process. The austenitizing and quenching in a hot forming process is expected to influence the anisotropy induced by the rolling process. The  $r$ -values in Eller [13] suggest that the hot forming process does indeed have a normalizing effect on the anisotropy of the sheet metal, with the relative differences in directional yield stresses decreasing by half after a hot forming treatment.

## 2.2.2 Hardening

Material hardening encompasses the yield criterion evolution and the stress–strain relationship due to plastic deformation. The yield criterion evolution is described by the hardening law. A material’s stress–strain relationship, for plastic strains, is calibrated in a hardening curve.

The hardening law describes the effect of plastic deformation on the yield surface. The yield surface evolution can be described by either kinematic or isotropic hardening, see Figure 2.5. In kinematic hardening, the yield surface translates. In isotropic hardening, the size of the yield surface increases equally in all directions. The main difference between both laws is their behavior in cyclic loading, in which the kinematic hardening law is able to represent the Bauschinger effect. The kinematic hardening law changes a yield criterion from isotropic to anisotropic after plastic deformation and is therefore less commonly used in simulations than the isotropic hardening law.

A hardening curve is generally based on a strain hardening law. There are many different strain hardening laws available in the literature. Well known laws are the Swift [30] and Voce [32] strain hardening laws. For calibrating 22MnB5, Eller [13] used a non-linear mix between the Swift and a modified Voce law. For calibrating Tribond’s hardening, a similar flexible approach will be used. The hardening parameters are given by the Swift power law:

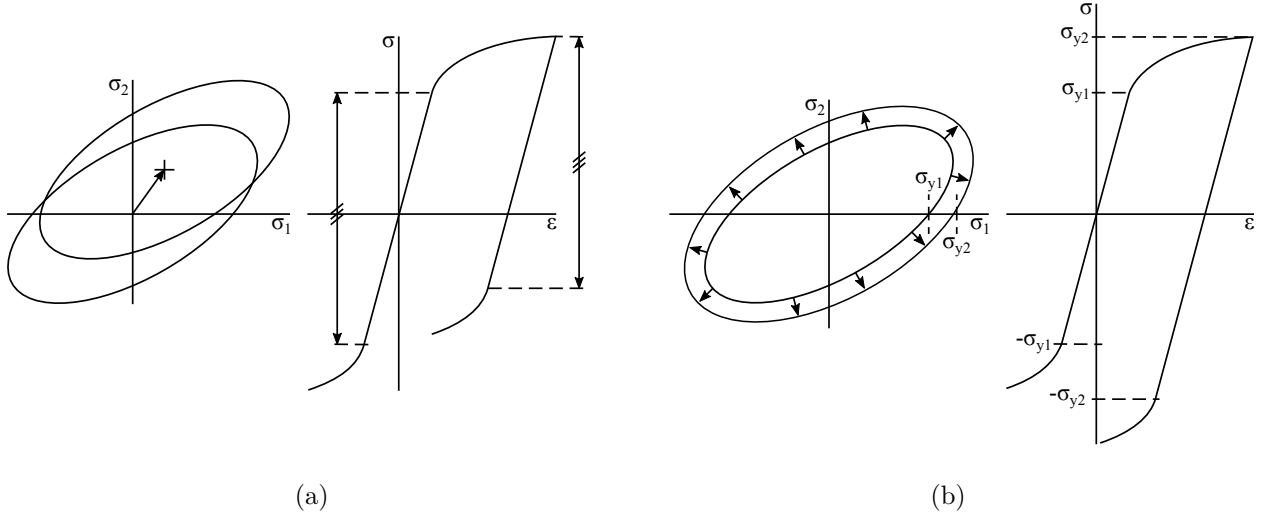


**Figure 2.5** Illustrations of the 1D and 2D yield surface evolution described by the kinematic (a) and isotropic hardening laws (b).

$$\sigma_S(\bar{\varepsilon}_p) = k_S(\bar{\varepsilon}_p + \varepsilon_{0,S})^{n_S}, \quad (2.4)$$

the classical Voce saturation law:

$$\sigma_V(\bar{\varepsilon}_p) = \varepsilon_{0,V} + k_V(1 - e^{-n_V \bar{\varepsilon}_p}) \quad (2.5)$$

and the mixing rule:

$$\sigma = \lambda_V \cdot \sigma_V + (1 - \lambda_V) \cdot \sigma_S \quad (2.6)$$

in which the mixing parameter  $\lambda_V$  is defined as:

$$\lambda_V = \lambda_{\text{final}} + (\lambda_{\text{initial}} - \lambda_{\text{final}}) \cdot e^{-\alpha_{\text{shape}} \bar{\varepsilon}_p}. \quad (2.7)$$

The hardening parameters are  $k_S$ ,  $\varepsilon_{0,S}$ ,  $n_S$ ,  $\varepsilon_{0,V}$ ,  $k_V$ ,  $n_V$ ,  $\lambda_{\text{final}}$ ,  $\lambda_{\text{initial}}$  and  $\alpha_{\text{shape}}$ .

At the Volkswagen Group Research, a standardized process is used for calibrating the hardening parameters of a material. The hardening parameters define a true stress–true equivalent plastic strain  $\sigma(\bar{\varepsilon}_p)$  curve, Figure 2.6 shows an example of such a hardening curve. The initial section of the stress–strain  $\sigma_{\text{initial}}(\bar{\varepsilon}_p)$  curve is calculated from the measured force–displacement curves up to force maximum of the uni-axial tensile test results. The method for calculating the true stress and true equivalent plastic strain is shown in Appendix B. After force maximum, this calculation method is no longer valid and the stress–strain relationship needs to be approximated for higher  $\bar{\varepsilon}_p$ . Therefore, the complete hardening curve is a combination of the experimental results and the mixed Swift and Voce law extrapolations. The Swift and Voce law extrapolation are determined by fitting these laws to the last section of the  $\sigma_{\text{initial}}(\bar{\varepsilon}_p)$  curve. This is done, to ensure a smooth transition between the experimental results and the Swift and Voce law extrapolations. The mixing rule parameters are determined in an inverse FEM optimization. By definition, the results from the optimization will lie somewhere between the Swift and Voce law extrapolations. During the optimization, the objective function calculates the difference between simulation and experimental results. It compares the force–displacement curves of both tensile tests after force maximum and similar to Haddadi [17] it also compares two strain fields of the notched tensile test at two different strains. The strain fields are compared at force maximum and after initiation of localized necking. The result of the optimization is the optimized mixing rule parameter  $\lambda_V$ , which defines the hardening curve after  $\sigma_{\text{initial}}(\bar{\varepsilon}_p)$ . Figure 2.7 shows this standardized process in a flow diagram.

With the elasto–plastic behavior calibrated, the next step is to characterize the fracture behavior of the material.

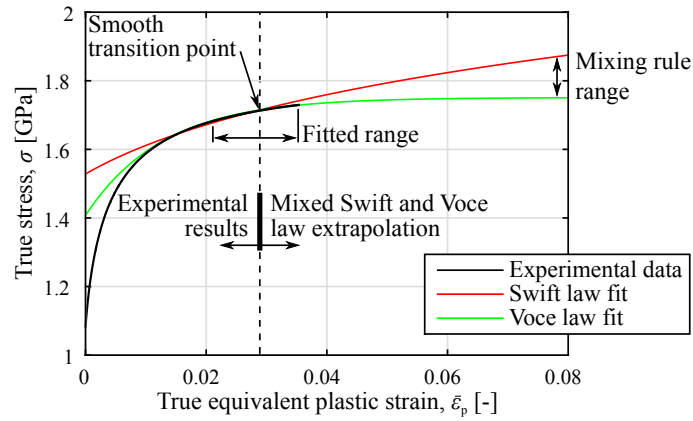


**Figure 2.6** Illustrative experimental true stress–true equivalent plastic strain curve and fitted Swift and Voce laws.

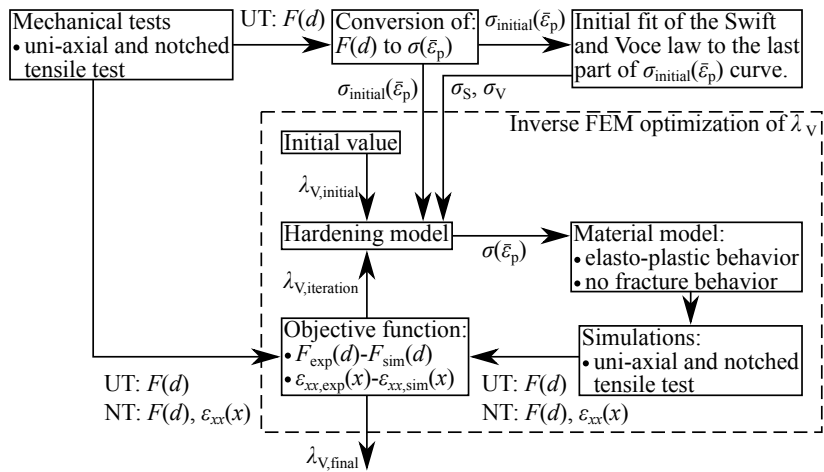


**Figure 2.7** Flow diagram of the standard inverse FEM optimization to determine the unknowns of the non-linear mixing rule for a material hardening curve.

### 2.2.3 Fracture model

For application in crash simulations, the material model needs to accurately describe fracture behavior. The modified Mohr–Coulomb (mMC) fracture model developed by Bai [5] is used. This model describes ductile fracture in materials. The mMC fracture model defines the equivalent fracture strain  $\bar{\epsilon}_f$  as a function of the stress triaxiality  $\eta$  and the normalized Lode angle parameter  $\bar{\theta}$ . When an element plastically deforms, it will accumulate damage until fracture according to the damage evolution rule.

#### 2.2.3.1 Stress triaxiality and Lode angle parameter

Material ductility is shown to depend on both the stress triaxiality  $\eta$  and the normalized Lode angle parameter  $\bar{\theta}$  [5]. The stress triaxiality  $\eta$  is defined by:

$$\eta = \frac{\sigma_m}{\bar{\sigma}} \quad (2.8)$$

where  $\sigma_m$  is the hydrostatic pressure which is positive in compression and  $\bar{\sigma}$  is the equivalent Von Mises stress. The Lode angle  $\theta$  is calculated from:

$$\cos(\theta) = \frac{27(\sigma_1 - \sigma_m)(\sigma_2 - \sigma_m)(\sigma_3 - \sigma_m)}{2\bar{\sigma}^3} \quad (2.9)$$

in which  $\sigma_1$ ,  $\sigma_2$  and  $\sigma_3$  are the principal stresses, with  $\sigma_1 \geq \sigma_2 \geq \sigma_3$ . The range of the Lode angle is  $0 \leq \theta \leq \pi/3$ . This is normalized to give:

$$\bar{\theta} = 1 - \frac{6\theta}{\pi}. \quad (2.10)$$

The range of the normalized Lode angle becomes  $-1 \leq \bar{\theta} \leq 1$ .

#### 2.2.3.2 mMC Fracture surface

The fracture criterion used in this work is a modified version of the Mohr–Coulomb criterion. Bai [5] rewrote the stress-based form of the criterion to a strain-based form. The equivalent fracture strain is defined as:

$$\bar{\epsilon}_f(\eta, \bar{\theta}) = \left\{ \frac{k_S}{c_2} \left[ c_3 + (c_\theta - c_3) \frac{\sqrt{3}}{2 - \sqrt{3}} \left( \sec\left(\frac{\pi}{6}\bar{\theta}\right) - 1 \right) \right] \left[ \sqrt{\frac{1 + c_1^2}{3}} \cos\left(\frac{\pi}{6}\bar{\theta}\right) + c_1 \left( \eta + \frac{1}{3} \sin\left(\frac{\pi}{6}\bar{\theta}\right) \right) \right] \right\}^{\frac{-1}{n_S}} \quad (2.11)$$

in which:

$$c_\theta = \begin{cases} 1 & \text{for } \bar{\theta} \geq 0 \\ c_4 & \text{for } \bar{\theta} < 0 \end{cases}.$$

The parameters  $k_S$  and  $n_S$  are the factor and exponent of the Swift hardening law. They are determined by fitting the Swift law to the hardening curve. The parameters  $c_{1-4}$  are calibrated from experimental results. This is done using data from four different tests, which are listed in Table 2.2. An example of a fitted fracture surface and the loci of the four different tests are shown in Figure 2.8a. The figure also shows the plane stress fracture curve, which is of importance in sheet metal failure. According to Bai [5], for the plane stress condition  $\eta$  and  $\bar{\theta}$  are related through:

$$\cos\left[\frac{\pi}{2}(1 - \bar{\theta})\right] = -\frac{27}{2}\eta\left(\eta^2 - \frac{1}{3}\right). \quad (2.12)$$

In the four different experiments, fracture will occur in different places in the stress state. As the shape of the mMC fracture surface suggests, some stress states allow for higher amounts of plastic strain before fracture than others (Figure 2.8b).

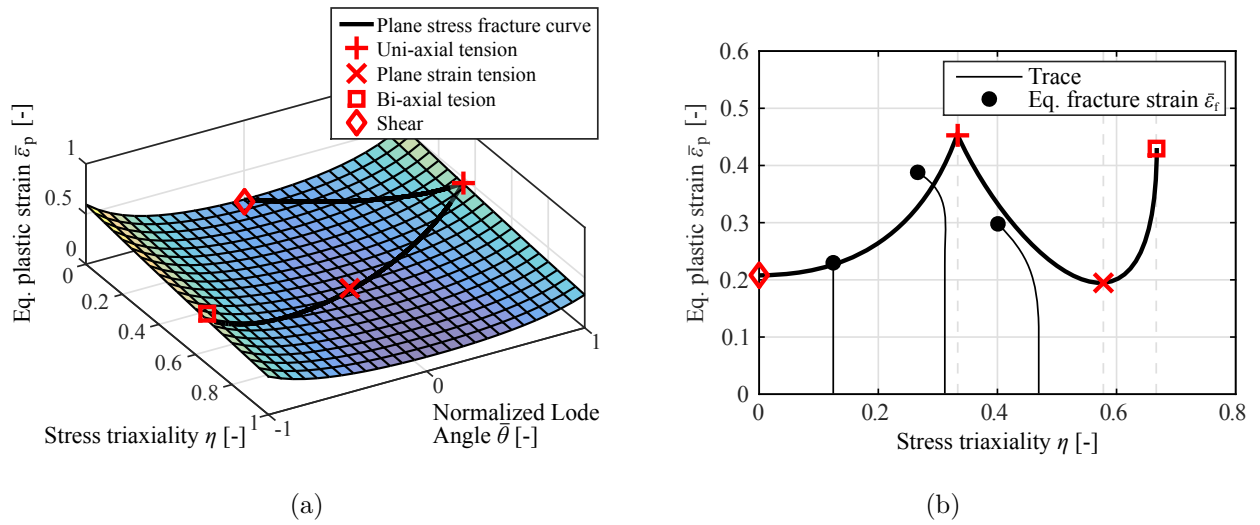


**Figure 2.8** Example mMC fracture surface (a) and the plane stress fracture curve (b) with different stress states marked. Fracture surface adapted from Bai [7]. ( $k = 740 \text{ MPa}$ ,  $n = 0.15$ ,  $c_1 = 0.0345$ ,  $c_2 = 338.6 \text{ MPa}$ ,  $c_3 = c_4 = 1.0$ )

### 2.2.3.3 Damage evolution rule

The point of fracture due to plastic deformation is specified by the damage evolution rule. The damage the material accumulates due to plastic deformation is described by the damage indicator  $D$ , where  $0 \leq D < 1$ . Damage in a stress state trace is calculated with the integral:

$$D(\bar{\epsilon}_p) = \int_0^{\bar{\epsilon}_p} \frac{1}{\bar{\epsilon}_f(\eta, \bar{\theta})} d\bar{\epsilon}_p \quad (2.13)$$

in which the stress space parameters  $\eta$  and  $\bar{\theta}$  are functions of the equivalent plastic strain  $\bar{\epsilon}_p$ . An element in an FE model will eliminate when the damage indicator of its stress state trace reaches the critical value of  $D = 1$ . This represents fracture in a simulation.

The damage evolution rule can be interpreted as follows. When plastic deformation initiates at a specific stress state  $\eta$  and  $\bar{\theta}$ , the equivalent fracture strain  $\bar{\epsilon}_f$  is known from Equation 2.11. In the case of proportional loading (a constant stress state), the damage will accumulate along a vertical trace, which reaches its critical value exactly on the mMC fracture surface, see Figure 2.8b. In the case of non-proportional loading (a non-constant stress state), the damage indicator can reach a critical damage value below or above the mMC fracture surface. An example of this is also given in Figure 2.8b.

CONFIDENTIAL

# Chapter 3

## Experimental work

In this chapter, experiments that have been used to investigate the mechanical behavior of Tribond are presented. The initial results of a through thickness study are also described for use in the hardness-driven material model. The main focus are the mechanical tests used to study the bulk material behavior, with hardness measurements and micrography to study abnormal behavior.

### 3.1 Initial Metallographic analysis and hardness measurements

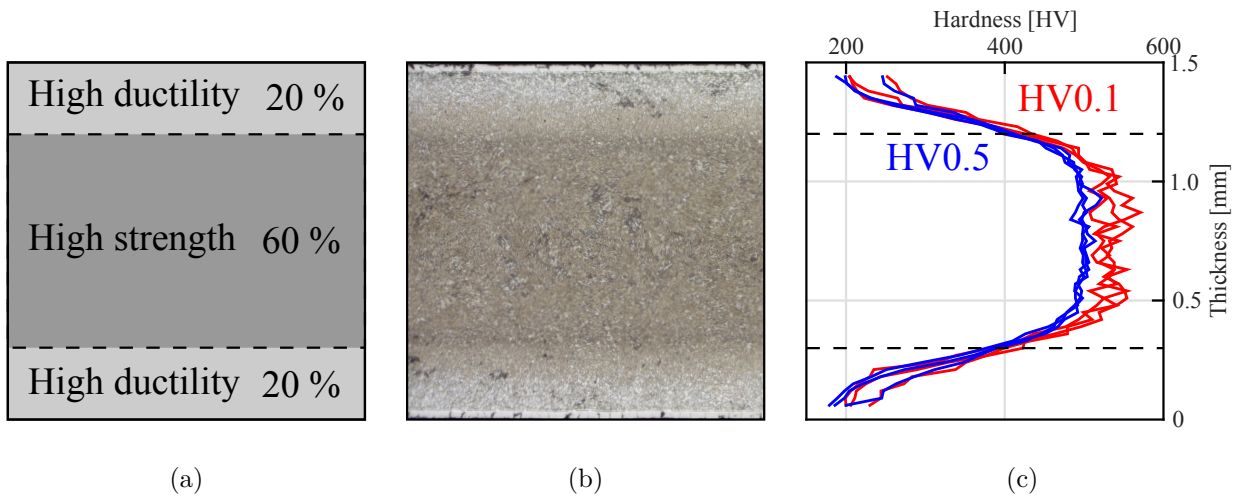
The Tribond material model will be hardness driven. Which means that the material properties through the thickness of the specimen will depend on hardness values. With a Vickers hardness test, hardness measurements are made along a specimen's thickness,  $HV(y)$ , where  $y$  is the position coordinate in thickness direction. The measurements are made after hot forming with two different indentation loads of 0.1 kgf and 0.5 kgf. The lower indentation load was used to obtain more data points along the specimen's thickness. In order to avoid the inaccuracy caused by the small indentation size, another set of hardness measurements with the higher indentation load was carried out. These data points were used for the hardness-driven model. Figure 3.1 shows Tribond 1200's composition, a micrograph of an etched specimen and the hardness properties through the thickness after hot forming. The hardness measurements show the transition between core and surface layer as a gradual increase in hardness. Furthermore, it shows a wide transition zone, larger than the 60  $\mu\text{m}$  given by ThyssenKrupp [9]. The results show that only 30% of the total thickness (50% of the core layer) reaches the expected core layer hardness. Which means, with a hardness-driven material model only this part will have purely core layer properties.

Figure 3.2 compares the results of the hardness measurements with different indentation loads. The two indentation loads show different core layer hardness values. The HV0.1 results show more scatter which is mainly due to the small indentation size. To fit enough data points for an accurate plot, the measurements were spread along the length of the specimen. To avoid hardness measurements being influenced by a previous indentation's cold work, the distance between two indentations was specified by the ISO 6507 standard. An important condition for spreading measurements over the length of the specimen is that the material properties are uniform along the length. As the spacing was kept small, local uniformity in the results of Figure 3.1c is assumed.

### 3.2 Mechanical tests

A set of mechanical tests is used to calibrate core and surface layer material models of Tribond 1200. Experiments with different load cases were performed to accurately determine the material's mechanical behavior under complex loading during a crash. The results of these tests will be used to calibrate plastic and fracture behavior in both core and surface layer material models.

The mechanical tests were performed with a Zwick/Roell Z250 universal material testing machine. Most tests also used GOM Aramis 5M with adjustable base and Digital Image Correlation (DIC) for strain field measurements. The DIC system uses up to two cameras to capture images during testing. The testing machine and Aramis are linked such that each image has corresponding force and displacement data. If a surface has enough contrast, Aramis can calculate the strains on the surface. Contrast is created by a speckle pattern, see Figure 3.7b.



**Figure 3.1** Side-by-side view of thickness properties of Tribond 1200, showing the composition (a), an etched specimen (b) and the hardness measurements (c) both after hot forming.

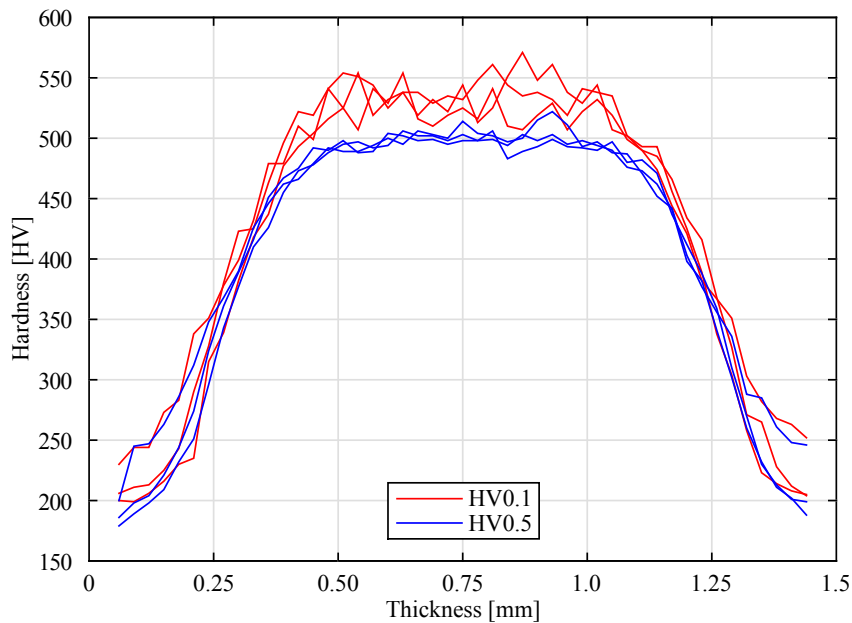


**Figure 3.2** Tribond 1200 through thickness hardness measurements, obtained using 0.1 kgf and 0.5 kgf indentation loads.

**Table 3.1** Overview of the mechanical tests used for calibration of the plastic and fracture behavior. The fracture strains are given for specific stress states  $\varepsilon_f(\eta, \theta)$ .

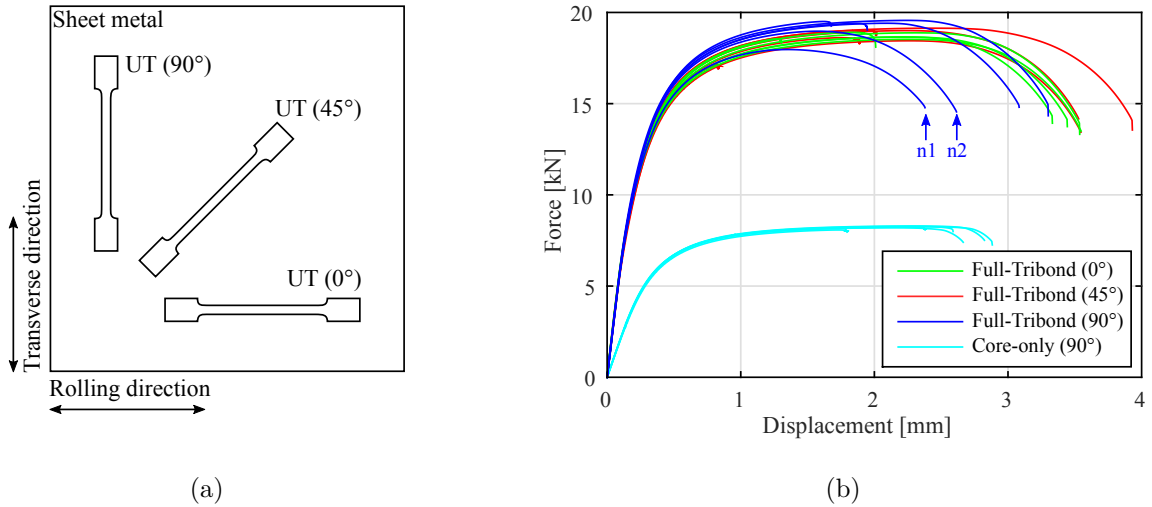
Mechanical test (abbr.)	Purpose	
	Core-only	Full-Tribond
Uni-axial tensile (UT)	$\sigma_{y,\text{core}}, E, \bar{\varepsilon}_{\text{core}}(\bar{\varepsilon}_{p,\text{init}})$	$r$ -values, $E, \bar{\sigma}_{\text{surf}}(\bar{\varepsilon})$
Notched tensile (NT)	$\bar{\sigma}_{\text{core}}(\bar{\varepsilon}_{p,\text{extrapol}})$	$E, \bar{\sigma}_{\text{surf}}(\bar{\varepsilon}), \varepsilon_{f,\text{core}}\left(\frac{1}{\sqrt{3}}, 0\right)$
Central hole tensile (CH)	<b>x</b>	$\varepsilon_{f,\text{core}}\left(\frac{1}{3}, 1\right)$ , investigation
Bulge test (BT)	<b>x</b>	$\varepsilon_{f,\text{core}}\left(\frac{2}{3}, -1\right)$
Shear (SH)	<b>x</b>	$\varepsilon_{f,\text{core}}(0, 0)$
3-Point bending, narrow specimen (BE1.5)	<b>x</b>	validation, investigation
3-Point bending, wide specimen (BE20)	<b>x</b>	$\varepsilon_{f,\text{core,min}}\left(\frac{1}{\sqrt{3}}, 0\right), \varepsilon_{f,\text{surface}}\left(\frac{1}{\sqrt{3}}, 0\right)$
Buckling bending, narrow specimen (BB1.5)	<b>x</b>	validation, investigation
Buckling bending, wide specimen (BB20)	<b>x</b>	validation

Table 3.1 gives an overview of the mechanical tests. For each different test type six specimens were tested, unless stated otherwise. The uni-axial tensile test specimens were extracted at  $0^\circ$ ,  $45^\circ$  and  $90^\circ$  angles relative to the sheet rolling direction, see Figure 3.3a. The results were used to investigate Tribond's anisotropy by calculating the Lankford coefficients or  $r$ -values. Specimens for all other mechanical tests were extracted in transverse direction of the sheet, which is the weakest direction in the sheet. In addition to the tests with the full-Tribond material, uni-axial and notched tensile tests with core material were performed. The core-only specimens were ground from full-Tribond specimens, by removing 0.5 mm transition zone from the top and bottom surface. This left a 0.5 mm thick specimen with only core material. This corresponds to the section identified as having core layer hardness, see Figure 3.2. The core-only specimens will be used for calibrating the core layer strain hardening. The uni-axial tensile core-only test results directly define the yield stress, Young's modulus and initial strain hardening. Together with the notched tensile core-only test results, they will be used in an inverse FEM optimization to indirectly fit the extrapolated strain hardening curve. The surface layer strain hardening will be indirectly determined in an inverse FEM optimization from uni-axial and notched tensile full-Tribond test results. To calibrate the fracture behavior of the material four additional tests were performed. Together with the notched tensile tests these specify fracture strains  $\varepsilon_f$  at different, well-defined stress states. The mechanical tests used to calibrate fracture are the notched tensile, central hole tensile, bulge, shear and 3-point bending tests. To further investigate and validate the final material model buckling bending tests were also performed. For both bending tests, narrow and wide Tribond specimens of respectively 1.5 mm and 20 mm width were used. An overview of the tests is presented in Table 3.1.

### 3.2.1 Uni-axial tensile test

Uni-axial tensile tests have been performed for full-Tribond and core-only specimens. The full-Tribond specimens were extracted at  $0^\circ$ ,  $45^\circ$  and  $90^\circ$  angles relative to the sheet rolling direction, see Figure 3.3a. The specimen geometry is shown in Figure C.1. The specimen thickness values were  $t = 1.5$  mm for the full-Tribond specimens and  $t = 0.5$  mm for the core-only specimens.

For testing, a gauge length of  $l_0 = 50$  mm and a quasi-static cross-head speed of  $0.1 \text{ mm s}^{-1}$  were used. To measure the force, a standard load cell was used, with a nominal capacity of 250 kN and an accuracy of 10 N. The displacement was measured with a Makro Xtens extensometer. This extensometer clamps the specimen and has a high accuracy of  $\pm 1 \mu\text{m}$ . The measured force-displacement curves are shown in Figure 3.3b. The yield stress values were calculated from the force-displacement curves using a Young's



**Figure 3.3** Sheet metal with uni-axial tensile test cutouts at  $0^\circ$ ,  $45^\circ$  and  $90^\circ$  angles to the rolling direction (a). Measured force–displacement curves of four different uni-axial tensile tests (b).

modulus of 190 GPa and an offset of 0.2%. Strain fields were measured with a DIC system. A 2D camera setup was used to track a speckle pattern on the specimen’s front during testing. To calculate  $r$ -values of three different sets of full-Tribond specimens, the true total strains in axial and width directions were obtained from the DIC, see Appendix A. The mean values and standard deviations of the yield stresses and  $r$ -values are shown in Table 3.2. The full-Tribond yield stresses in rolling direction show the least variation. The other yield stresses have higher variations. The full-Tribond  $r$ -values are slightly less than one and are relatively similar. No  $r$ -values were calculated for the core-only specimens. In Figure 3.3b, two outliers of the transverse direction full-Tribond test results are highlighted. The lower strength and ductility of outlier n1 were further investigated with the use of the strain field measurements, see Figure 3.4. It can be seen that strain localization occurs at a very early stage of the experiment, at a displacement of  $d = 0.30$  mm. This is clearly before force maximum at  $d = 1.40$  mm. It seems the lower strength and ductility of this specimen are the result of a local weak spot in the material. The other marked outlier n2 showed similar results. The weak spots in these specimens could be caused by the rolling process or press hardening. The rolling process might allow inclusions in the weld between the base steels or the uneven distribution through the thickness of the base steels during rolling. Whereas not properly quenching or heating of the sheets might have influenced the martensitic microstructure. To check the full-Tribond sheets, the global uniformity of the hardness values along a length of 70 mm were investigated. The hardness values were measured with a 0.1 kgf indentation load, as this allowed for a closer spacing of the measurement points. Using the ISO 6507 standard, the amount of measurement points on the side of a specimen was limited. The results are shown in Figure 3.5. Between a length of 10 mm – 40 mm, the material shows a lower core layer hardness fraction. Whether this is caused by the rolling process or press hardening of the Tribond sheets is unknown.

The uni-axial tensile core-only test results not influenced by weak spots will be used to directly specify the yield stress, Young’s modulus and initial stress–strain relationship in the core layer plasticity model. Furthermore, both the core-only and full-Tribond specimen results will be used in the core and surface layer plasticity optimizations, respectively. The plasticity optimization is described in Chapter 4.

### 3.2.2 Notched tensile test

Notched tensile tests have been performed for full-Tribond and core-only specimens. The specimen geometry is shown in Figure C.2. The specimen thickness values were  $t = 1.5$  mm for the full-Tribond specimens and  $t = 0.5$  mm for the core-only specimens.

The test were performed with a quasi-static cross-head speed of  $0.1 \text{ mm s}^{-1}$ . The force–displacement curves were measured with the same load cell and extensometer as the uni-axial tensile tests. The strain fields were measured with a 3D DIC camera setup. This setup can also accurately correlate the strains on the surface of the specimen when the measured surface moves out-of-plane during necking. This is necessary, because the strain hardening optimizations require accurate strain fields at high strains. The measured force–displacement curves are shown in Figure 3.6a. The curves show very little scatter with no outliers.

**Table 3.2** Mean values and standard deviations (SD) of the yield stresses and r-values for all uni-axial tensile tests.

Specimen		$\sigma_{\text{yield,Rp0.2}}$ [MPa]	$r$ [-]
Full-Tribond (0°)	Mean	881	0.812
	SD	9.5	0.073
Full-Tribond (45°)	Mean	887	0.903
	SD	19.9	0.081
Full-Tribond (90°)	Mean	932	0.746
	SD	20.9	0.009
Core-only (90°)	Mean	1265	–
	SD	13.9	–

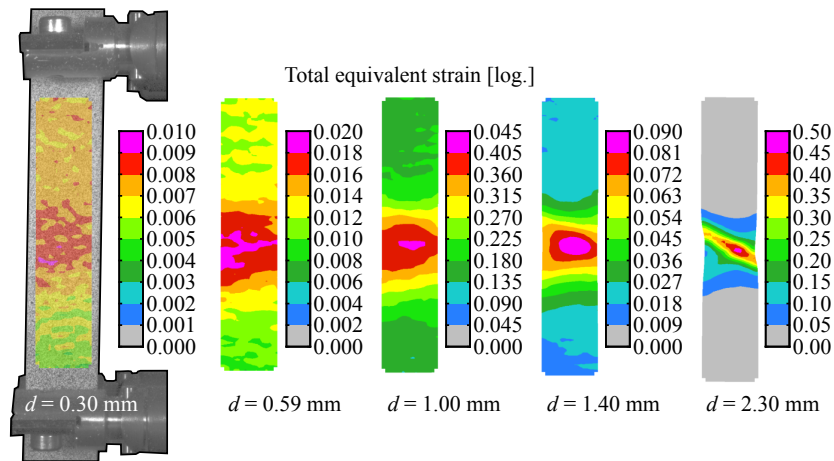


**Figure 3.4** Clamped specimen with strain field overlay and the measured strain fields at different displacements during testing of uni-axial tensile test outlier.

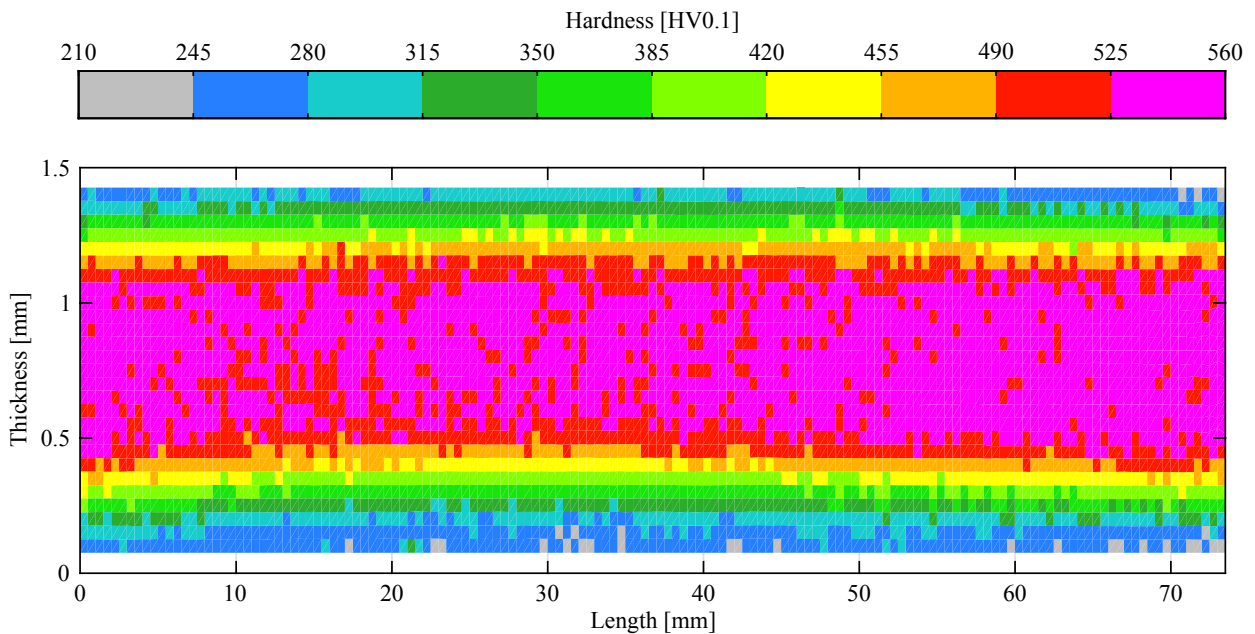


**Figure 3.5** Tribond 1200 steel sheet edge hardness measurement, obtained using 0.1 kgf indentation load.

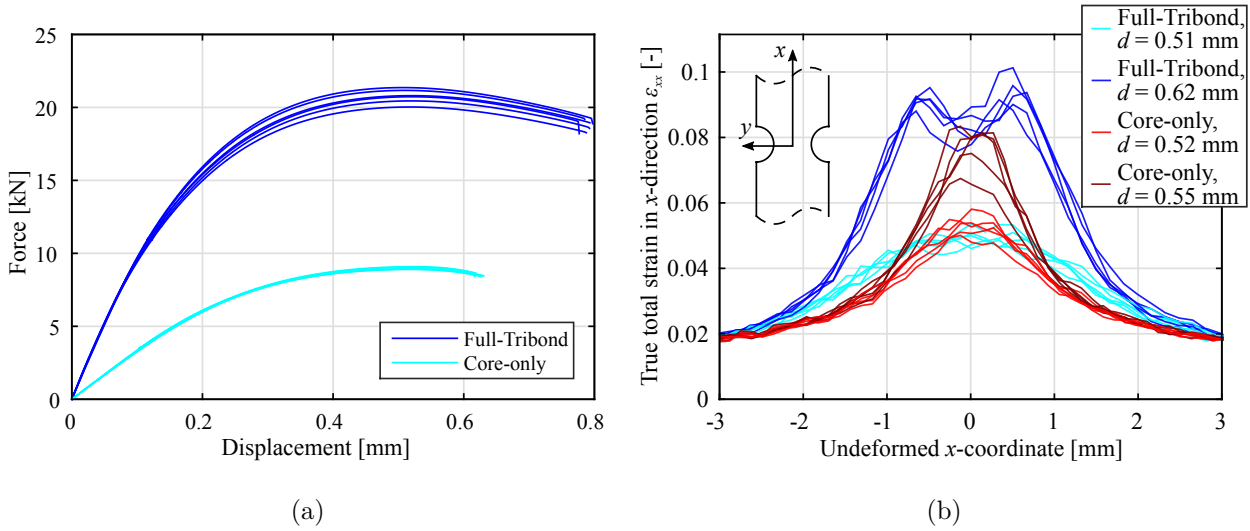


**Figure 3.6** Measured force–displacement curves (a) and total strain curves at force maximum and after initiation of localized necking (b) for two different notched tensile tests.

Figure 3.6b shows the strain fields at force maximum and after initiation of localized necking for both notched tensile tests. The true total strain curves are plotted along the  $x$ -coordinate shown in the inset. The two strain peaks observed at  $d = 0.62$  mm on the surface of the full-Tribond specimens are due to necking through the thickness. The strain fields are shown in a side-by-side comparison in Chapter 4.

The notched tensile core-only and full-Tribond test results will be used in the core and surface layer plasticity optimizations, respectively. The full-Tribond results will also be used to calibrate the core layer and validate the surface layer fracture models for the plane strain tension stress state.

### 3.2.3 Central hole tensile test

Central hole tests have been performed for full-Tribond specimens only. The specimen geometry is shown in Figure C.3.

The force–displacement curves were measured with the same load cell and extensometer as the uni-axial tensile tests. The strain fields were measured with a 2D DIC camera setup. To get better insight in the fracture behavior of the surface and core material, the inside of the hole was filmed with a Canon EOS 700D. The hole’s lateral edge in an upright specimen fails first under a well-defined uni-axial tension stress state. The Canon camera was used to capture this fracture initiation on the hole’s inner surface. The video properties were switched between high resolution images at low frame rate and lower resolution images at higher frame rate. The highest frame rate at maximum resolution was 24 fps, so to facilitate capturing as much video data as possible, the tensile tests were performed at a low cross-head speed of  $0.005 \text{ mm s}^{-1}$ . As the default testing speed of  $0.1 \text{ mm s}^{-1}$  may be considered quasi-static, no influence on the force–displacement curves is expected when using a lower speed. The measured force–displacement curves are shown in Figure 3.7a. Figure 3.7b shows an image captured by the Canon camera of the inner surface of a strained central hole specimen. This image was captured just before fracture, it shows necking at the lateral edge of the hole. No abnormal behavior was observed in the Canon video data, the material appeared to fail instantly. A higher frame rate might reveal complete core layer failure before the surface layer fractures. However, with the current results, the Tribond is assumed to have the same macro level behavior as any other non-composite steel.

The central hole tensile test results will be used to calibrate the core layer fracture model for the uni-axial tension stress state. They will also be used to validate Tribond’s surface layer fracture model.

### 3.2.4 Bulge test

Bulge tests have been performed for full-Tribond specimens only. The specimen geometry was a square sheet of 127 mm by 127 mm.

A schematic overview of the test setup is shown in Figure 3.8b. A specimen was mounted in the clamp which was secured with eight bolts, each bolt was tightened with a torque of 70 Nm. The clamp and

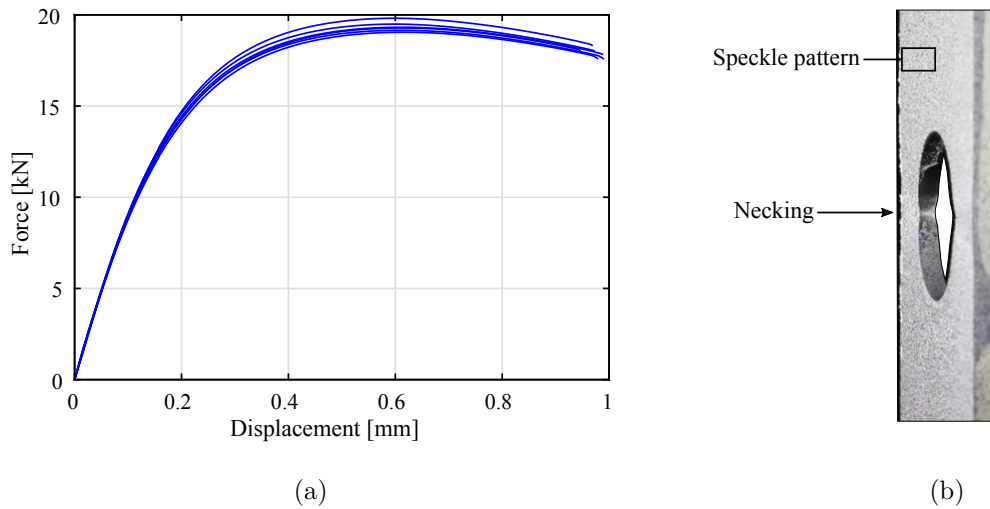


**Figure 3.7** Measured force–displacement curves of the central hole tensile tests (a). Image of the hole’s inner surface of a strained upright central hole specimen (b).

punch were mounted on the universal testing machine. The clamp, punch and the specimen were mounted concentrically. The specimens were covered with a double layer of 0.17 mm thick PTFE film and a lubricant to decrease friction forces between the punch and the specimen. During the test the punch moved upwards. The tests were performed with a quasi-static cross-head speed of  $20 \text{ mm min}^{-1}$ . The forces of the force–displacement curves were measured with the standard load cell. For the displacement measurement a 2D DIC camera setup was used. By tracking the relative displacements between two contrast dots on the clamp and punch the displacement was accurately measured. The local displacement measurement was required, in order to avoid elastic influences from the clamp and punch mounts when measuring the displacement with the built-in cross-head travel monitor. The strain fields were measured with a 3D DIC camera setup. The DIC used a mirror setup to capture the strain fields on the top of the specimens. For an image of the setup see Figure D.1. The measured force–displacement curves are shown in Figure 3.8a. The curves with the highest and lowest fracture displacements are highlighted. Figure 3.9 shows the strain fields of the highlighted specimens at a displacement of  $d = 18 \text{ mm}$  and post-fracture. Specimen n4 is found to have a deviating strain field with non-circular strain localization and a differing fracture direction. This is caused by a weak spot in the material near the tip of the punch. This would also explain the relatively low fracture displacement.

The bulge test results will be used to calibrate the core layer fracture model for the bi-axial tension stress state. They will also be used to validate the surface layer fracture model.

### 3.2.5 Shear test

Shear tests have been performed for full-Tribond specimens only. The specimen geometry is shown in Figure C.4. The specimen geometry was developed by Greve [16] to determine the fracture strain for the simple shear stress state.

A schematic overview of the test setup is shown in Figure 3.10b. A specimen was mounted in a two piece clamp, one piece fastens the outer parts and one piece the main part of the specimen. Each part was fastened with a bolt, the bolts clamping the outer parts were tightened with a torque of 70 Nm, the main part fastening bolt was hand tightened. The bolts effectively fasten the specimen in the shape lock. During testing the main part moved down. The tests were performed with a quasi-static cross-head speed of  $0.1 \text{ mm s}^{-1}$ . A standard load cell was used to measure the force required to move the main body down. The displacement was measured locally on the specimen to avoid measuring the influence of elastic deformations in the test setup. For the local displacement measurement, two contrast points in the strain field were used. The strain fields were measured with a 2D DIC camera setup. The measured force–displacement curves are shown in Figure 3.10a.

The shear test results will be used to calibrate the core layer fracture model for a simple shear stress state.

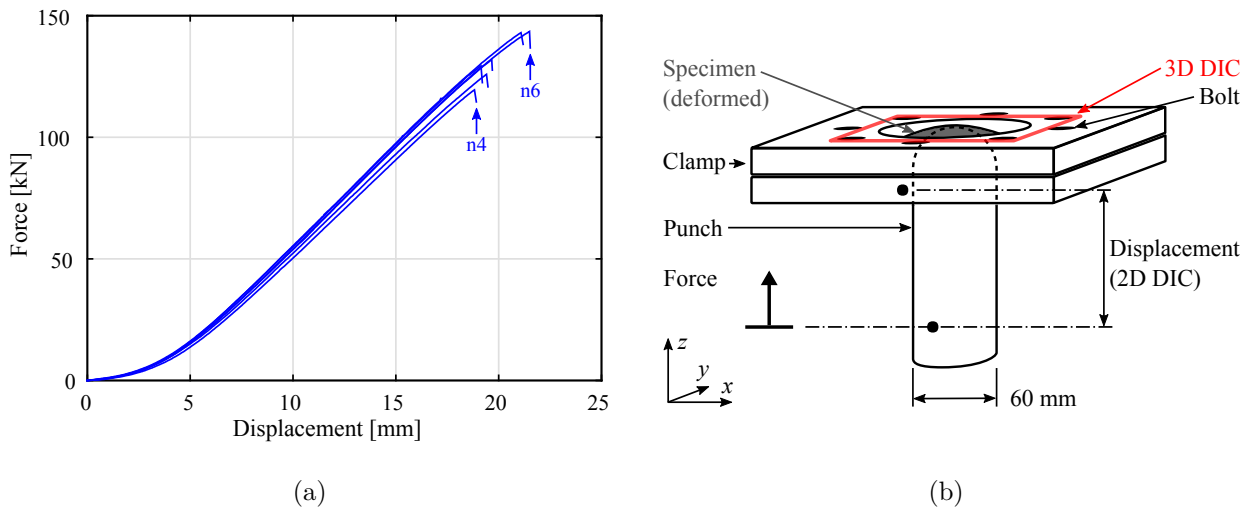


**Figure 3.8** Measured force–displacement curves (a) and a schematic overview of the test setup (b) of the bulge test.

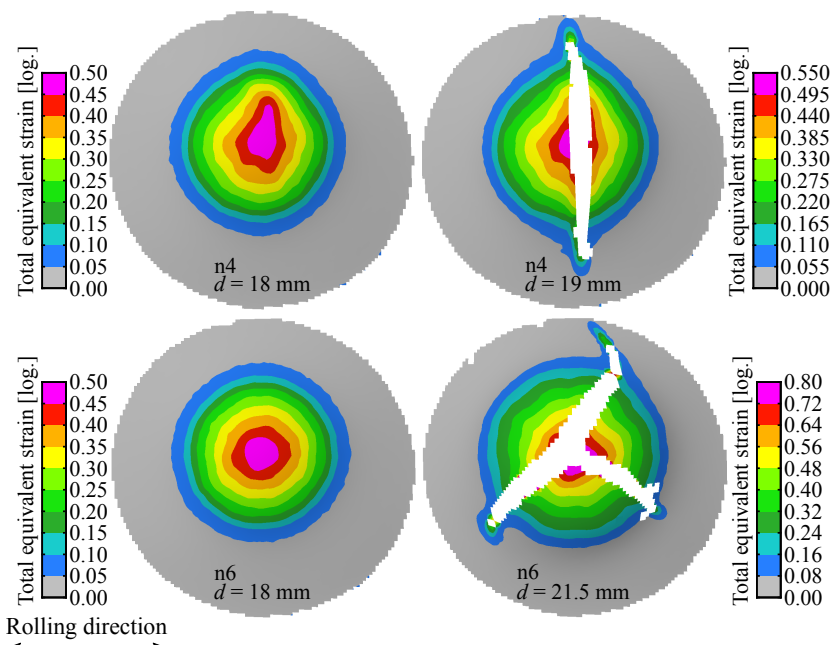


**Figure 3.9** Measured strain fields for bulge test specimens *n4* and *n6* at a displacement of  $d=18$  mm and post-fracture.

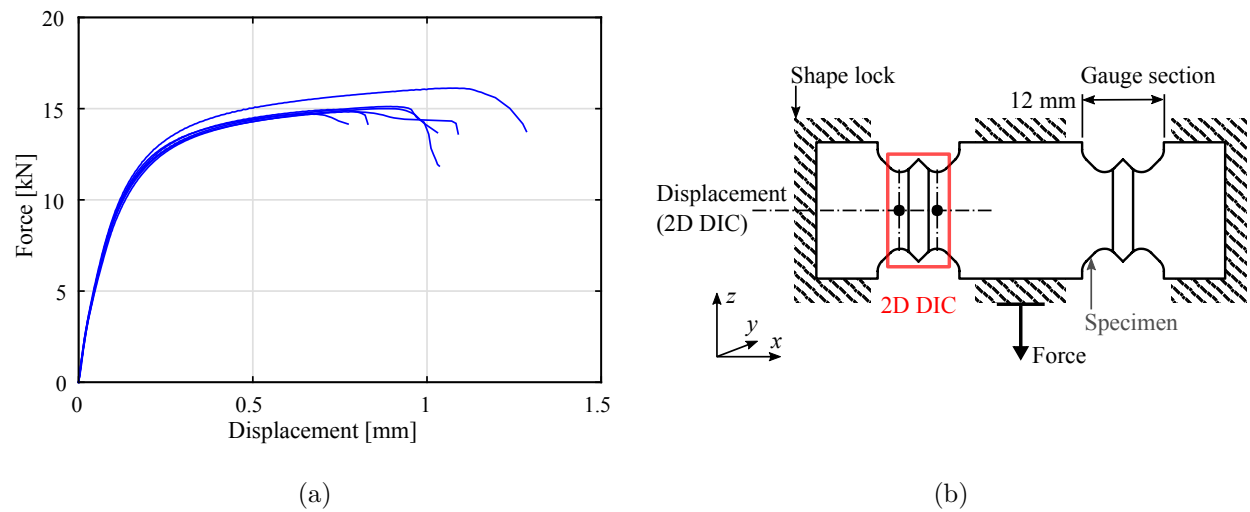


**Figure 3.10** Measured force–displacement curves (a) and a schematic overview of the test setup (b) of the shear test.

### 3.2.6 3-Point bending test

3-Point bending tests have been performed for full-Tribond specimens only. The tests were performed according to the VDA 238-100 standard [31]. However, instead of a 60 mm wide specimen, two different geometries were tested, a narrow (1.5 mm) and wide (20 mm) specimen. The narrow specimen geometry is shown in Figure C.5. The wide specimen geometry was a rectangular sheet of 20 mm by 60 mm. These different geometries produce different stress states in the specimens during testing: a uni-axial tension and plane strain tension stress states in the narrow and wide specimens, respectively. The shut-off criterion was also changed from a 30 N force drop to a 80 % force drop or until unimpaired bending was no longer assured after a displacement of  $d = 15$  mm.

The test setup is shown in Figure 3.12a. In this test a specimen was supported on two rollers, the rollers then move upwards to bend the specimen. The inner bending radius matches the radius of the knife. The test was performed with a quasi-static testing speed of  $0.1 \text{ mm s}^{-1}$ . The force–displacement curves for the narrow specimen were measured with a low force load cell, with a nominal capacity of 10 kN and an accuracy of 3 N. The wide specimen forces were measured with the standard load cell. The displacements for both geometries were measured with the built-in cross-head travel monitor. No strain fields were measured. The measured force–displacement curves of the narrow and wide specimen geometries are shown in Figure 3.11. The force–displacement curves of the narrow specimens show the material does not fail before test end at  $d = 15$  mm. The wide specimens do show failure. The six wide specimens were bend beyond the point of fracture initiation of this out-of-plane loading test has to be known. To get specimens which only showed fracture initiation, new tests had to be performed. These tests were interrupted based on the amount of force drop after force maximum. The force–displacement curves were not added to Figure 3.11b. These interrupted bending test specimens showed very little external signs of cracking so they were cut to investigate if the material had failed internally. A specimen’s crack investigation micrographs are shown in Figures 3.12b and 3.13. The etched specimen micrograph shows the movement of the core layer during bending and a crack in the outer fiber of the material (Figure 3.12b). The unetched image shows that the crack initiated internally, the intact outer surface was however removed by the polishing required to etch the specimen (Figure 3.13).

The 3-point bending narrow test results will be used to validate the material models plasticity, it will also be used as a lower bound for the fracture validation as no fracture occurs in this specimen. The wide specimen results will be used in the calibration of the fracture model as fracture does occur in these tests.

### 3.2.7 Buckling bending test

Buckling bending tests have been performed for full-Tribond specimens only. Again, two different geometries for a narrow (1.5 mm) and wide (20 mm) specimen were tested. The narrow specimen geometry is shown in Figure C.5. The wide specimen geometry was a rectangular sheet of 20 mm by 120 mm. The buckling

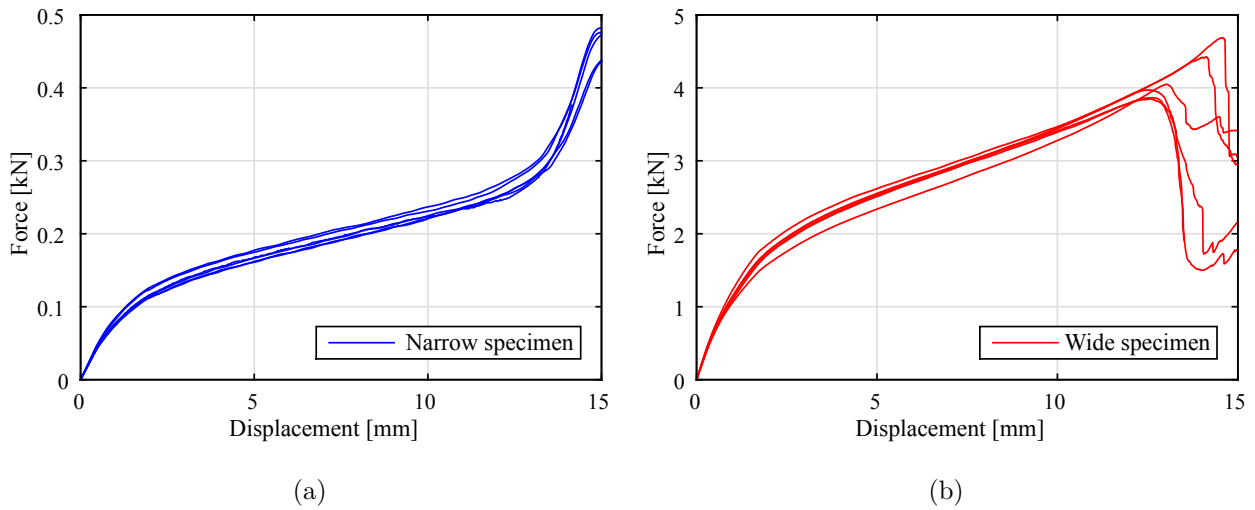


**Figure 3.11** Measured force–displacement curves of the narrow (a) and wide (b) specimen geometries of the 3-point bending test.

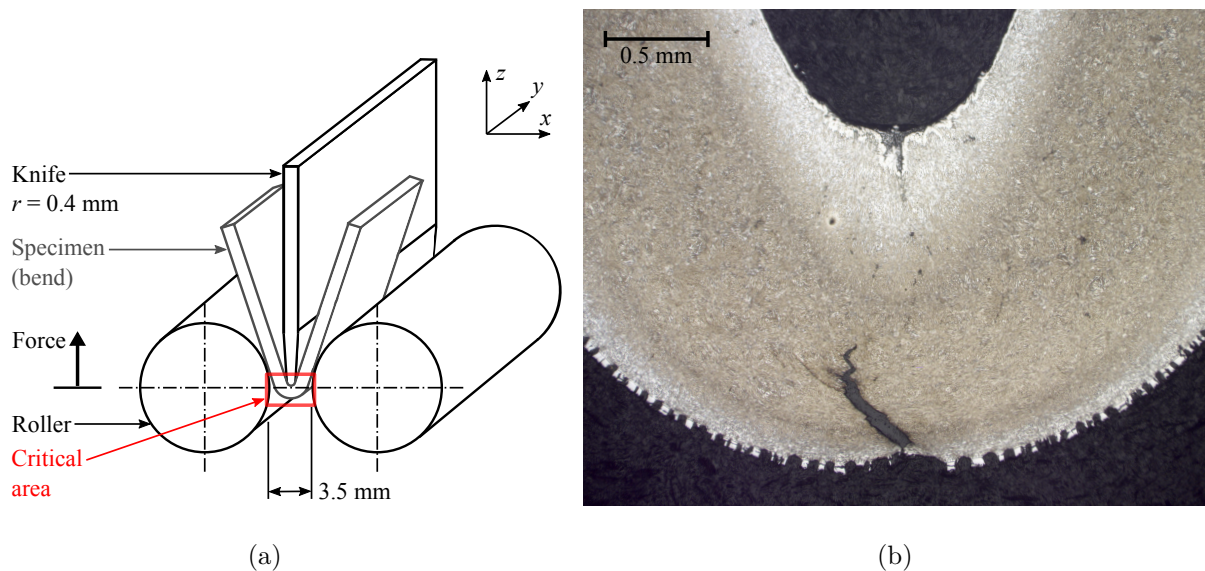


**Figure 3.12** Schematic overview of the test setup of the 3-point bending test (a), adapted from VDA 238-100 standard [31]. Micrograph of etched interrupted 3-point bending test specimen  $n4\_07$  after an initial force drop of 300 N (b).

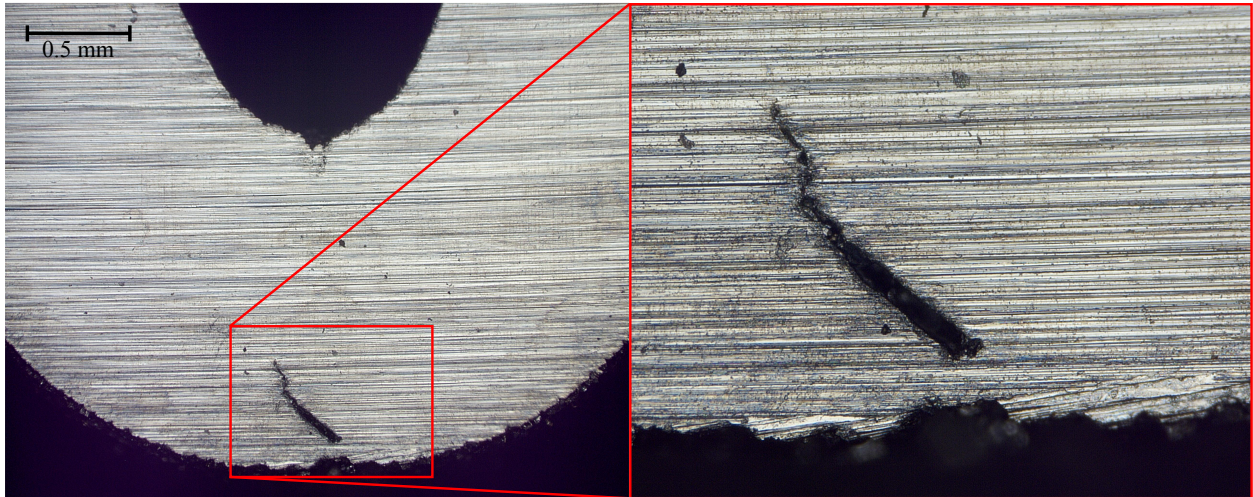


**Figure 3.13** *Micrograph of unetched interrupted 3-point bending test specimen n4\_07 after an initial force drop of 300 N with inset.*

bending test was developed by Hönle [22] as an improved frictionless version of the 3-point bending test. Henn [19] then updated the test setup for use in material model validation at Audi, the same test setup is used here.

The test setup is shown in Figure 3.15. In the setup, the specimen was given an initial deflection to enforce a well-defined buckling force peak in the force displacement curve. After some initial tests, it was found that the buckling force peak is well-defined when using an initial deflection of 2 mm. Lower initial deflections showed violent buckling during testing which gave a large variation in the height of the force peak at low deformations. The tests were performed with a quasi-static cross-head speed of  $0.5 \text{ mm s}^{-1}$ . The forces were measured with the low force load cell for the narrow specimens and the standard load cell for the wide specimens. The displacement measurement was initially performed locally, but appeared to differ less than 0.5% with the cross-head travel monitor's measurement. Therefore the travel monitor was used instead. Strain fields were measured on the outer bending surface. Just as with the 3-point bending test a crack investigation is performed. In this case, the specimen did not show any sign of fracture at the maximum displacement of 36 mm, so no interrupted bending tests were required. Instead, specimens were investigated after being subjected to the maximum displacement of 36 mm. The measured force–displacement curves of the narrow and wide specimen geometries are shown in Figure 3.14. Crack investigation micrographs of a specimen are shown in Figures 3.16. It shows that the Tribond has not yet cracked, whereas the AlSi coating has. There is a difference in fracture behavior between the 3-point and buckling bending tests even though the tests experience the same stress state. This is due to the different bending radii during testing. In the case of a 3-point bending test, the knife will enforce a sharp bend whereas in the buckling bending test a large area can deform. This means the 3-point bending test accumulates more damage and thus fractures sooner.

The buckling bending test results will be used to validate the plasticity model, they will also be used as a lower bound for the fracture validation as no fracture occurs in both the narrow and wide specimens during testing.

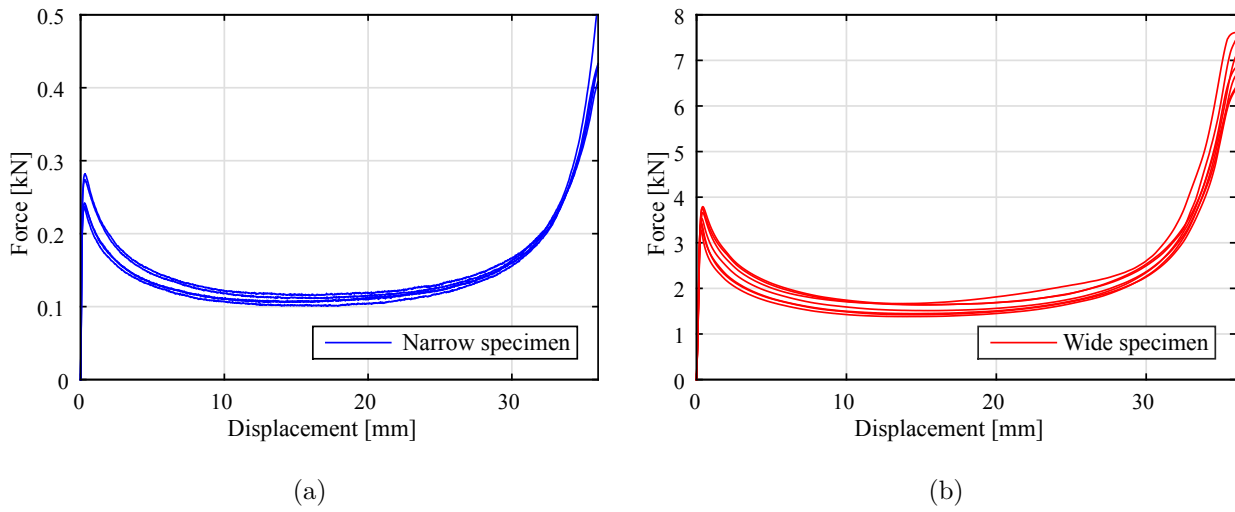


**Figure 3.14** Measured force–displacement curves of the narrow (a) and wide (b) specimen geometries of the buckling bending test.

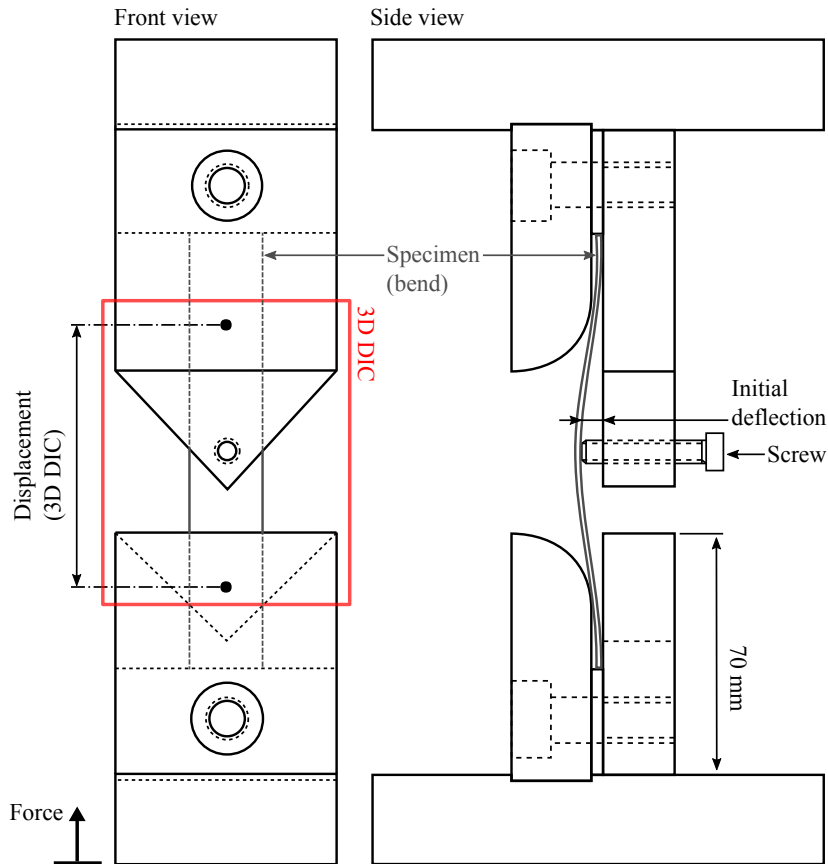


**Figure 3.15** Test setup of the buckling bending test.



**Figure 3.16** *Micrograph of unetched buckling bending test specimen n1\_03 at a displacement of 36 mm with inset.*

CONFIDENTIAL

# Chapter 4

## Material modeling

The Volkswagen Group Research's Modular Material Model (MMM) Parameter Identification Procedure (PIP) is used to calibrate the Tribond material model. The procedure was developed further to account for the varying through thickness properties of composite steels like Tribond. The original procedure was presented in Chapter 2. Calibrating the plastic behavior of the core and surface layer models is done in Section 4.2. The complete fracture model with mesh size dependency is calibrated in Section 4.3. The modeling strategy is presented in the next section.

### 4.1 Modeling strategy

Tribond is a composite steel, its material properties differ through the thickness, as illustrated in Figure 3.1. The Tribond material model should be able to approximate the specific material behavior through the thickness to accurately model in- and out-of-plane loading behavior. Similar to the simulation method of ThyssenKrupp [27], the material model varies through the thickness. Separate material models are calibrated for the core and surface layer hardness values, with a combination of both used in the transition zone. This means that the core and surface layer material models will need to be calibrated. The transition zone material properties will then be specified by an interpolation rule. This interpolation rule will, similar to the modeling strategy used by Eller [13], derive the material properties in the transition zone according to the hardness properties. The idea of a hardness driven material model is that the elastic, plastic and fracture properties in the transition zone are all linked to the material hardness. After calibrating the core and surface layer material models, the material properties are known for the maximum and minimum hardness values, respectively. With the interpolation rule, the material properties for any intermediate hardness values can be defined.

The hardness distribution is mapped by the elements of an FE model based on the averaged hardness measurements of Section 3.1, see Figure 4.1a. The mesh size is kept small in the initial material model calibration, to ensure the model can accurately map the hardness. In the used FE models, the thickness of 1.5 mm is modeled with an even sixteen elements. This results in an element size of 0.09375 mm in thickness-direction, referred to as an 0.1 mm mesh. The element distribution and hardness values are shown in Figure 4.1b. The four center elements with hardness 499 HV are pure core material. Elements 1 – 6 have transition zone hardness values and are considered transition zone material. These elements will have a mixture of core and surface layer properties. There are no elements with a surface layer hardness of 173 HV. This means there are no elements with only the surface layer plasticity model. The hardness values of each element are given in Table 4.1.

In line with the experimental test set, core-only specimens will be used to calibrate the core layer plasticity model directly. The Tribond's plasticity model will then still have unknown hardness-driven mixing rule and surface layer plasticity model parameters, which are calibrated from the full-Tribond specimens. Fracture in the core and surface layer material model is calibrated from in- and out-of-plane loading tests on full-Tribond specimens.

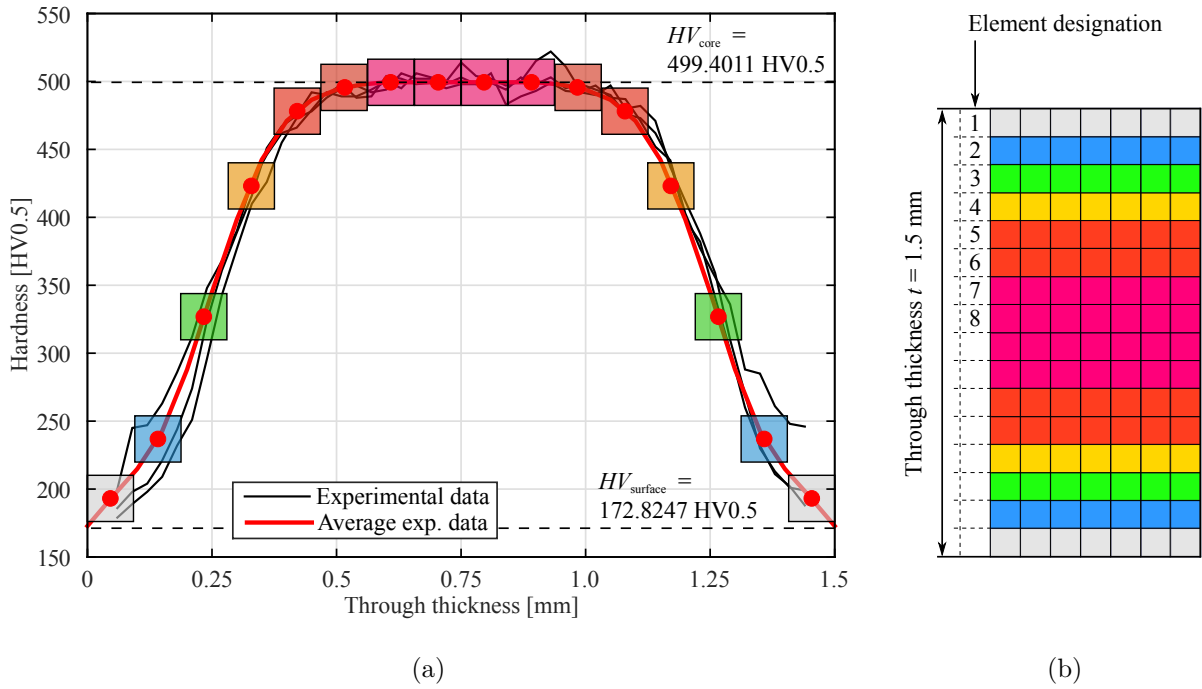


**Figure 4.1** Hardness map of the average experimental data with 0.1 mm mesh (a) and 0.1 mm FE model cross section (b).

**Table 4.1** Hardness values of a solid element FE model with a 0.1 mm mesh.

Element designation	1	2	3	4	5	6	7	8
$HV =$ Hardness [HV0.5]	192.982	237.432	327.226	423.222	477.771	495.158	499.401	499.401

## 4.2 Plasticity model

The plasticity model describes the stress–strain relationship during plastic deformation. The elastic behavior is described by Hooke’s law. After yielding, which is defined by a yield criterion, the true stress–true equivalent plastic strain relationship, which is defined by a hardening law and a mix of strain hardening curves, describes the plastic deformation.

### 4.2.1 Yield criterion

Choice of the correct yield criterion to model Tribond’s transition from elastic to plastic behavior, largely depends on the metals anisotropy. Therefore, the  $r$ -values presented in Section 3.2.1 were calculated. With  $r$ -values in the range  $0.75 < r < 0.90$ , Tribond shows only minor anisotropy in the in-plane uni-axial tensile test results. These results are for full-Tribond specimens, not for the core and surface layer materials separately. It was shown by Eller [13] that the core material’s behavior can be accurately modeled with an isotropic model. Therefore, by assuming the surface material is also isotropic, an isotropic yield criterion can be used for both plasticity models in the full-Tribond model. The isotropic Hershey yield criterion will be used, which allows for adjustment of the plane strain tension and shear yield stresses, relative to the uni-axial tension yield point. To calibrate this yield criterion, the yield stress  $\sigma_y$  and the exponent  $a$  need to be determined, see Equation 2.3. As stated before, the uni-axial and notched tensile test results will be used for this.

From the uni-axial tensile test, the yield stress  $\sigma_y$  in uni-axial tension is found. The Hershey exponent  $a$  is derived from the notched tensile test simulation results. As was shown in Section 2.2.1, the exponent affects the yield point in plane strain tension and shear. The parameter is hard to calibrate directly from the experimental results, therefore it was back-calculated by simulating a uni-axial and notched tensile test. For the first simulations, an initial, trial value of the exponent was taken from literature [13]. Considering the properties of the two metals used in Tribond, it is assumed that the harder and more abundant core layer will be leading in the height of the ultimate tensile strength (UTS). Therefore, the initial parameter  $a = 6$  is chosen, inline with the calibration of Eller [13] for 22MnB5. The parameter is validated with simulations of uni-axial and notched tensile tests of core-only and full-Tribond tests, the results are presented in Figures 4.6 and 4.11. It shows a good fit at force maximum for the core-only results, but the full-Tribond results shows the uni-axial tensile test simulation results underestimate the UTS of the average experimental results. It does however lie within the scatter of all full-Tribond specimen uni-axial tensile test experimental results.

A single Young’s modulus characterizes the elastic behavior of both the core and surface layer material. It is based on the experimental results of all uni-axial tensile tests, shown in Table 4.2. For the full-Tribond specimen an average of 182.22 GPa was calculated. This value is quite low because the specimen thickness used to calculate the Young’s modulus did not account for the AlSi coating. According to the Volkswagen internal TL 4225 norm [1], the AlSi coating forms a brittle, non load carrying surface layer with a total coating thickness of  $t_{\text{AlSi}} = 80 \mu\text{m}$ . Adjusting for this, a more accurate approximate Young’s modulus can be calculated of 192.49 GPa. Therefore, a Young’s modulus of 190 GPa is used which means the elastic behavior is underestimated. The influence of underestimating the core layer’s Young’s modulus is shown in Figure 4.2a. At an example yield stress of 1 GPa, the lower Young’s modulus decreases the error at yielding, between the simulation and average experimental data, by more than half. The error at yielding is caused by the non-linear region of the elastic behavior.

In ultrahigh-strength steels UHSS, the exact stress at which yielding occurs is hard to determine. The materials stress–strain curve does not show a clear yield point. Instead the proportional limit can be calculated with the Young’s modulus and an offset. The proportional limit is the stress at which the stress–strain curve first deviates from a straight line. The proportional limit is used to approximate the yield point. The two Tribond layers have different yield points and from the performed experiments only the yield point of the core layer can be determined directly. Therefore, the core layer yield point is determined by the experimental results of the core-only specimen results in Section 3.2.1. The measured average engineering stress–strain curve of the core-only specimens is shown in Figure 4.2b. The average yield stresses for offsets of 0.2 %, 0.1 % and 0.05 % for full-Tribond and the core layer are shown in Table 4.3. The simulation error introduced by neglecting the non-linear elastic behavior just before yielding decreases with a smaller offset. This means the assumption for fully-linear elastic behavior is more valid with a smaller offset, which also leads to a lower yield stress. In lieu of an improved elastic description, which would require a cyclic loading test [25], the offset is set to 0.05 %. Improving the elastic description could result in a higher yield stress.

	Full-Tribond	Core layer
$E_{\text{mean}}$ [GPa]	192.5 (182.2)	198.5
SD [GPa]	3.17	2.18

**Table 4.2** Average Young’s moduli and the standard deviation of the full-Tribond and the core layer material.

	Full-Tribond	Core layer
$\sigma_{y,\text{Rp}0.2}$ [MPa]	932.0	1 265.2
SD [MPa]	20.9	13.9
$\sigma_{y,\text{Rp}0.1}$ [MPa]	813.7	1 149.4
SD [MPa]	18.9	16.4
$\sigma_{y,\text{Rp}0.05}$ [MPa]	714.6	1 057.1
SD [MPa]	26.3	20.9

**Table 4.3** Average yield stress and the standard deviation of the full-Tribond and core layer material, calculated for different offsets (0.2 %, 0.1 % and 0.05 %) and with a Young’s modulus of 190 GPa.

Although, the higher yield stress would only serve to compare Tribond’s performance more easily with different materials according to the standardized 0.2 % offset rule [10]. The elastic behavior of Tribond’s surface metal cannot be characterized directly from experimental results, because no surface layer specimens were tested. However, with a single Young’s modulus for both layers already determined, only the surface’s yield stress is unknown. Therefore, the yield stress is added to the optimization parameters, to be indirectly defined in the plasticity optimization. The average full-Tribond specimen yield stresses are added to Table 4.3 for completeness. Elastic properties used in the Tribond material model are summarized in Table 4.4.

## 4.2.2 Hardening law

In this section, first the core layer and then the surface layer plastic behavior is calibrated.

### 4.2.2.1 Core layer

The process to calibrate the core layer plastic behavior is analog to the standardized process shown in Figure 2.7. The result is a hardening curve for the core layer material. From the core-only specimen results, it is possible to directly determine the first part of the hardening curve. This is done by taking the experimental true stress–true equivalent plastic strain results of the uni-axial tensile test, see Figure 4.3a. These results only define the plastic behavior up to a true plastic strain of  $\bar{\epsilon}_p = 0.035$ . This is because the true stress–true plastic strain calculations are only valid up to force maximum. To determine the rest of the strain hardening curve, the experimental results need to be extrapolated. This is done by fitting the Swift and Voce hardening laws to the last 70 % of the experimental data. Changing this percentage influences the smooth transition point between the Swift and Voce extrapolation mix and the experimental results. A high percentage was used to shift the transition point to a lower plastic strain, which meant a larger part of the

**Table 4.4** Elastic properties used in the Tribond material model, calculated with  $E = 190$  GPa and an offset of 0.05 %, the surface layer yield strength was determined later.

	Core layer	Surface layer
Yield strength $\sigma_y$ [GPa]	1 057.1	(310.2)
Young’s modulus, $E$ [MPa]	190	190

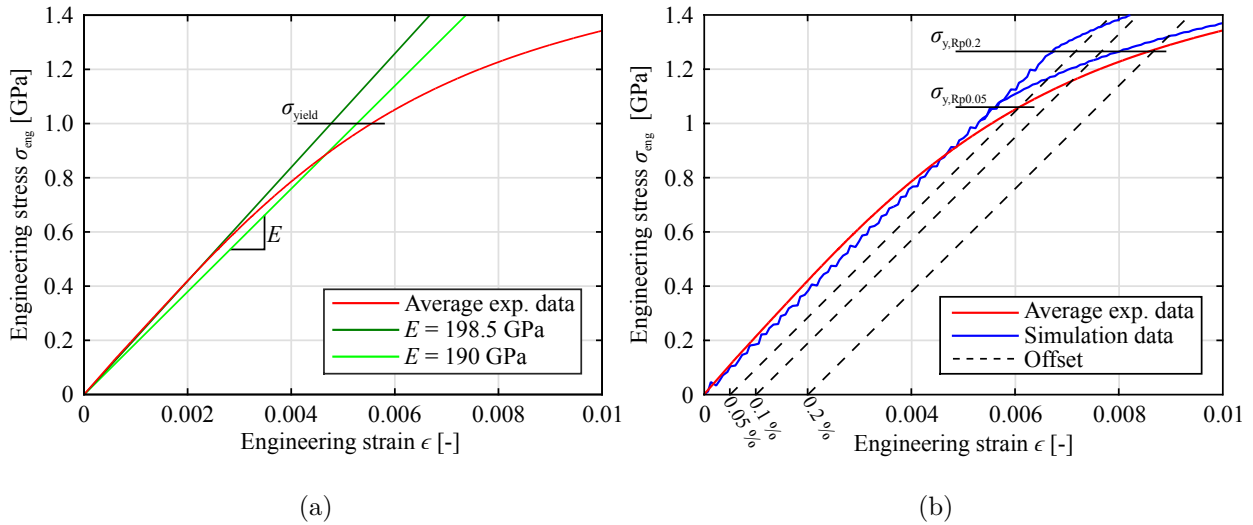


**Figure 4.2** Average experimental engineering stress–strain curve of the core-only specimens, illustrating the influence of underestimating the Young’s modulus (a) and of varying the offset (b).

hardening curve was variable during the optimization. This was used as a strategy to try and shift the start of localized neck forward in the uni-axial tensile test simulation results. With the current fit, this transition point lies at  $\bar{\epsilon}_p = 0.029$ , see the dotted lined in Figure 4.3b.

To determine the extrapolated hardening curve, a mix of both the Swift and Voce law extrapolations is calibrated in an inverse FEM optimization, see Equations 2.4 and 2.5. As stated before, a non-linear mixing rule is used to mix the Swift and Voce law extrapolations. The optimization parameters are defined in Equation 2.7. The non-linear mixing rule parameters  $\lambda_{\text{initial}}$ ,  $\lambda_{\text{final}}$  and  $\alpha_{\text{shape}}$  are the unknowns which need to be calibrated. The optimized hardening curve will lie somewhere in between a purely Swift or Voce law extrapolation. To validate these upper and lower bounds of the hardening curve, simulations of the uni-axial and notched tensile tests are performed with purely Swift and Voce law extrapolations in the hardening curve, see Figure 4.4. The FE simulations are performed with so called under-integrated 8-node solid elements, they have one integration point combined with the artificial stiffness method [14], which gives hourglass control. This integration method is also referred to as the uniform reduced integration (URI) method. The simulation results show a corridor within which the measured force–displacement curves lie after necking. This means that the Swift and Voce extrapolations are indeed an upper and lower bound to the actual hardening curve.

In the optimization, the objective function will minimize the difference between the experiments and simulations at a set of sample points. Four sets of sample points are obtained from the average force–displacement curves of the uni-axial and notched tensile tests and two true total strain curves of the notched tensile test. Since the measured strain hardening curve of the uni-axial tensile test is used until force maximum, the optimization only influences the behavior after a plastic strain of  $\bar{\epsilon}_p = 0.029$ . Therefore, the sample points are chosen after force maximum in the uni-axial and notched tensile tests. Figures 4.5a and 4.5b show the sample points for fitting the force–displacement curves. In total, 40 sample points are used, but for clarity only 10 are shown. Figure 4.5b also shows the true total strain curve comparison points. The comparison points are at force maximum ( $d = 0.52$  mm) and after the initiation of localized necking ( $d = 0.55$  mm). The total strain curve sample points compare the total strain in  $x$ -direction along the longitudinal axis of symmetry on the surface of the notched specimen, see Figure 4.5c. The measured true total strain curves and sample points are also shown in this figure. The displacements for which the strain fields are shown correspond to the comparison points at force maximum and in the neck.

With the unknown hardening parameters and the objective function defined, the optimization for Tribond’s core layer hardening curve can be performed. The optimization results are given in Table 4.5. The table also shows the parameters that were fitted directly to experimental data. The simulated force–displacement curves and true total strain curves are shown in Figure 4.6. The simulation results show a good fit for the uni-axial and notched tensile test force–displacement curves. The uni-axial tensile test simulation overestimates the measured displacement at which necking occurs. The fit is however still considered good, because the experimental data was influenced by weak spots in the specimens, which was discussed

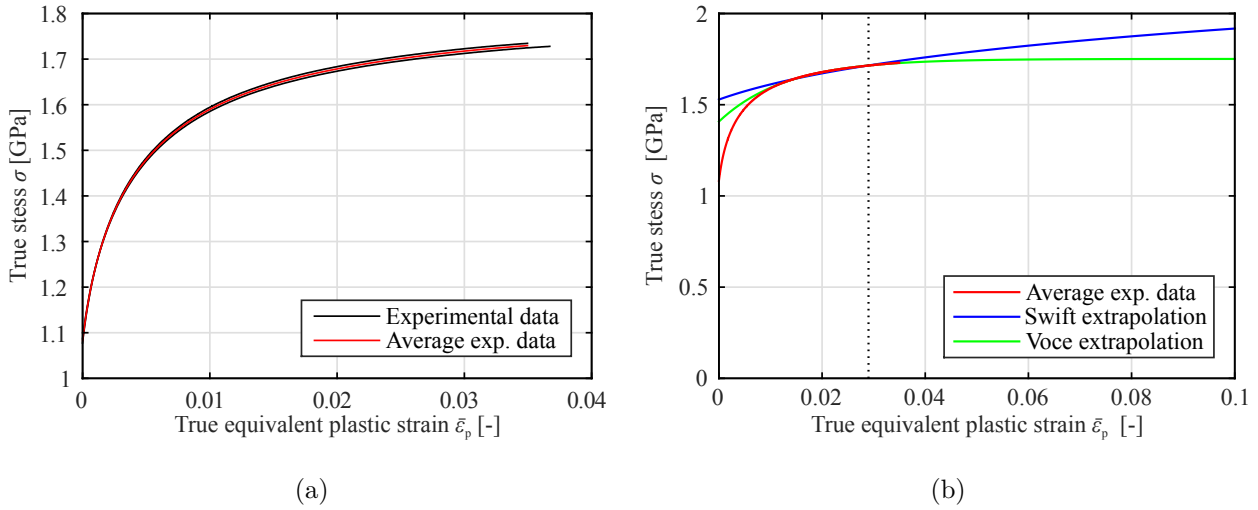


**Figure 4.3** Experimental core layer true stress–true equivalent plastic strain data of the uni-axial tensile test (a) with the Swift and Voce law extrapolations, where the dotted line marks the smooth transition point at  $\bar{\epsilon}_p = 0.0029$  (b).

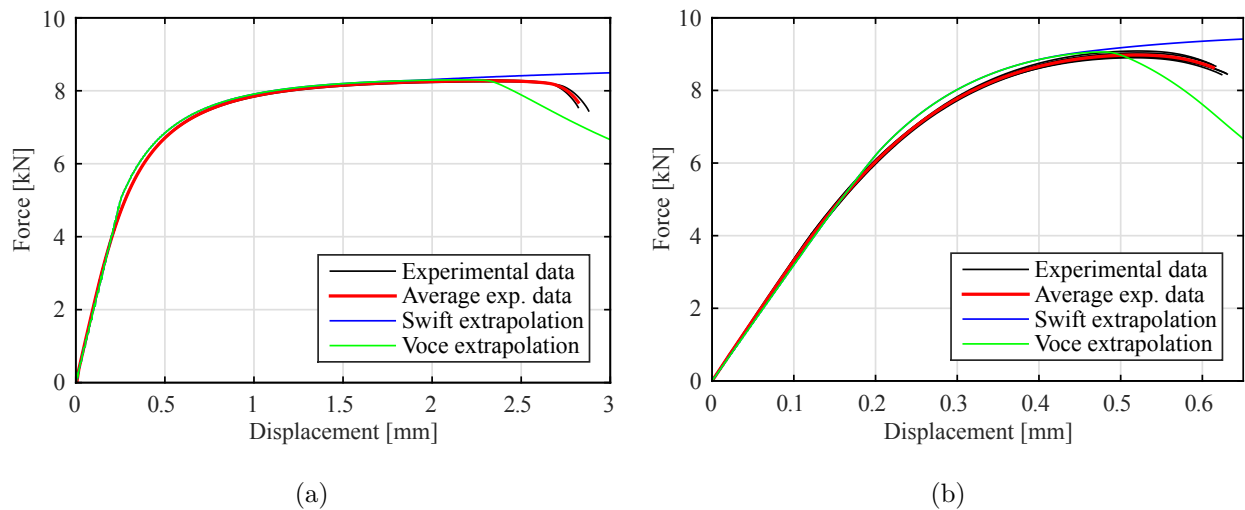


**Figure 4.4** Corridor check between the simulated force–displacement curves of purely Swift and Voce law extrapolations for the hardening curve of the uni-axial (a) and notched tensile test (b).

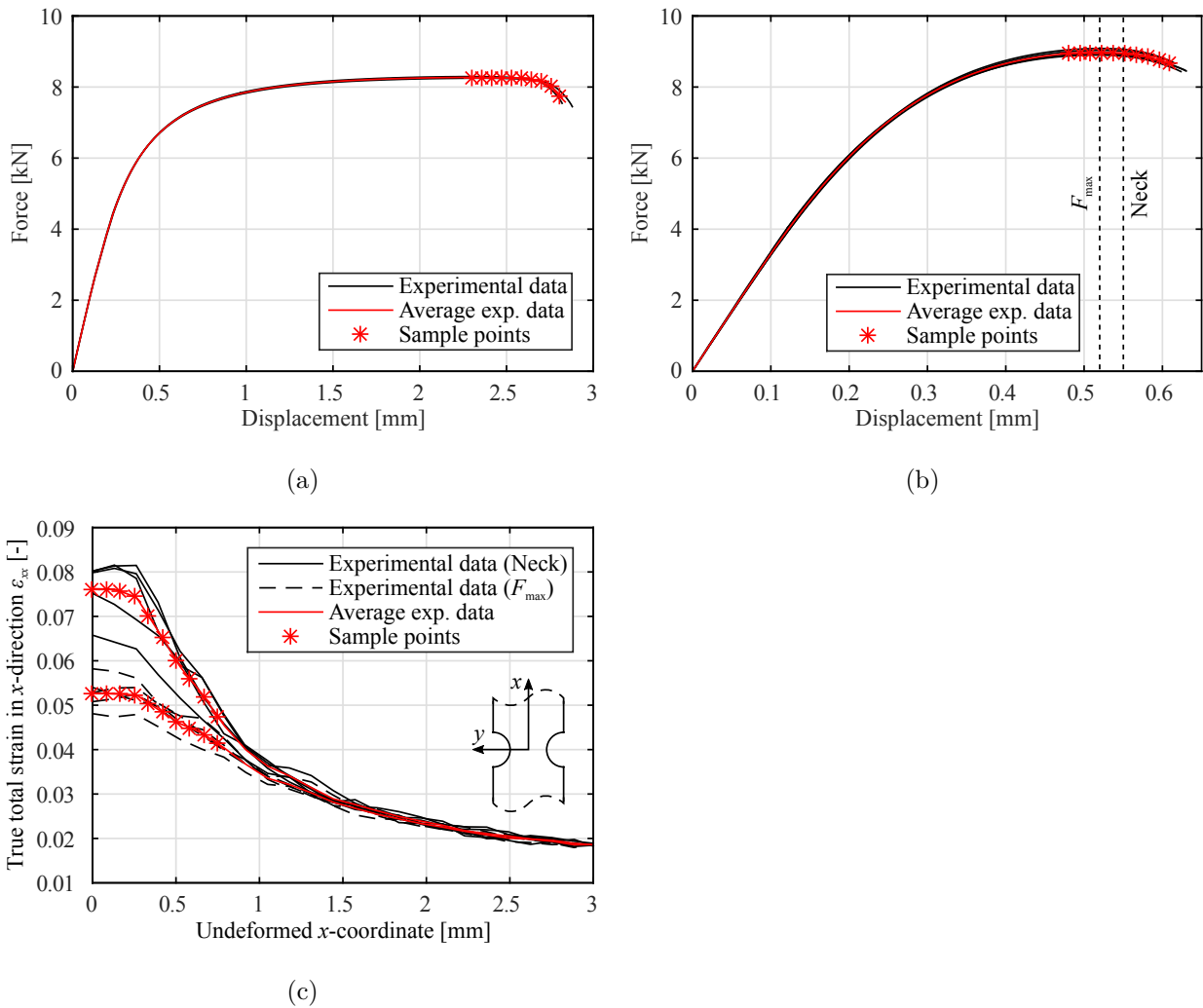


**Figure 4.5** Sample points in the core-only experimental results: on the measured force–displacement curves of the uni-axial (a) and the notched tensile tests (b) and on the measured true total strain curves of the notched tensile test along the undeformed  $x$ -coordinate (c).

**Table 4.5** Calibration results of the core layer plasticity optimization.

	Fitted directly to experimental data					Optimization results			
	$k_S$	$\varepsilon_{0,S}$	$n_S$	$\varepsilon_{0,V}$	$k_V$	$n_V$	$\lambda_{\text{initial}}$	$\lambda_{\text{final}}$	$\alpha_{\text{shape}}$
	[GPa]	[-]	[-]	[-]	[GPa]	[-]	[-]	[-]	[-]
Core layer	2.4860	0.0183	0.1216	1.4076	0.3435	77.7716	0.6354	0.6380	0.4326

in Section 3.2.1. These weak spots were shown to decrease the displacement at which necking occurred. The results for the notched tensile test are better, predicting the necking point more accurately. These experimental results were not influenced by weak spots, because in these tests the point of strain localization was predefined. The predicted true total strain curve of the notched tensile test during necking does not fit the average experimental data as well as the true total strain curve at force maximum. Although, the simulation results do lie within the experimental data range. In the neck, the simulated total strain peak is narrower and higher than the experimental data, suggesting strains localize more strongly in the simulation. The overall better fit of the notched tensile test results is due to the objective function used to calibrate the model. Of the four sets of sample points used in the optimization, only one is from the uni-axial tensile test results. Therefore, its fit is given less priority than that of the notched tensile test. In both force–displacement curves, the simulation results continue on after the experimental results end, because no fracture behavior has been specified yet. The optimized hardening curve and the mixing rule parameter  $\lambda_V$  are shown in Figure 4.7. Figure 4.7b shows that the mixing parameter is practically constant, only varying 0.2% over a true equivalent plastic strain range of  $0 \leq \varepsilon_p \leq 2$ . It is likely that a linear mixing rule would also be able to solve the optimization adequately, however this optimization is not performed.

The plasticity model is validated with a side-by-side comparison of the total strain fields on the specimen surface of the simulation and experimental results, see Figure 4.8. The facet size in the DIC used to calculate the strain field is comparable to the element size used to get the simulation results. The strain fields at force maximum compare well, but during necking this is less so. The simulated strain fields during necking show the same difference in total strain peak height and width as Figure 4.6c. The simulation slightly overestimates the maximum strain, but underestimates the area that experiences localized necking. After the plasticity calibration of the core layer, the next step is to calibrate the hardening curve of the surface layer.

#### 4.2.2.2 Surface layer

The two step standardized process used for the core layer calibration required core-only experimental results for both steps. The first step determined material parameters directly, i.e. the Young’s modulus, yield point and strain hardening law parameters. The second step calibrated the material parameters indirectly in an inverse FEM optimization, i.e. the non-linear mixing rule parameters. The results of the core layer calibration are shown in Tables 4.4 and 4.5. For the surface layer, there are no surface-only experimental results, but there are full-Tribond results. According to the modeling strategy, the plasticity properties of Tribond are specified by the core and surface layer models and a hardness driven mixing rule. Therefore, the surface layer plasticity model and the mixing rule are calibrated from full-Tribond specimen results.

The mixing rule specifies the transition zone plastic behavior by interpolating between the core and surface layer plasticity models. An initial assumption for the hardness driven mixing rule is based on the 22MnB5 calibration by Eller [11]. Here, the material hardness was assumed to be linearly related to the hardening properties. The transition zone plastic behavior varies with the hardness, it is specified as a linear combination of the core ( $\sigma_{\text{core}}$ ) and surface layer ( $\sigma_{\text{surface}}$ ) true stress responses. The transition zone mixing rule is:

$$\sigma_{\text{tz}} = f_{\text{core}} \cdot \sigma_{\text{core}} + (1 - f_{\text{core}}) \cdot \sigma_{\text{surface}} \quad (4.1)$$

where the mixing parameter is:

$$f_{\text{core}} = \frac{HV - HV_{\text{surface}}}{HV_{\text{core}} - HV_{\text{surface}}} \quad (4.2)$$

where  $HV$  is an elements hardness,  $HV_{\text{surface}} = 172.8 \text{ HV}0.5$  and  $HV_{\text{core}} = 499.4 \text{ HV}0.5$ , see also Table 4.1.

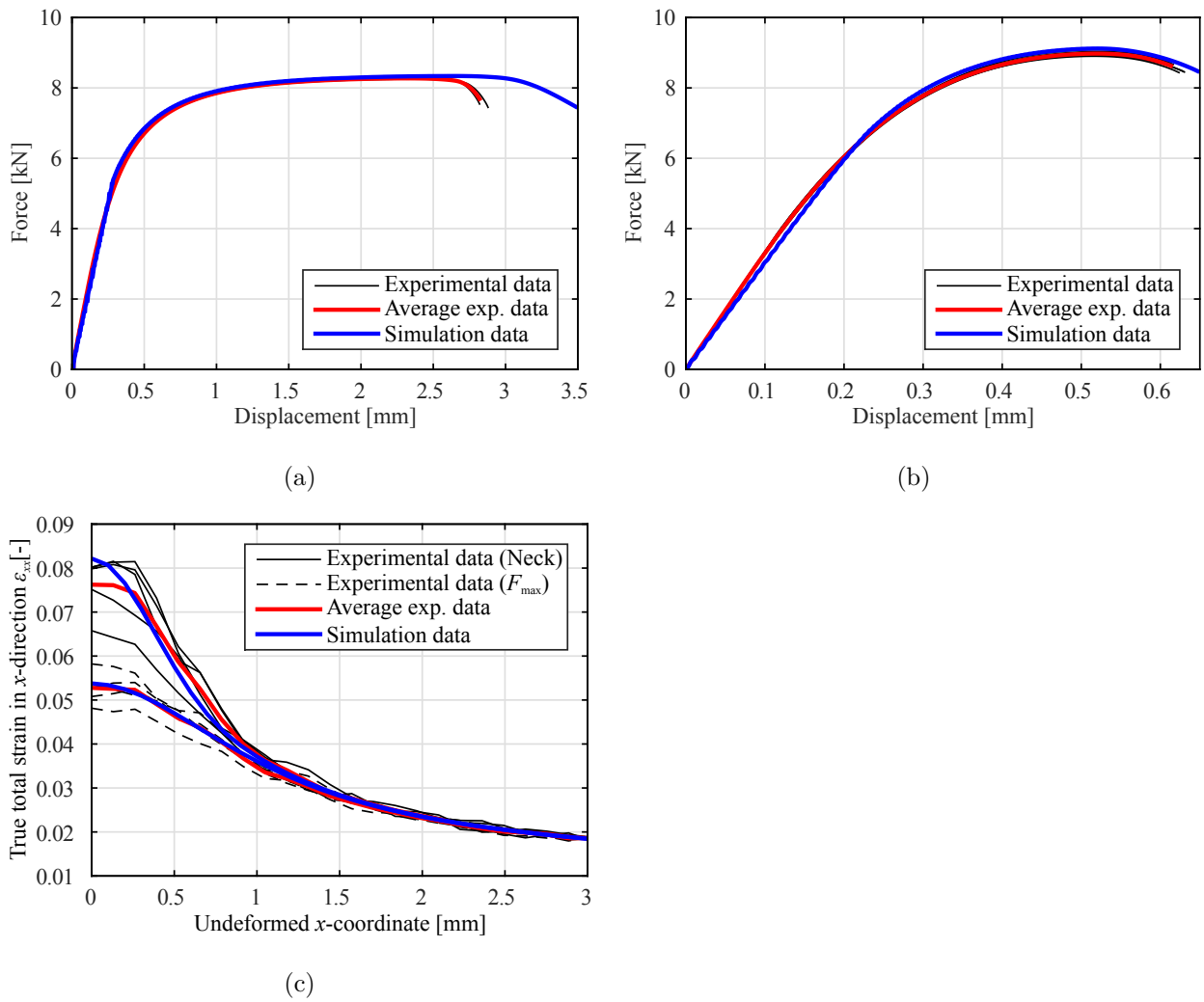


**Figure 4.6** Core layer plasticity optimization results and the core-only experimental results: the measured force-displacement curves of the uni-axial (a) and the notched tensile tests (b) and the measured true total strain curves along the undeformed x-coordinate of the notched tensile test (c).

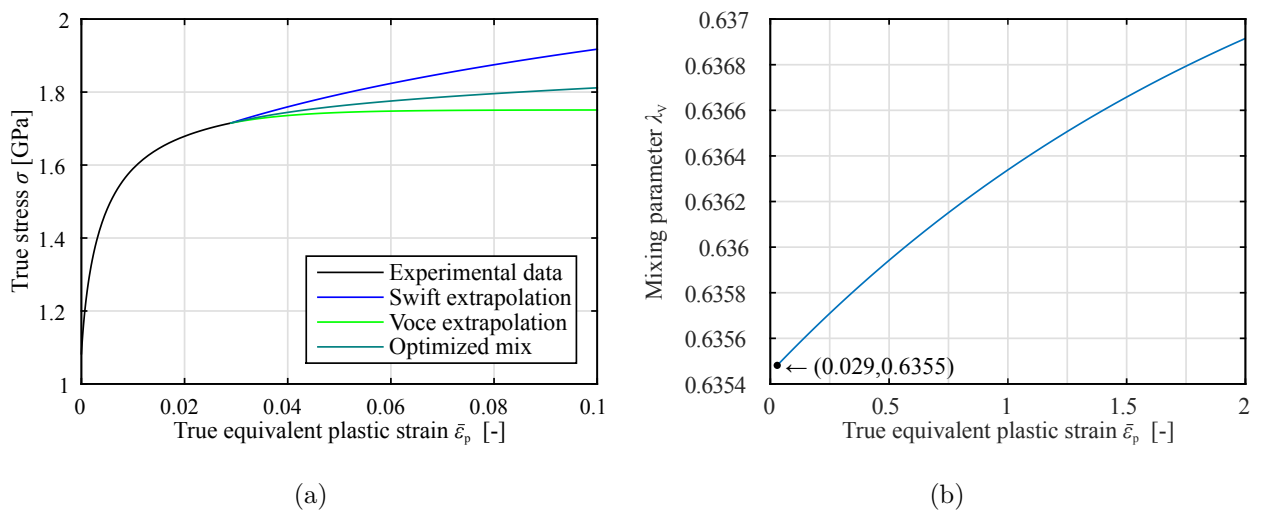


**Figure 4.7** Hardening curve for purely Swift and Voce law extrapolations with the optimized mixing rule (a) and the mixing parameter  $\lambda_V$  (b).

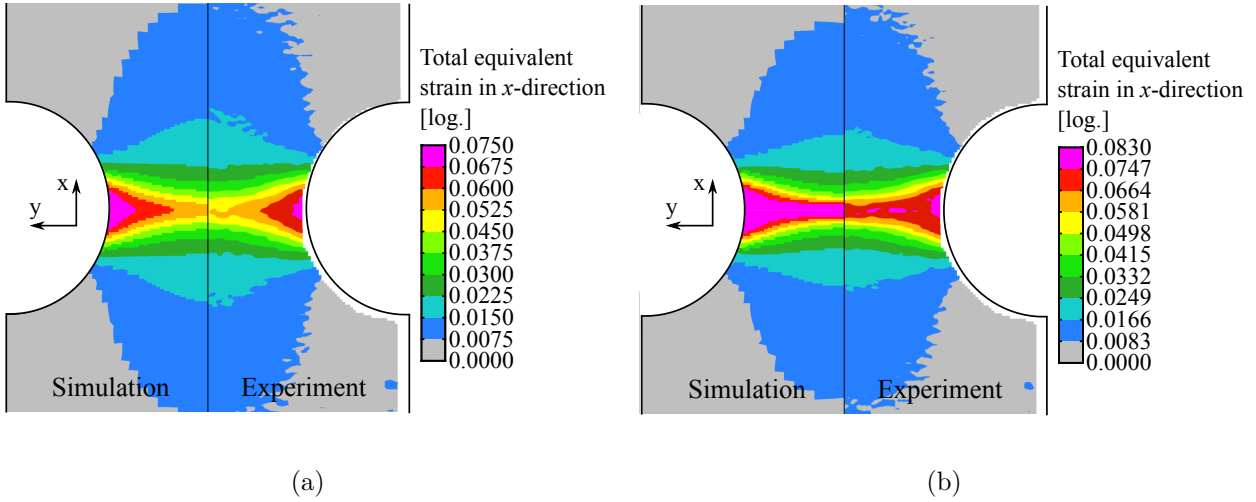


**Figure 4.8** Side-by-side comparison of the strain fields on the surface of a core-only notched tensile test specimen at force maximum  $d = 0.52$  mm (a) and during localized necking  $d = 0.55$  mm (b).

The unknown surface layer plasticity model is calibrated in the PIP. Figure 4.9 shows the updated calibration process of Figure 2.7. Here, the unknown calibration parameters are shown in red. A major difference when calibrating the surface layer plasticity is the amount of optimization parameters. Without experimental data, the yield stress  $\sigma_y$  and the initial stress-strain relationship  $\sigma_{\text{initial}}(\bar{\varepsilon}_p)$  of the hardening curve cannot be determined directly. This means there is no data for the Swift and Voce laws to be fitted to. Therefore, all of these hardening curve parameters as well as the yield stress need to be determined indirectly in the inverse FEM optimization. The hardening curve will now be a mix of only the Swift and Voce hardening laws, unlike the core calibration (Figure 2.6) it will not transition from experimental data to extrapolation data. The current optimization problem has ten parameters, nine specified in Section 2.2.2 and the unknown surface layer yield stress. An important factor in the computation time of the optimization procedure is the amount of optimization parameters. Therefore, to make the optimization more efficient and keep the computation time at an acceptable level, some simplification is required. The six unknown parameters of the Swift and Voce hardening laws can be reduced by using the condition that the hardening curve  $\sigma(\bar{\varepsilon}_p)$  starts at the yield point  $\sigma_y$ . This means that the true stress equals the yield stress at a true equivalent plastic strain of  $\bar{\varepsilon}_p = 0$ . The Swift and Voce laws become:

$$\sigma_S(0) = \sigma_y = k_S (0 + \varepsilon_{0,S})^{n_S} = k_S (\varepsilon_{0,S})^{n_S} \quad (4.3)$$

$$\sigma_V(0) = \sigma_y = \varepsilon_{0,V} + k_V (1 - e^{-n_V \cdot 0}) = \varepsilon_{0,V}. \quad (4.4)$$

These yield the conditions:

$$k_S = \frac{\sigma_y}{(\varepsilon_{0,S})^{n_S}} \quad (4.5)$$

$$\varepsilon_{0,V} = \sigma_y \quad (4.6)$$

which reduce the amount of unknowns by two. To further reduce the amount of unknowns, the non-linear mixing rule, which proved unnecessary for the core layer hardening curve, will become a linear rule Equation 2.6 then becomes:

$$\sigma = \alpha_V \cdot \sigma_V + (1 - \alpha_V) \cdot \sigma_S \quad (4.7)$$

where  $\alpha_V$  is the linear mixing rule parameter. This parameter is constant, instead of depending on the true equivalent plastic strain and the three parameters used in the non-linear mixing rule. With these simplifications, the ten parameter optimization problem has reduced to a six parameter problem, the parameters  $\varepsilon_{0,S}$ ,  $n_S$ ,  $k_V$ ,  $n_V$ ,  $\sigma_y$  and  $\alpha_V$ .

The optimization procedure will again optimize an objective function with sample points comparing experimental data and simulation data. In this case, the experimental data are the uni-axial and notched tensile test results of full-Tribond specimens. The sample points will be spread over the complete plastic range of the experiments, because the complete surface layer hardening curve needs to be calibrated. The

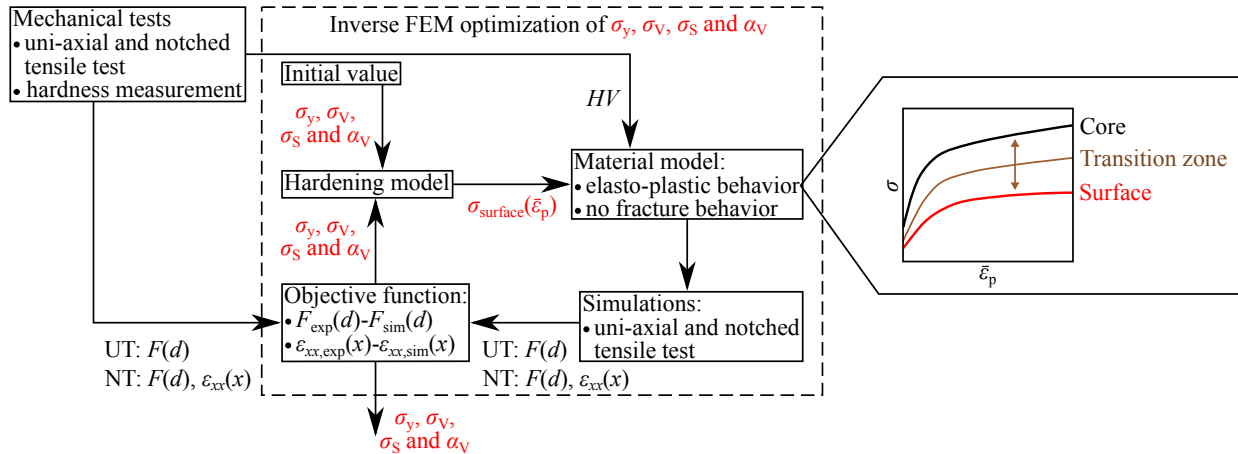


**Figure 4.9** Flow diagram of the inverse FEM optimization to determine the unknowns of the surface layer hardening curve and transition zone mixing rule.

yield point in the Tribond specimens is specified by the proportional limit calculated with an offset of 0.05 %, see Table 4.3. The force–displacement curves of both the uni-axial and notched tensile tests and the total strain curves in  $x$ -direction are shown in Figure 4.10. Again, the dotted lines in Figure 4.10b indicate the displacements of the total strain curves in Figure 4.10c, and for clarity only 10 of the 40 sample points are shown.

The results of the inverse FEM optimization of the surface layer are given in Table 4.6 and are plotted in Figure 4.11. The values which specify the hardening curve were determined by optimization with loose bounds. This shows in the relatively large initial strain of the Swift hardening law  $\varepsilon_{0,S}$ . The Swift hardening law parameters might have been more in keeping with expectations if the initial strain  $\varepsilon_{0,S}$  parameter had been determined from Equation 4.3 instead of the parameter  $k_S$ . The force–displacement curve of the uni-axial tensile test simulation deviates from the average experimental data. The force magnitude during plastic deformation is influenced by the yield stress. It appears that in this case, the yield stress was not chosen high enough to accurately predict the force maximum without negatively influencing the height of the notched tensile test simulation. The relative heights of the yield stresses and by extension the force–displacement curves, are prescribed by the Hershey exponent  $a$ . To increase the uni-axial tension test force level at force maximum, the Hershey exponent would need to increase. The simulation results of the uni-axial tensile test are also compared to all experimental results, see Figure 4.11b. This shows the scatter between the specimens. The average curve was not based on all this data, but on the data with the largest fracture displacements, to allow for a better representation of the necking behavior. The force–displacement curves extracted in different rolling directions were not used as these would not represent the weakest direction in the sheet. The differences in maximum force is less than 5 % and the difference in the point of necking is less than 30 %, both are approximated well enough to accept the calibration result. The force-displacement curve and the total strain curves of the notched tensile test show a good fit. For the total strain curve during necking, the simulation data does not fit as accurately to the average experimental data, although it does not lie far outside the experimental data range. In this case, the double peak in the measured total strain curve is not represented accurately by the simulation. The notched tensile test results are more accurate than those of the uni-axial tensile test, because they are again represented by more sample points in the optimization. This could have been compensated by adding a weighting factor to increase the importance of fitting the uni-axial tensile test results. However, because of the weak spots and the accompanying high scatter in the experimental results of the uni-axial tensile tests this was not done. The surface layer hardening curve is shown in Figure 4.12a and both the core and surface layer hardening curves are shown in Figure 4.12b. This figure gives insight into the interpolated transition zone hardening curve, which must lie in between these upper and lower bounds.

The Tribond plasticity model is validated with a side-by-side comparison of the total strain fields on the specimen surface of the simulation and experimental results, see Figure 4.13. The strain fields at force maximum ( $d = 0.51$  mm) compare well, but during necking ( $d = 0.62$  mm) this is less so. The simulated strain fields in the neck show the same difference in total strain peak height and width as Figure 4.11d. The simulation does not accurately capture the two peaks in the strain field.

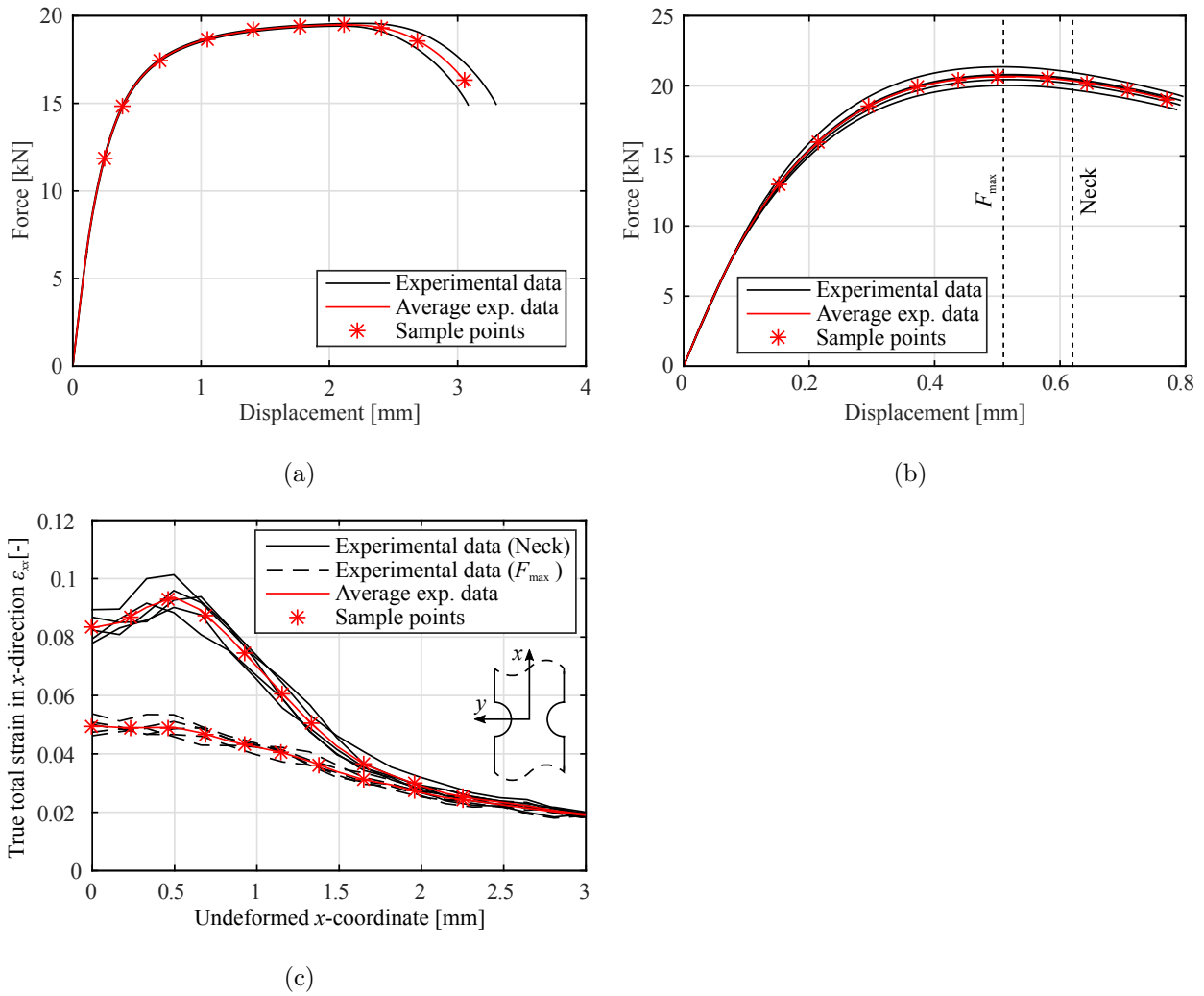


**Figure 4.10** Sample points in the full-Tribond experimental results: on the measured force–displacement curves of the uni-axial (a) and the notched tensile tests (b) and on the measured true total strain curves of the notched tensile test along the undeformed  $x$ -coordinate (c).

**Table 4.6** Calibration results of the surface layer plasticity optimization.

	$\varepsilon_{0,S}$	$n_S$	$k_V$	$n_V$	$\sigma_y$	$\alpha_{\text{shape}}$
	[-]	[-]	[GPa]	[-]	[MPa]	[-]
Surface layer	0.5937	0.0058	0.6695	25.93	310.2	0.2423

With the Tribond elasto–plastic material behavior modeled, the next step is to calibrate fracture. Fracture is calibrated with the full-Tribond specimen results of the other mechanical tests. After calibrating fracture these tests will be simulated, the simulation results are presented in Appendix F. These fracture plots are used to validate the elasto–plastic behavior model calibrated in this section, this is discussed further in Section 4.3.4.

## 4.3 Fracture model

Solid element FE models are used for the fracture model calibration. The fracture model describes the damage accumulation during plastic deformation and the point at which the damage reaches a critical value. As an element reaches a critical damage value, it is eliminated from the model. This section describes the calibration of the core layer fracture model and the different approaches used to calibrate the surface layer fracture model. The basics of the fracture modeling strategy are presented in the next section.

### 4.3.1 Fracture modeling strategy

To represent fracture in the Tribond material model, mMC fracture surfaces for the core and surface layer will be calibrated, as well as the mixing rule for the mMC fracture surfaces of the transition zone. In different mechanical tests, fracture was only observed in the UT, NT, CH, BT, SH and BE20 tests, see Table 4.7. The UT test results showed fracture, but are not used to validate the calibrated fracture behavior. This is due to the experimental results being influenced by weak spots, which lead to inaccurate fracture displacements.

In the tests that do show fracture, a distinction can be made between in- and out-of-plane loading. Tests that fail due to in-plane loading are assumed to have failed in the core. These tests can therefore be used to calibrate the core layer fracture surface: the NT, CH, BT and SH tests. The BE20 specimens fail due to out-of-plane bending. In the case of a monolithic steel, fracture would occur in the outer bending fiber. For a composite steel like Tribond, the exact fracture behavior due to out-of-plane bending is unknown. Therefore, a detailed investigation on the fracture behavior under out-of-plane bending was performed, see Section 3.2.6. The results showed that the BE20 test is the only test which fails in the transition zone. Therefore, these experimental results are the only source for transition zone fracture properties. The transition zone properties are defined by both the core and surface layer fracture models and the hardness driven mixing rule. Therefore, the BE20 experimental results are used to calibrate the core layer fracture model and the mixing rule for the transition zone properties. Fracture models are calibrated for different mesh sizes. The optimization is first performed for a 0.1 mm mesh and then for coarser 0.2 mm and 0.5 mm mesh sizes.

### 4.3.2 Core layer

To calibrate the core layer fracture model, the mMC fracture surface will be fit to the test results of the NT, CH, BT, SH and BE20 tests. The BE20 test is also added to the fitting routine, to assure fracture does not occur in the core layer before the transition zone has a chance to fracture. However, it will only be a lower bound to the core layer mMC fracture surface. The six parameters which need to be calibrated for the core layer fracture model are given in Equation 2.11. A fracture surface is calibrated with a mixture of experimental and simulation results. The experimental results specify the fracture displacement. The experiments are used to find the average displacement at which fracture occurs under different loading states, see Table 4.7. The simulation results specify the hardening curve and the stress state traces in each element as a function of the plastic deformation. The hardening curves of the core and surface layer plasticity models are shown in Figure 4.12b. The stress state traces of the core elements of the NT, CH, BT, SH and

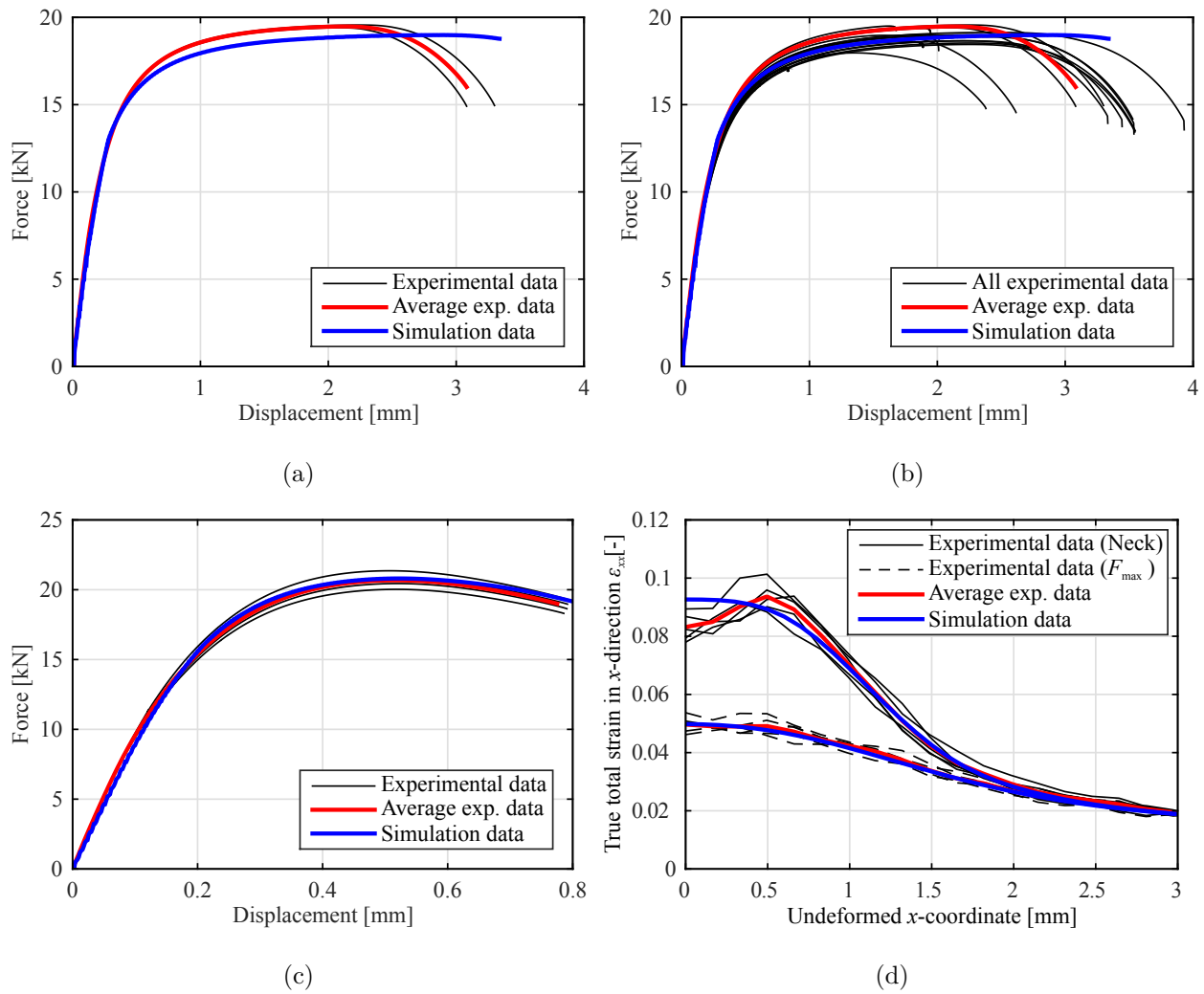


**Figure 4.11** Surface layer plasticity optimization results and the full-Tribond experimental results: the measured force–displacement curves of the uni-axial (a,b) and the notched tensile tests (c) and the measured true total strain curves along the undeformed x-coordinate of the notched tensile test (d).

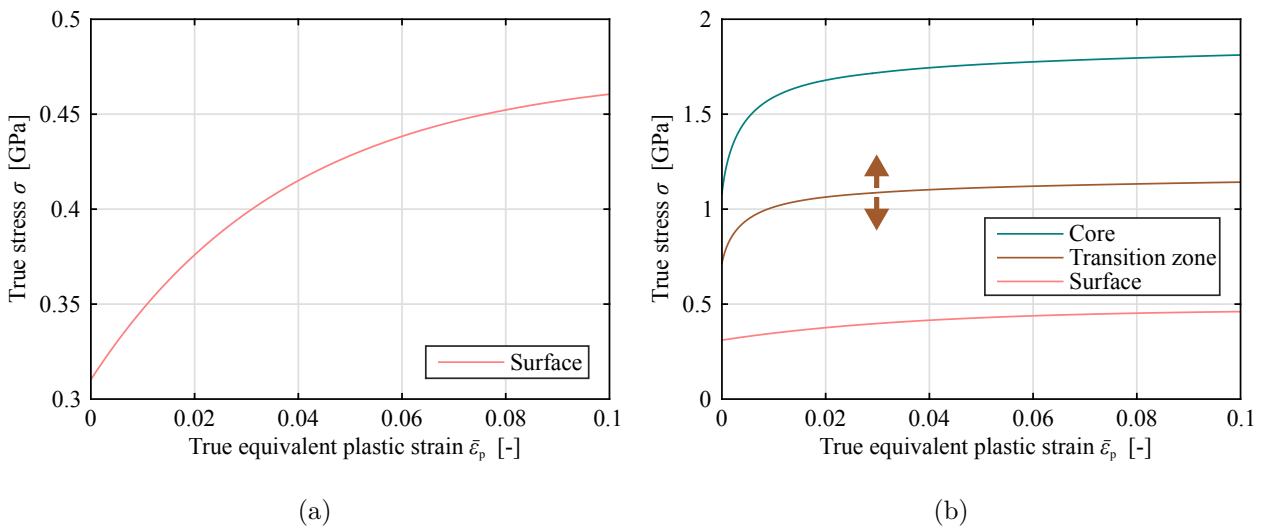


**Figure 4.12** The optimized surface layer hardening curve (a) and the core and surface layer hardening curves with example transition zone hardening cure (b).

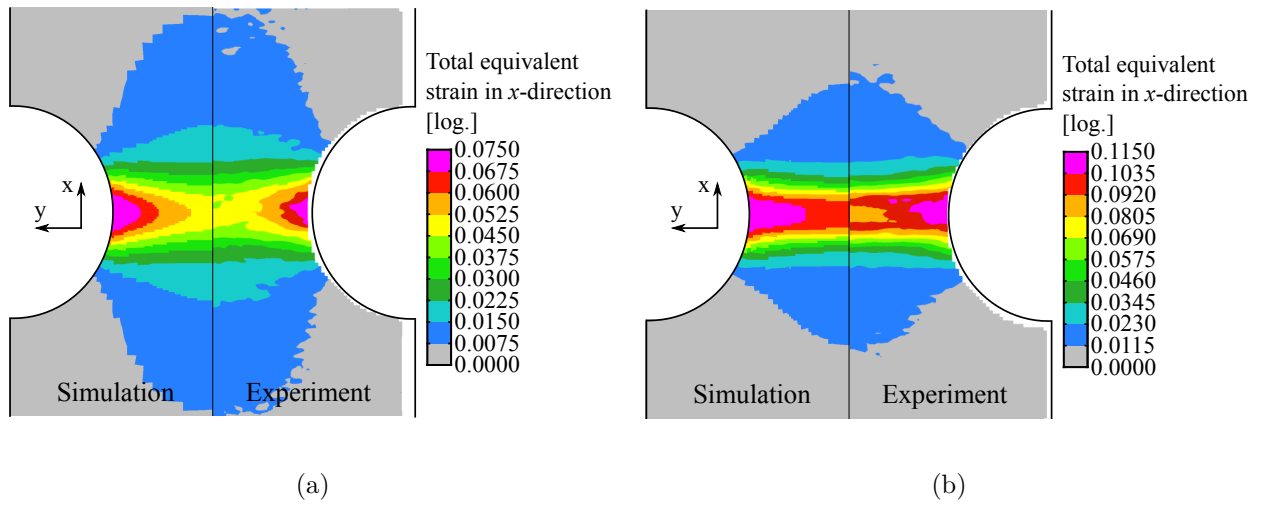


**Figure 4.13** Side-by-side comparison of the strain fields on the surface of a full-Tribond notched tensile test specimen at force maximum  $d = 0.51$  mm (a) and during localized necking  $d = 0.62$  mm (b).

**Table 4.7** Overview of the mechanical tests used for calibration and validation of the fracture behavior.

Mechanical test (abbr.)	Fracture location	Fracture displacement $d_{\text{frac}}$ [mm]	Purpose
Uni-axial tensile (UT)	core	3.19 (inaccurate)	-
Notched tensile (NT)	core	0.79	$\varepsilon_{f,\text{core}}(\eta, \bar{\theta})$
Central hole tensile (CH)	core	0.97	$\varepsilon_{f,\text{core}}(\eta, \bar{\theta})$
Bulge test (BT)	core	19.94	$\varepsilon_{f,\text{core}}(\eta, \bar{\theta})$
Shear (SH)	core	0.88	$\varepsilon_{f,\text{core}}(\eta, \bar{\theta})$
3-Point bending, narrow specimen (BE1.5)	no fracture		validation
3-Point bending, wide specimen (BE20)	transition zone	12.63 (13.3)	$\varepsilon_{f,\text{core,min}}(\eta, \bar{\theta})$ , $\varepsilon_{f,\text{surface}}(\eta, \bar{\theta})$ , $\varepsilon_{f,\text{tz}}(\eta, \bar{\theta})$
Buckling bending, narrow specimen (BB1.5)	no fracture		validation
Buckling bending, wide specimen (BB20)	no fracture		validation

**Table 4.8** Calibration parameters of the core layer mMC fracture model for a 0.1 mm mesh.

	$k_S$ [GPa]	$n_S$ [-]	$c_1$ [-]	$c_2$ [GPa]	$c_3$ [-]	$c_4$ [-]
core layer	2.371	0.08954	0.07987	1.296	0.9380	1.066

BE20 tests in which fracture initiates are shown in Figure 4.14. The stress state traces of all elements of the BE20 test in which fracture might initiate are shown in Figures E.1 and E.2.

The standard optimization method used at the Volkswagen Group to fit the mMC fracture surface is used for fitting the core layer fracture model. First, the hardening curve is used to fit the factor  $k_S$  and the exponent  $n_S$  of the Swift hardening law. These are not the values specified in Section 4.2.2.1, but are the results of fitting a pure Swift law to the full hardening curve of the core. This is the results of the mMC model defined by Bai [6] being derived with the Swift hardening law. Then, the stress state traces are used to calibrate the parameters  $c_{1-4}$ . Sets of stress state traces are created by simulating the different mechanical tests with the elasto-plastic material model calibrated in the previous section. Only those stress state traces identified as possible points of fracture initiation are used, these traces are referred to as the fracture candidates. They are a function of the true equivalent plastic strain. With the fracture displacement known from the experimental results, the fracture time is found in the simulation results and that in turn gives the fracture strain of a trace. Of each set of traces, the traces which accumulate the most damage are used for the optimization. This optimization routine will calibrate the height of the mMC fracture surface. Here,  $k_S$  and  $n_S$  are fixed and the parameters  $c_{1-4}$  are optimized such that the damage accumulated along a trace reaches the critical value  $D = 1$  when the trace reaches the fracture strain. This is the objective function. In the mMC fracture surface optimization for the Tribond core layer, the objective function for the four standard tests will be  $D = 1$  and for the fifth test, the BE20 test, it is  $D \leq 1$ . This is because the BE20 test is meant to specify a lower bound to the mMC fracture surface.

The optimized parameters of the mMC fracture surface for a 0.1 mm mesh are shown in Table 4.8. The fracture surface is shown in Figure 4.14. During the optimization, it was found that there was a competition between the damage values of the NT and BE20 tests. Figure 4.14 shows that their stress state traces lie close together and appear to influence the mMC fracture surface adversely. This happens when the NT traces shift the mMC fracture surface down while the BE20 traces try to shift it up locally. The balance to which the damages were optimized had to be shifted slightly to ensure fracture would not occur too soon in the core layer of the BE20 test. Therefore, the average fracture displacement of the BE20 test, with which the fracture strains of the traces were determined, was adjusted to 13.3 mm from 12.63 mm, see Table 4.7.

The behavior of the calibrated core layer fracture model is checked against the core-only specimen results. The results are shown in Figure 4.15. The UT simulation fracture results are inaccurate due to specimen necking being simulated too late which is a consequence of the plasticity optimization. The NT simulation results are very accurate, the fracture results show the marginal effect of the mMC fracture surface being shifted up locally by the BE20 traces. However, the delay in fracture is very small. Validating the fracture model with the full-Tribond experimental results is only possible after the surface layer fracture model and a mixing rule are calibrated.

### 4.3.3 Surface layer

To calibrate the surface layer fracture model and the mixing rule for the transition zone fracture behavior, transition zone fracture results are required. The only experiment which showed fracture somewhere else than the core was the BE20 test. In Section 3.2.6, the fracture behavior of the BE20 test was investigated. Figure 3.13 shows a micrograph of a specimen with a crack in the center of its cross section. It would seem that fracture does not initiate in the outer fiber of the specimen. However, an exact hardness layer in which fracture initiates cannot be pinpointed. With only one load case in which fracture initiates, the mMC fracture surface cannot be calibrated in the same way as the core layer fracture model. Considering the surface layer is more ductile than the core layer, fracture in this layer is mostly a secondary effect. However, it cannot be neglected, as a surface layer fracture model is still required to ensure elements are eliminated. A different approach to calibrate the surface layer fracture model must be found.

Based on the fracture results of the BE20 test, the surface layer fracture model should at least avoid fracture in the outer bending fiber of a Tribond specimen. In the case of a 0.1 mm mesh, the outer bending fiber are the elements with hardness value  $HV = 193 HV0.5$ . Fracture is avoided if the damage values of

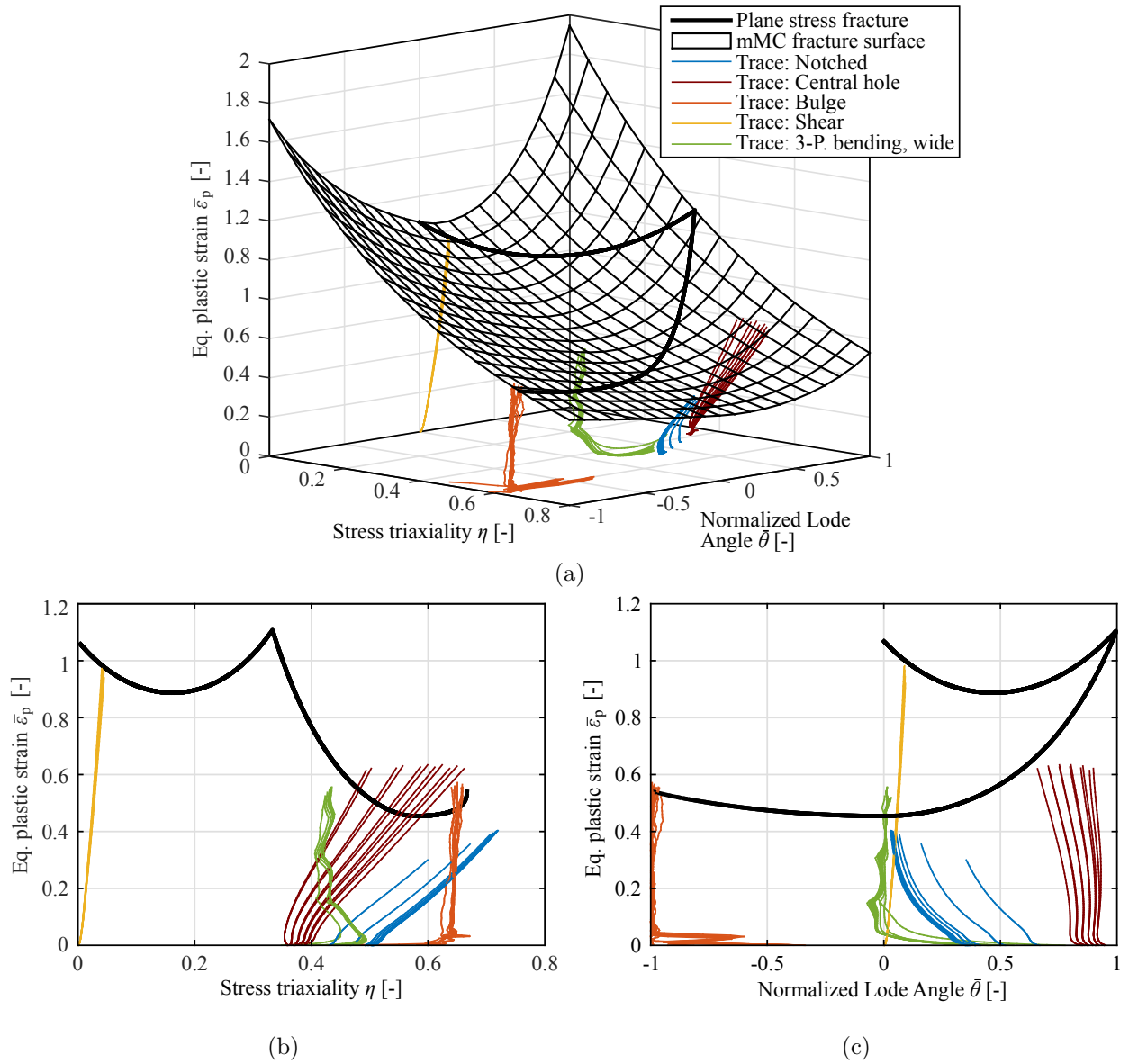


**Figure 4.14** Calibrated core layer mMC fracture surface for a 0.1 mm mesh (a) and the plane stress fracture curve in the  $(\eta, \bar{\epsilon}_p)$ -plane (b) and the  $(\bar{\theta}, \bar{\epsilon}_p)$ -plane (c). With stress state traces of the fracture candidates.

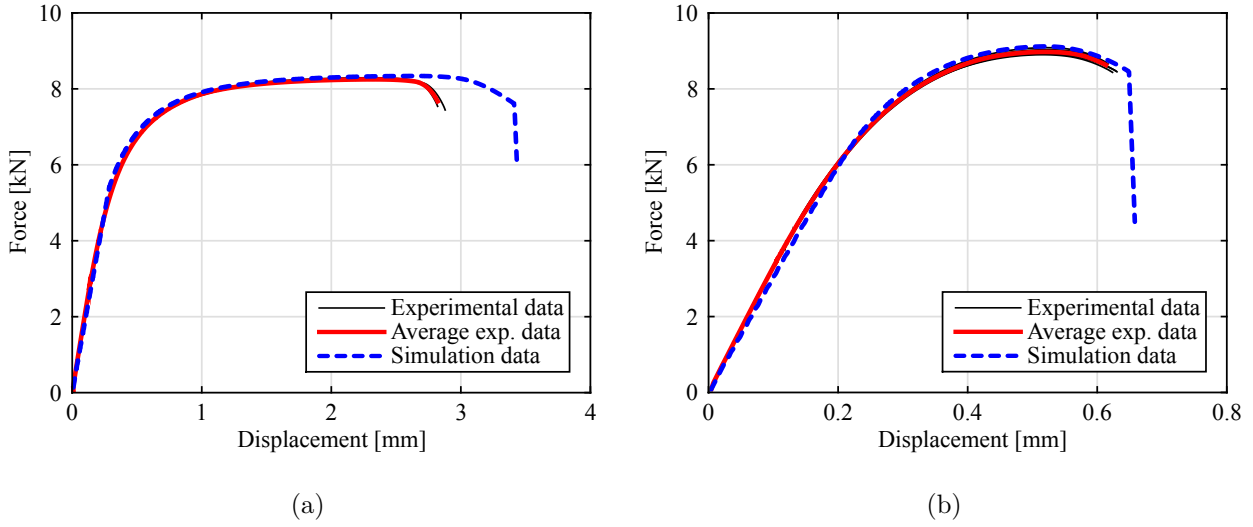


**Figure 4.15** Core layer fracture model optimization and core-only experimental results: uni-axial (a) and notched tensile test results (b).

the stress state traces are less than one. To calculate the damage accumulation, the mMC fracture surface in the transition zone needs to be known. The transition zone fracture model is described as:

$$\bar{\epsilon}_{f,tz} = f_{core} \cdot \bar{\epsilon}_{f,core} + (1 - f_{core}) \cdot \bar{\epsilon}_{f,surface} \quad (4.8)$$

where the core layer fracture model  $\bar{\epsilon}_{f,core}$  was calibrated in the previous section and the unknowns are the core layer fraction  $f_{core}$  and the fracture model of the surface layer  $\bar{\epsilon}_{f,surface}$ .

The core layer fraction  $f_{core}$  is specified by a mixing rule. Initially, the same linear mixing rule is used as for the plastic behavior, see Equation 4.2. The surface layer fracture model  $\bar{\epsilon}_{f,surface}$  is unknown, but the stress state traces  $\bar{\epsilon}_f(\eta, \theta)$  for the outer bending fiber elements are known from the BE20 simulation. These are the traces of transition zone elements at  $HV = 193$  with both core and surface layer fracture models defining its point of fracture. From these traces a lower bound fracture strain  $\bar{\epsilon}_{f,max}$  can be determined, using the average experimental fracture displacement  $d_{frac}$  specified in Table 4.7. In the case of proportional loading (constant stress state), the stress state trace of the maximum fracture strain  $\bar{\epsilon}_{f,max}$  is equal to the fracture strain of the transition zone fracture model  $\bar{\epsilon}_{f,tz}$  at a specific hardness and stress state. The stress state traces of the outer bending fiber element  $HV = 193$  in Figures E.1 and E.2, do indeed show relatively constant stress states. Therefore, to avoid fracture in the outer bending fiber, the approximate lower bound of the transition zone fracture model at a specific stress state and  $HV = 193$ , is specified by:  $\bar{\epsilon}_{f,tz} \geq \bar{\epsilon}_{f,max}$ . The only unknown in Equation 4.8 is the surface layer fracture model  $\bar{\epsilon}_{f,surface}$  at this stress state.

Solving would only give the fracture strain of a single stress state, no fracture surface can be fit to this. However, the experimental fracture results seem to suggest that the BE20 test is the only loading case, and specifically stress state, where the surface layer fracture model critically influences the fracture behavior. Therefore, the fracture behavior at different stress states need only be roughly approximated, as it is a secondary effect. The surface layer fracture model  $\bar{\epsilon}_{f,surface}$  is approximated with the same shape fracture model as is used for the core layer  $\bar{\epsilon}_{f,core}$ , only shifted so as to assure fracture does not occur too soon in the BE20 test. The height of the surface layer fracture model is specified by the fracture results of the BE20 test in the outer bending fiber. For this, the calculation method described above will be used, only instead of specifying the surface layer fracture model at the specific stress state, the shift of the core layer fracture model to the surface layer fracture model will be calculated. The shift is defined as:

$$\Delta\bar{\epsilon}_f = \bar{\epsilon}_{f,surface} - \bar{\epsilon}_{f,core} \quad (4.9)$$

The above method is applied to calibrate an initial surface layer fracture model. The first step is to calculate the shift from the outer bending fiber elements of a 0.1 mm BE20 simulation. Figure 4.16 shows the unknowns and known values when calculating the shift. Equations 4.8 and 4.9 are combined to:

$$\Delta\bar{\epsilon}_f = \frac{\bar{\epsilon}_{f,tz} - f_{core} \cdot \bar{\epsilon}_{f,core}}{1 - f_{core}} - \bar{\epsilon}_{f,core} \quad (4.10)$$

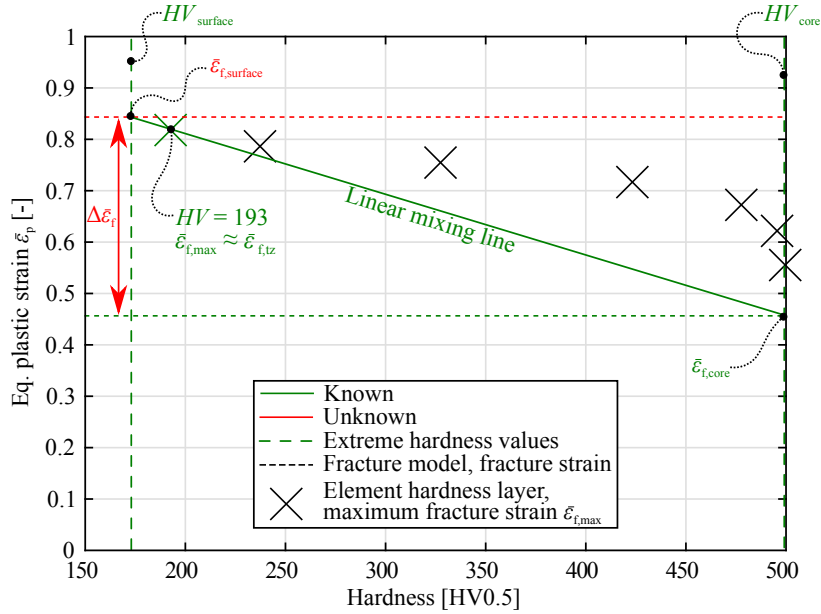


**Figure 4.16** Illustration of the calculation method for the fracture model shift, using the outer bending fiber elements of the wide specimen 3-point bending test simulation.

**Table 4.9** Calibrated parameters of the surface layer mMC fracture model for a linear mixing rule and a 0.1 mm mesh.

	$k_S$ [GPa]	$n_S$ [-]	$c_1$ [-]	$c_2$ [GPa]	$c_3$ [-]	$c_4$ [-]
Surface layer	2.371	0.08954	0.0499	1.2936	0.9133	1.0421

in which the core layer fraction  $f_{\text{core}}$  is given by the linear mixing rule of Equation 4.2. With the hardness values known, the core layer fraction can be calculated for hardness layer  $HV = 193$  in the transition zone fracture model. The cross at  $HV = 193$ , in Figure 4.16, marks the maximum fracture strain  $\bar{\epsilon}_{f,\text{max}}$  of the set of traces identified for fracture initiation in this hardness layer. It approximates the transition zone fracture model strain  $\bar{\epsilon}_{f,tz} \approx \bar{\epsilon}_{f,\text{max}}$ , assuming proportional loading. The core layer fracture model  $\bar{\epsilon}_{f,\text{core}}$  is evaluated at the stress state  $(\eta_{\text{ep}}, \theta_{\text{ep}})$  of the trace's maximum fracture strain  $\bar{\epsilon}_{f,\text{max}}$ , where ep stands for the end point. Now the unknown surface layer fracture model  $\bar{\epsilon}_{f,\text{surface}}$  can be calculated for the same stress state. The only remaining unknown is the shift  $\Delta\bar{\epsilon}_f$  which can no be calculated from Equation 4.9, this gives  $\Delta\bar{\epsilon}_f = 0.3869$  [-].

The surface layer fracture strains  $\bar{\epsilon}_{f,\text{surface}}(\eta, \theta)$  are calculated by shifting the core layer fracture model  $\bar{\epsilon}_{f,\text{core}}$  for all stress states by  $\Delta\bar{\epsilon}_f = 0.3869$  [-]. Now, the surface layer fracture model parameters of Equation 2.11 can be calibrated by fitting them to the shifted model. Of these six parameters the  $k_S$  and  $n_S$  are left constant and taken from the core layer fracture model. According to Bai [7],  $k_S$  affects the height of the fracture locus, but its behavior is opposite to that of parameter  $c_2$ . This is easily observed to be true, as they could be combined into one new parameter instead of the fraction in Equation 2.11. Instead of a new parameter or one redundant variable,  $k_S$  is left constant. The power exponent  $n_S$  also influences the height, but it will also alter the lode angle dependence which is undesirable. Therefore, only the four parameters  $c_{1-4}$  are used for fitting. The six fracture model parameters are shown in Table 4.9.

Now, that the Tribond fracture model is completely defined with core and surface layer fracture models and a linear mixing rule, simulations can be performed to validate the made assumptions. The NT, CH, BT, SH, BE1.5, BE20, BB1.5 and BB20 are simulated. The simulation results are not shown completely, but will be briefly discussed here. In line with the fracture results of Figure 4.15, where core-only specimens were used to validate the core layer fracture model, it would appear that fracture occurs on time for NT, CH, BT and the SH tests. The simulation results of the BE and BB tests initially showed undesirable force levels at high displacements. In these four tests, the force is overestimated due to use of the uniform reduced integration (URI) method, to ensure hourglass prevention it adds artificial stiffness at high displacements. To

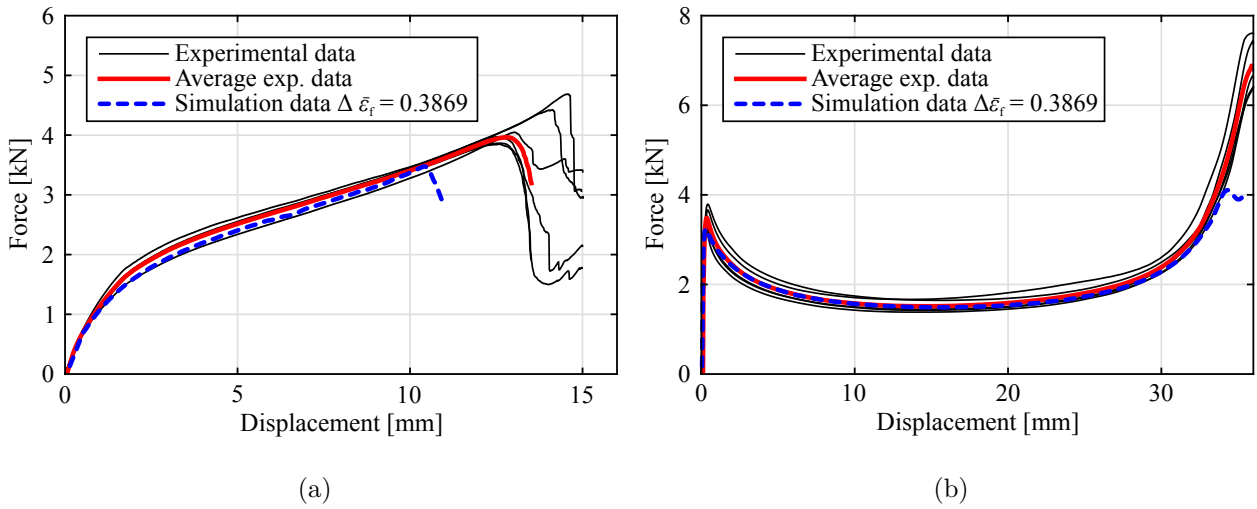


**Figure 4.17** Simulation results with calibrated surface layer fracture model and linear mixing approach: wide specimen 3-point bending (BE20) (a) and wide specimen buckling bending (BB20) test results (b).

**Table 4.10** Mean values and the standard deviations of the stress state traces at the end points.

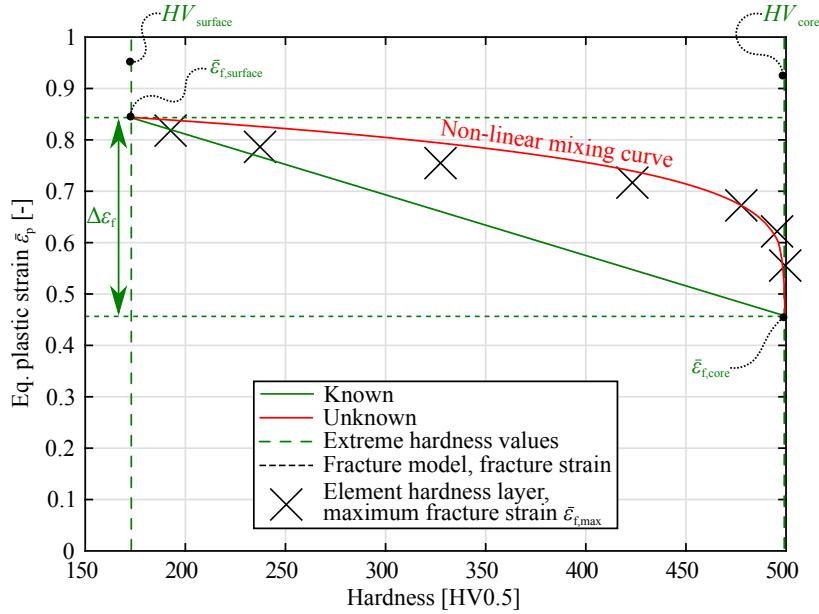
	$\eta_{ep}$	$\bar{\theta}_{ep}$	$\bar{\epsilon}_{f,max}$
Mean	0.5163	0.0156	0.4949
SD	0.04761	0.0014	0.0347

remedy this, the selective reduced integration (SRI) method was used for simulation of these two test types. The SRI method has eight integration points for the deviatoric strain part and one integration point for the volumetric strain part. It is four times more expensive than the URI method, but with the advantage that it does not need the artificial stiffness method for hourglass prevention. After new simulations with SRI for BE and BB tests, the BE20 and BB20 tests showed good force levels at large displacements, but undesirable fracture results, see Figure 4.17. It shows the BE20 simulation fractures too soon and the BB20 fractures, even though no fracture was expected. Here, the experiments without fracture (BE1.5, BB1.5 and BB20) prove themselves to be good lower bounds when validating the fracture model. In the BE20 test simulation results, presented in Figure 4.17a, the hardness layer  $HV = 478$  fractures first. This is also suggested in Figure E.3, which shows the plane stress fracture curves of all hardness layers and the stress state traces of these hardness layers plotted for the linear mixing rule. Figure 4.16 marks the maximum fracture strain of the set of traces identified for fracture initiation in all hardness layers. It shows that the linear mixing line, calibrated for the outer fiber, under cuts all damage values, except the maximum fracture strain it was calibrated for. When assuming proportional loading, they should all lie on or below the linear mixing line to avoid fracturing too soon. When they lie above the linear mixing line, it means the damage value has reached  $D > 1$  in the simulation, which would have eliminated the element before fracture occurred in the experiments. The maximum fracture strains of the traces per hardness layer do not have the same stress states ( $\eta_{ep}, \bar{\theta}_{ep}$ ), as can be seen in Figures E.1 and E.2. Comparing them with the maximum fracture strains of the linear mixing rule calibrated for  $HV = 193$ , therefore introduces an error. Table 4.10 list the mean values and standard deviations of the end point stress states and fracture strains of all hardness layers. This shows the error is relatively small.

Considering Figure 4.16, to get a linear mixing rule to work, all crosses (representing end points of traces) must lie on or under the linear mixing line. Therefore, the shifts are calculated for all of the hardness layers, see Table 4.11. The shift values show the height with which the surface fracture model needs to be shifted to avoid fracture occurring too soon in a specific hardness layer. The maximum value in this table would postpone element elimination in the simulation to the same point as the experimental results. The extreme shift suggested for hardness layer  $HV = 495$  shows that, with a linear mix, the surface layer fracture strain needs to be very high to assure fracture initiation does not occur too soon. However, simulation results

**Table 4.11** Calculated shifts for all hardness layers in the transition zone.

Hardness layer, $HV$ [HV0.5]	193	237	327	423	478	495
Shift, $\Delta\bar{\varepsilon}_f$ [-]	0.3869	0.3952	0.5290	0.9935	2.6175	7.7043

**Figure 4.18** Illustration of the calibration method for the non-linear mixing rule curve, using the maximum fracture strain of the stress state traces of the wide specimen 3-point bending (BE20) test simulation.

for the surface layer fracture model with a shift of  $\Delta\varepsilon_f = 7.704$  [-] showed that this shift was unrealistic, because under in-plane loading the surface elements are eliminated far too late. The out-of-plane bending test BE20 also showed undesirable behavior: although fracture initiated correctly within the material, the outer layer would not eliminate at all. These results are not shown here.

The extremely high shift required in a linear mixing rule, is because there is only a small fraction of surface layer fracture model mixed into the transition zone fracture model at  $HV = 495$ . An alternative to shifting the surface layer fracture model too high, is changing the linear mixing rule to a non-linear mixing rule. A non-linear mixing rule could account for the apparent high increase in fracture strain in the transition zone at only a small hardness drop. The proposed mixing parameter is similar to Equation 4.2, only now the parameter is non-linearly related to the hardness. The non-linear mixing parameter is:

$$f_{\text{core, nl}} = f_{\text{core}}^b = \left( \frac{HV - HV_{\text{surface}}}{HV_{\text{core}} - HV_{\text{surface}}} \right)^b \quad (4.11)$$

here  $f_{\text{core, nl}}$  is the non-linear core layer fraction and  $b$  is the exponent.

An illustrative non-linear mixing rule is plotted in Figure 4.18. Here, the maximum fracture strains  $\bar{\varepsilon}_{f, \text{max}}$  from the different hardness layers are plotted over the hardness just as in Figure 4.16. The exact non-linear exponent cannot be determined from the figure, it does however show the inevitable effect of fitting all maximum fracture strains of the hardness layers, namely that fracture will occur more or less simultaneously in all hardness layers. The exponent of the non-linear mixing rule is calibrated in an optimization routine which considers the damage accumulation more accurately, not assuming proportional loading or comparing the fracture strains at an average stress state, as in Figures 4.16 and 4.18.

The optimization routine will need to specify the shape of the non-linear mixing curve. The two variables in this curve are the exponent  $b$  and the fracture model shift  $\Delta\bar{\varepsilon}_f$ . With the relatively small distance between the fracture models for the surface layer hardness  $HV = 173$  and the transition zone  $HV = 193$ , the shift calculated for the linear mixing rule is used as approximation for the shift of the non-linear mixing rule. That means the shift is  $\Delta\bar{\varepsilon}_f = 0.3869$  [-] and the same surface layer fracture model parameters can be used, see Table 4.9. The only unknown parameter in the optimization is the non-linear exponent  $b$ . The objective function of this optimization routine considers the damage values of the individual hardness layers. Each

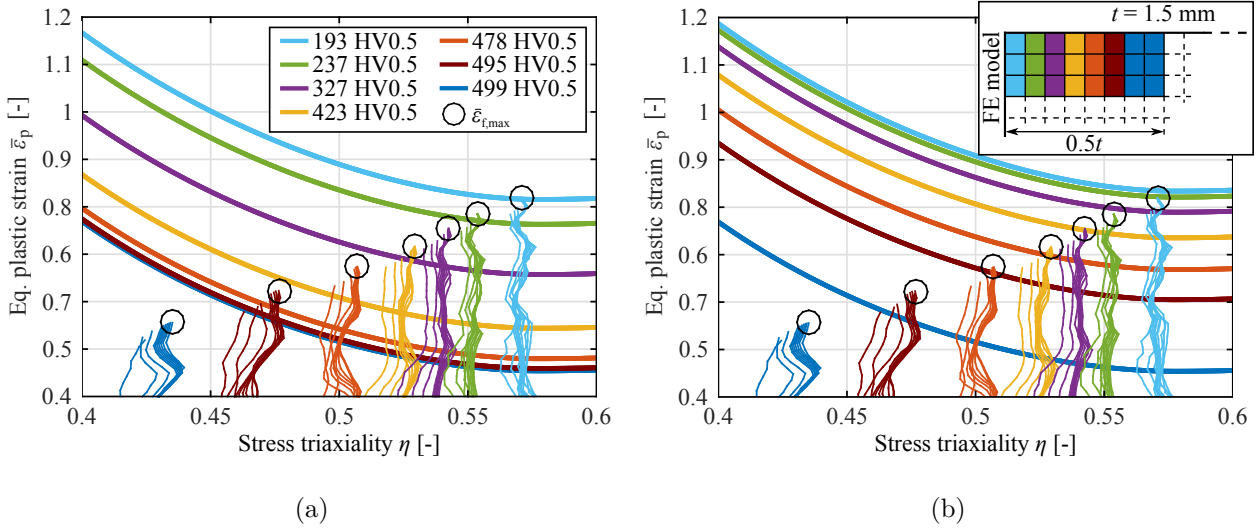


**Figure 4.19** Comparison of the linear (a) and non-linear (b) mixing rules: plane stress fracture curves for all hardness layers of a 0.1 mm mesh with the stress state traces in the  $(\eta, \bar{\epsilon}_p)$ -plane.

hardness layers damage was specified to be equal to the critical damage value  $D = 1$ . This gave a non-linear exponent of  $b = 0.21577$ .

The two different mixing rules are compared in Figure 4.19. This shows a closeup of the plane stress fracture curves of the transition zone fracture models of all hardness layers for the linear and non-linear mixing rule. The complete figures of the linear and non-linear mixing rule are shown in Figures E.4 and E.3, respectively. This clearly shows that at hardness layer  $HV = 495$  the plane stress fracture curve lies under the maximum fracture strain when a linear mixing rule is used and above the maximum fracture strain when a non-linear mixing rule is used. This means that the transition zone fracture model experiences too little influence of the surface layer.

With the new Tribond fracture model defined, simulations of all calibration tests are performed. The results are shown in Appendix F. The results are generally very good, not only showing fracture behavior similar to the experiments, but also simulating the correct force levels for elastic and plastic deformation. Considering the fracture results of the BE20 test, fracture still occurs slightly too early. This is caused by the inability of the fracture surface to accurately predict both the BE20 and NT tests fracture displacements. A compromise had to be made between overestimating the fracture displacement in the NT test and underestimating the fracture displacement in the BE20 test. This was done by using the increased fracture displacement of 13.3 mm instead of the average fracture displacement of 12.63 mm, see Table 4.7. The UT test shows the largest difference in fracture displacement. This test also shows less accurate elasto-plastic behavior, by underestimating the force response. In the case of the UT test, the occurrence of weak spots in the experimental results are considered the major reason for these deviations. Therefore, they cannot be used to validate the fracture behavior. For the SH and BT tests, fracture seems to occur too soon, but it is important to compare these values with the average fracture displacements of Table 4.7 and not with the average curves. These tests then fracture exactly as expected. The average curves served to calibrate the elasto-plastic behavior. This shows the elasto-plastic behavior is very accurately predicted by the calibration of Section 4.2.

According to the calibrated fracture model, the fracture properties are non-linearly related to the hardness properties unlike the elastic and plastic properties which are linearly related. Simulation results for fracture models with a linear hardness-driven mixing rule were unable to accurately predict the fracture in out-of-plane bending tests. This is because fracture is a more local effect, meaning it is also influenced by material defects. The norm ISO 18265 describes the linear conversion of hardness values to tensile strength, but no such norms are available for hardness values and fracture properties.

#### 4.3.4 Mesh size dependency

The Tribond fracture model has been calibrated for a 0.1 mm mesh, with good results. However, the industry standard for vehicle crash simulations normally consider coarser meshes, e.g. 0.2 mm and 0.5 mm. Eller [12] showed that the predicted strain fields are mesh size dependent, because a coarse mesh cannot accurately

**Table 4.12** *Hardness values of a solid element model with a 0.2 mm and a 0.5 mm mesh through the thickness.*

Element designation	1	2	3	4
0.2 mm mesh, $HV$ =Hardness [HV0.5]	212.274	378.462	489.302	499.401
0.5 mm mesh, $HV$ =Hardness [HV0.5]	276.639	498.153	–	–

display strain gradients or the geometric deformation in a model. This adversely influences the strain-based fracture model. To accurately model the fracture behavior of the coarser meshes, the fracture models have to be recalibrated. No finer meshes are considered, because the height of the fracture model can be considered to have converged for a 0.1 mm mesh, as it can accurately predict the strain fields. In the case of Tribond, there is an additional mesh size dependency, namely the accurate mapping of the hardness through the thickness of a specimen. Figures 4.20 shows the hardness map in the coarser meshes of 0.2 mm and 0.5 mm. Table 4.12 shows the exact hardness values through the thickness of a 1.5 mm thick FEM model.

The calibrations were performed in the same way as for the 0.1 mm mesh. First, a core layer fracture model was calibrated from the NT, CH, BT, SH and BE20 test results. For the 0.2 mm and 0.5 mm mesh, the core layer mMC fracture surfaces are shown in Appendix G. A significant consequence of the limited amount of elements through the thickness of a 0.5 mm mesh is that the four elements are all transition zone elements. This is because the core elements do not actually have the pure core layer hardness of  $HV = 499$ . Therefore, when calibrating the core layer fracture model, the traces of the transition zone elements  $HV = 498$  were used, hereby disregarding the small amount of surface layer mixed in at this hardness value. Next, a shift was calculated, which avoids fracture in the outer bending fiber elements of the BE20 tests, based on a linear mix. The surface layer fracture model parameters were fitted to the shifted model. Now, the same exponent of the non-linear mixing rule as in a 0.1 mm mesh is used, as the mixing rule is material dependent, not mesh size dependent. However, the exponents were calculated for the other mesh sizes. The 0.2 mm mesh gave an exponent of  $b_{0.2} = 0.3429$  and the 0.5 mm mesh an exponent of  $b_{0.5} = 1$ , which reduces the mixing rule to a linear mixing rule. Both these exponents did not equal the  $b_{0.1} = 0.2158$  calibrated in the 0.1 mm mesh. This is mainly due to there not being enough data points. For the 0.2 mm mesh a hardness value very close to the core layer hardness might give an exponent closer to  $b_{0.1}$  and for the 0.5 mm mesh only two data points need to be fitted, which can be done with a straight line. The fracture model calibration results are listed in Table 4.13.

The simulation results are shown in Appendix F, alongside the results of the 0.1 mm mesh size results. The results are accurate, with good prediction of the forces, even for the 0.5 mm mesh with its limited four elements through the thickness. The fracture displacements are accurately predicted for the in-plane loading cases. However, for the out-of-plane bending wide specimen results, the 0.5 mm mesh did not accurately predict fracture. In both the BE20 and BB20 tests, fracture occurred too soon. The 0.5 mm mesh fracture model underestimates the fracture displacement in a BE20 test by a little more than 20%. However, the BB20 test lower bound fracture displacement is underestimated by less than 3%. The difference in the force level for the plastic deformation in a SH test seems to be due to the Hershey exponent  $a$  being too high. Although, this is contradicted by the correctly predicted force levels in the NT tests. Considering the properties of a Hershey yield criterion, both the shear and plane strain tension stress states are equally dependent on the uni-axial tension yield stress and the Hershey exponent. One cannot be changed without the other also changing. The 0.5 mm mesh predictions for the SH test do seem accurate, but this is the result of two errors counteracting each other and thereby giving a seemingly accurate fit. Besides the Hershey effect, the second error source is the inaccurate SH test model geometry, specifically the surface grooves cannot be accurately represented in the coarse 0.5 mm mesh. Concerning the tests which do not show fracture (BE1.5, BB1.5 and BB20), the fracture model might overestimate the fracture behavior in the non-fracturing tests. To see if this is the case, the next step is to validate the calibrated material model.

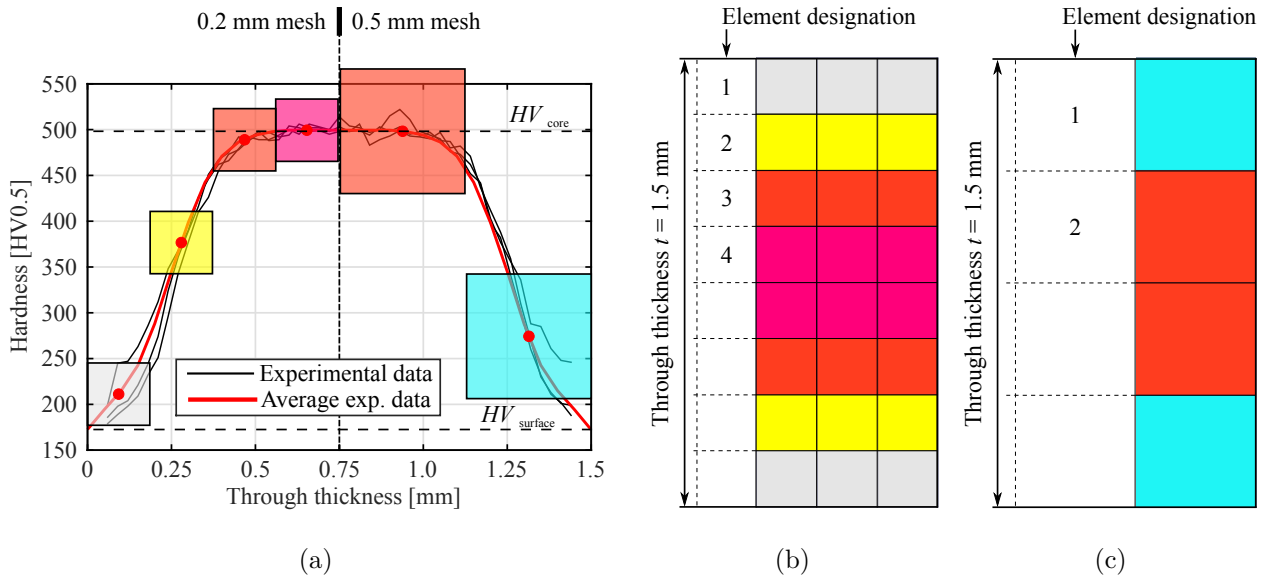


**Figure 4.20** Hardness map of the experimental data with 0.2 mm and 0.5 mm mesh (a) and a 0.2 mm (b) and 0.5 mm mesh FEM model cross section (c).

**Table 4.13** Calibrated parameters of the core and surface layer mMC fracture model, with a non-linear mixing rule for a 0.2 mm and a 0.5 mm mesh size.

	Fracture model	Core layer	Surface layer	Transition zone
0.2 mm mesh	$k_S$ [GPa]	2.3709	2.3708	—
	$n_S$ [—]	0.0895	0.0896	—
	$c_1$ [—]	0.0970	0.0524	—
	$c_2$ [GPa]	1.3136	1.3028	—
	$c_3$ [—]	0.9601	0.9201	—
	$c_4$ [—]	1.0613	1.0323	—
	$b$	—	—	0.2158
0.5 mm mesh	$k_S$ [GPa]	2.3709	2.3709	—
	$n_S$ [—]	0.0895	0.0896	—
	$c_1$ [—]	0.0972	0.0551	—
	$c_2$ [GPa]	1.2378	1.2450	—
	$c_3$ [—]	0.9292	0.9034	—
	$c_4$ [—]	0.9969	0.9922	—
	$b$	—	—	0.2158

# Chapter 5

## Model validation

In this chapter, the hardness-driven Tribond material model is validated, by using tests which were not used to calibrate the material model. Validation tests often consider more complex geometries instead of the purely in- or out-of-plane loading cases used for calibration. To validate the Tribond material model, the more complex geometry of an L-section compression test as presented by Henn [18] is used.

### 5.1 Experimental work

L-Section compression tests were performed with 15 full-Tribond specimens. The L-section specimen cross section is shown in Figure C.7. The test setup is shown in Figure 5.1a. The specimen length is  $l = 120$  mm with a free length between the clamps of 80 mm.

A specimen was mounted between the upper and lower clamps and fastened with a total of twenty bolts, ten in each clamp. First, the two smaller bolts were securely tightened with a hex key, clamping the specimen. Then the eight large bolts were securely tightened with a wrench, to fasten the clamping parts to the base plate. The clamping parts are shown in Figure 5.1b. A set of guide bolts were used to force the long side of the L-section to buckle inwards. The engaging mechanism in Figure 5.1 is folded down, when engaged it presses with both bolts on the visible side of the specimen. The tests were performed with a 600 kN Zwick universal material testing machine, at a cross-head speed of  $0.5 \text{ mm s}^{-1}$ . The measured force–displacement curves are shown in Figure 5.2. The tests showed no fracture and were stopped in most cases at a displacement of  $d = 32$  mm, exceptions were made to investigate self-contact. No DIC camera setup was used, but images of the deformation modes were made with a digital camera, see Figure 5.3. The two main different deformation modes are the outward buckling of the short side or of the long side of the L-section specimen. The figures also show the fold compressing to the point of self-contact, which causes the force to increase in some tests after a displacement of approximately 26 mm. The asymmetrical folding witnessed in some specimens is shown in Figure 5.3b. None of the tests showed any signs of fracture in the bends or folds of the free length. Shear fracture was observed directly at the clamp in some specimens, see Figure 5.7.

The first six tests were performed with the guide bolts engaged. This ensured that the long side would buckle inwards, see Figure 5.3a. The other nine tests were performed without the guiding bolts. Now, only one specimen bend inwards, showing a preference for the long side to buckle outwards. This preference could be caused by imperfections in the test setup and specimens. The different deformation modes showed no difference in force level. This is visible in the force–displacement curves of Figure 5.2 which shows the experimental data of both deformation modes.

### 5.2 Simulation results

To validate the hardness-driven material model, the L-section compression test is modeled. The Tribond fracture model was calibrated for three different mesh sizes. To simulate a compression test for each, three different FE models are needed with solid element mesh sizes of 0.1 mm, 0.2 mm and 0.5 mm.

Simulating the compression test of an L-section specimen is costly in terms of computation time. Especially, with its relatively large volume and a 0.1 mm mesh. Standard methods to reduce the amount of elements in an FE model are using a coarse mesh with local mesh refinement and creating an improved

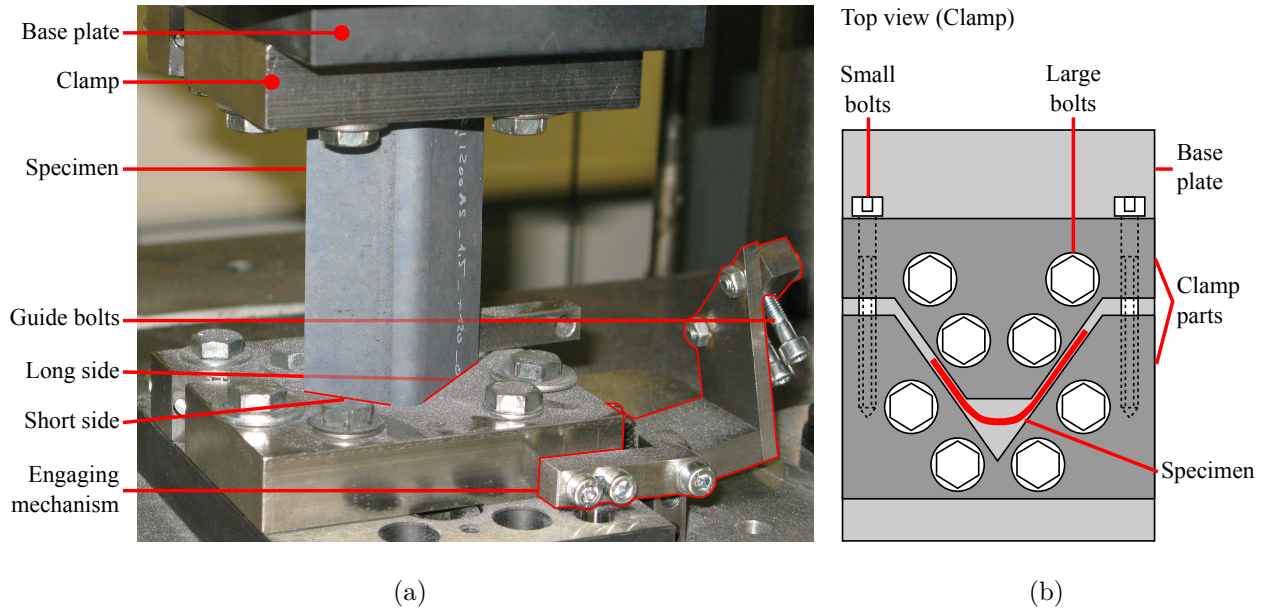


**Figure 5.1** Test setup (a) and a schematic of one of the clamps of the L-section compression test (b).

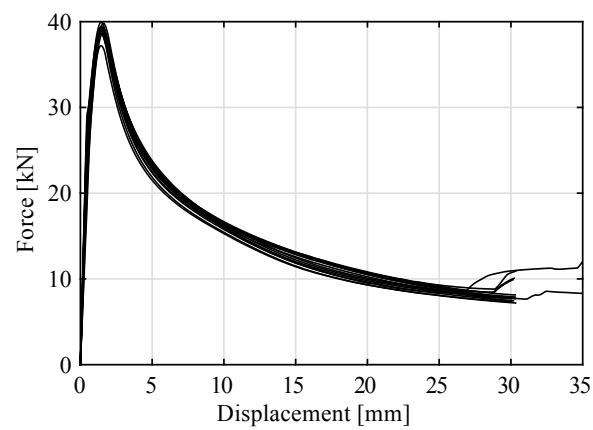


**Figure 5.2** Measured force-displacement curves of the L-section compression test.

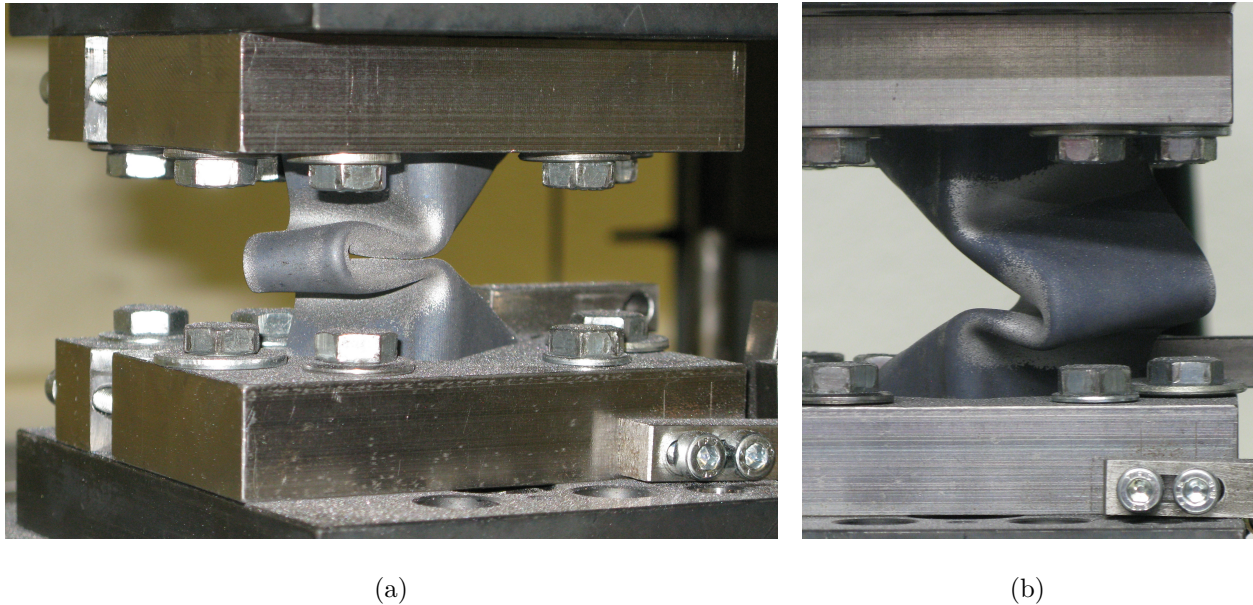


**Figure 5.3** *Different deformation modes of the L-section specimens after a compression test: with self-contact and inward long side buckling (a) and asymmetrical folding and outward long side buckling (b).*

equivalent simulation model. With the hardness mapping through the thickness and the complex deformation of the specimen, local mesh refinement could not be applied. This meant the complete FE model needed to be meshed with an 0.1 mm mesh size. An improved equivalent simulation model could be created by only modeling half of a specimen, by using the specimen's only symmetry line. Creating such a symmetrical model would however exclude asymmetrical folding from occurring, a phenomenon witnessed in many of the experiments. It would also require a boundary condition to model self-contact as this would not occur in a half specimen. An alternative improved equivalent simulation model was created for the specimen's gauge length. Only modeling the free length of the specimen, with a boundary condition replacing the clamps and 20 mm of the clamped specimen's top and bottom. The clamping boundary condition in this model proved too stiff, so the complete specimen and clamp were modeled instead. The final model with a 0.2 mm mesh, is shown in Figure 5.4. Similar models were created for the 0.1 mm and 0.5 mm mesh sizes. In the model, the clamps, base plates and guide bolts are modeled with shell elements. The clamp is modeled with a clamping force of 20 kN and a coefficient of friction of 0.2 between the clamp and the specimen. The base plates compress the specimen and the guide bolt is used to guide the direction of buckling. During testing, the guiding bolts press 1 mm into the specimen. Preliminary simulation results showed that without the guide bolts, there was a high buckling force required to initiate bending. This in contrast to the experimental results, which showed the guide bolts had no influence on the force–displacement curves. The difference between these results lies in the perfect model used in simulation versus the imperfect test setup. The expected behavior is a high force peak to cause sudden buckling of the material, but in the actual test, a specimen may be slightly bend or the base plates of the setup misaligned. Then, the buckling will occur more slowly, with a lower force peak. Therefore, the guide bolts were added to the simulation and the influence of the alignment of the top and bottom base plates was studied. To do this, FE models with a straight base plate and rotated base plate were tested. For the rotated base plate FE model the bottom base plate was rotated clockwise by  $1^\circ$  around the  $y$ -axis.

The simulation results of a straight and a rotated base plate are shown in Figure 5.5a. The simulation results are relatively close to the experimental results. The rotated base plate influences the height of the buckling force peak. The force levels after buckling are relatively constant between the straight and rotated base plate, but both the 0.2 mm and 0.5 mm mesh sizes shows the magnitude of the force levels are overestimated at large displacements. These simulations were performed with uniform reduced integration (URI), to reduce computation time, but this seems to have increased the stiffness. These simulations are repeated with selective reduced integration (SRI) to get more accurate results. The results are shown in Figure 5.5b. The results now more accurately predict the force levels at large displacements. The difference between the simulation results obtained with the straight and rotated base plate also becomes more apparent. Namely, that introducing some imperfection in the test setup alignment allows for better prediction of the

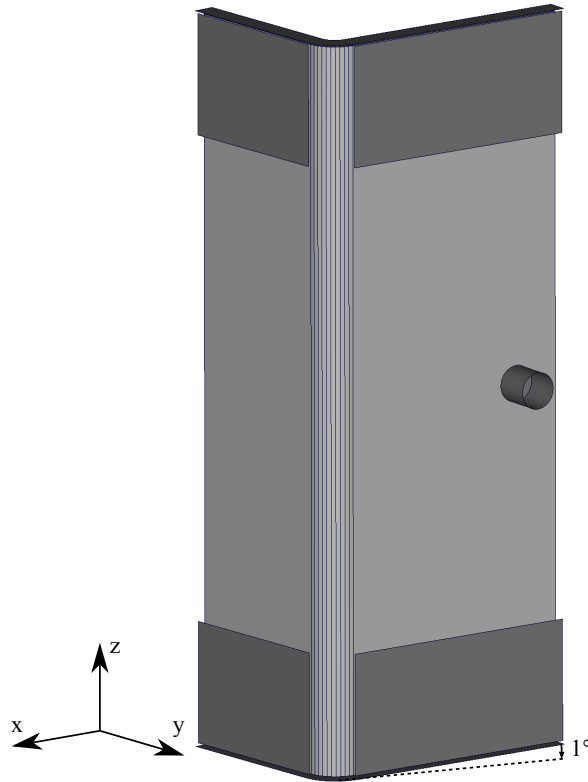


**Figure 5.4** *FE model of the L-section compression test.*

force levels of the experimental results. At the very end of the simulation results, the increase in the force shows the effects of self-contact. The difference in computation time between different integration types is shown in Table 5.1. The times are based on the normalized CPU usage for each simulation. Just as the experimental results, most of the simulations did not show fracture. Only the 0.5 mm rotated punch simulation showed fracture at the clamp. This is discussed further in the next section.

### 5.3 Comparison of the deformation modes and fracture

The simulation results validate the elasto–plastic force levels and the lower bound fracture behavior of the material model. To get better insight into the validity of the elasto–plastic model, the deformation modes are compared here. The 0.2 mm rotated base plate results are shown in Figure 5.6, more images of the 0.2 mm simulations are shown in Appendix H. The deformation modes fit well, with both the bending behavior of the straight and rotated base plate simulations corresponding to compressed specimens.

Unfortunately, the L-section compression test cannot serve to validate the fracture model in the case of a complex stress state. However, in some experiments, shear fracture occurred at the clamp, see Figure 5.7. The shear fracture only occurred in specimens whose long side buckled outwards. Shear fracture was also observed in the 0.5 mm mesh, with rotated base plate FE model. In this case, fracture occurred when the short side buckled outwards, see Figure 5.8. Fracture was only observed for a rotated base plate, it seemed to only occur in the case of asymmetric bending.

The material model is able to accurately predict the deformation modes and force levels witnessed in the L-section compression tests. The validation results show that fracture is not predicted too early. With the 0.5 mm mesh, fracture was predicted too early in the 3-point bending test. This validation shows that under crash-like complex bending, the model is not too conservative.

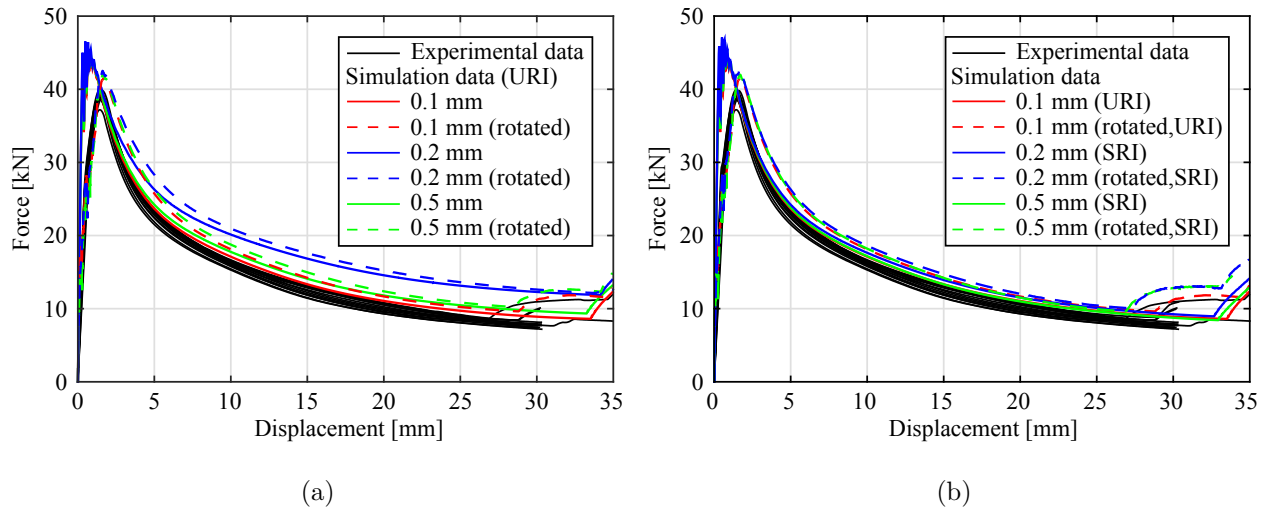


**Figure 5.5** *L-Section compression test validation results for different mesh sizes, illustrating the difference between a straight and rotated base plate with URI (a) and with SRI for the coarser mesh sizes (b).*

Mesh size	Rotated base plate	Integration method	Normalized computation time $\left[ \frac{\text{hours}}{128 \text{ CPU}} \right]$
0.1 mm	–	URI	218.3
0.1 mm	✓	URI	142.7
0.2 mm	–	URI	16.3
0.2 mm	–	SRI	78.5
0.2 mm	✓	URI	15.4
0.2 mm	✓	SRI	67.6
0.5 mm	–	URI	1.2
0.5 mm	–	SRI	3.1
0.5 mm	✓	URI	1.2
0.5 mm	✓	SRI	3.3

**Table 5.1** *Overview of the performed simulations.*

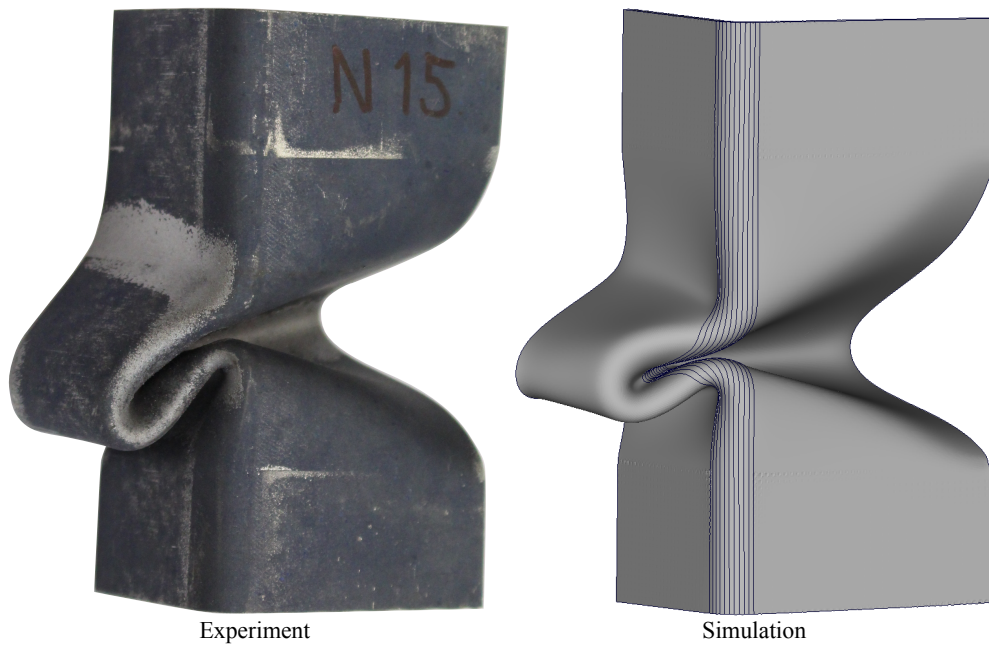


**Figure 5.6** *Front view: side-by-side comparison of the asymmetrically folded, compressed specimen and rotated base plate FE model with an 0.2 mm mesh and SRI.*

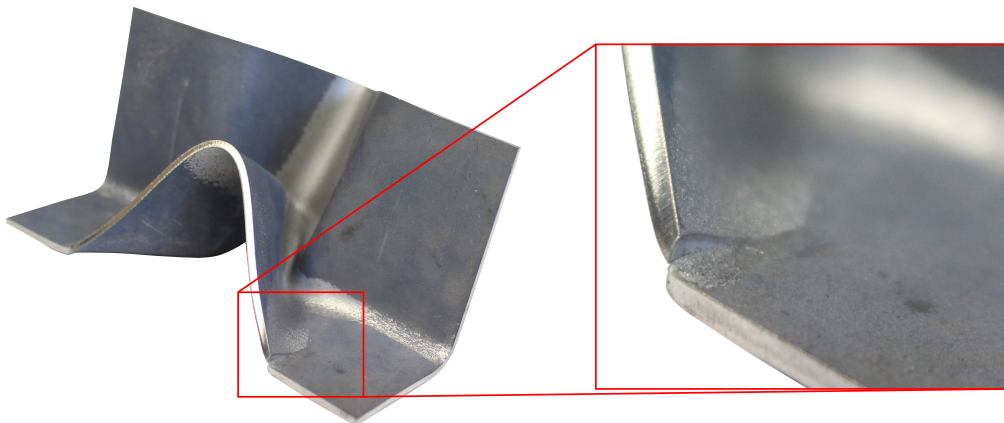


**Figure 5.7** *Compressed specimen with shear fracture above the clamped section.*



**Figure 5.8** *The 0.5 mm mesh with SRI and rotated base plate FE model with shear fracture above the clamped section.*

# Chapter 6

## Conclusion and recommendations

The objective of this master thesis was to calibrate a hardness-driven material model of the composite steel Tribond 1200 for use in crash simulations. The main focus was the detailed modeling of the material behavior with solid elements. It was stated, the model should accurately predict the elastic, plastic and fracture behavior for all hardness values through the thickness. The model must represent the material behavior in the case of complex loading experienced during a crash. The previous chapters described the work done towards reaching these goals. An overview of the main conclusions and recommendations for future work are both presented here.

### 6.1 Conclusion

This study set out to characterize and model the behavior of a composite steel. The characterization consisted of through thickness hardness measurements and mechanical testing of specific stress states. The characterized behavior was modeled with separate plasticity models for the core and surface layer hardness values and six fracture models for both extreme hardness values and mesh sizes of 0.1 mm, 0.2 mm and 0.5 mm. The properties of the interpolated hardness values were defined by a linear mixing rule for the plastic behavior and a non-linear mixing rule for the fracture behavior.

In Chapter 2, the manufacturing process and heat treatment of the Tribond sheets used in this study were described. Also the theoretical background of the material modeling process was presented. The following conclusion is drawn from Chapter 2:

- The hardness properties of the composite steel Tribond 1200 depend on the base steels and the size of the transition zone. The transition zone between these two steels in turn depends on the heat treatment, showing a clear increase in size after press hardening the Tribond sheet. This is caused by diffusion of alloying elements of the base steels at high austenitization temperatures in the furnace.

The Tribond characterization was performed in Chapter 3. It describes the experimental work done to study the properties through the thickness and the mechanical tests performed to understand Tribond's behavior under different load cases and stress states. The following conclusions are drawn from Chapter 3:

- The measured force displacement curves of the uni-axial tensile tests showed a large amount of scatter. The measured strain fields showed this was caused by the presence of weak spots in the tensile specimens. These weak spots negatively influence the force level, point of necking and the fracture displacement. A hardness measurement of the sheet cross section showed these weak spots corresponded to sections where less material reached the maximum hardness. Whether these problems occur during the rolling process or press hardening of Tribond sheets is unknown.
- The wide specimen results of the out-of-plane bending tests were investigated under a microscope. The fracture investigation of the 3-point bending test results showed fracture did not initiate in the outer bending fiber, as is common in monolithic steels. Instead the micrographs showed fracture initiated within the material. Further deformation after initial fracture showed delamination between the base steels to be a secondary fracture mode. The buckling bending test investigation showed no fracture for similar bending angles as the 3-point bending test under a similar stress state. This is due to the different bending radii during testing. In the case of a 3-point bending test, the knife will enforce

a sharp bend whereas in the buckling bending test a large area can deform. Therefore, the 3-point bending test accumulates more damage locally and thus fractures at a lower bending angle.

In Chapter 4, the material model was calibrated. The elastic, plastic and fracture properties for each hardness value through the thickness are defined by material models and hardness-driven mixing rules. The following conclusions are drawn from Chapter 4:

- The elastic and plastic behavior of the core layer model were calibrated with core-only specimens. Yielding is defined by an isotropic Hershey yield criterion with an exponent of  $a = 6$ . The hardening curve is defined by experimental results and a non-linear mix of fitted Swift and Voce hardening laws. The calibrated model shows good accuracy when modeling the core-only specimens used in the calibration. The elastic and plastic behavior of the surface layer model were calibrated with full-Tribond specimens. The surface layer hardening curve was determined in an inverse FEM optimization by calibrating a linear mix of the Swift and Voce hardening laws. A linear relationship between hardness and hardening properties was used to simulate full-Tribond specimens with good accuracy. The results were validated and show good accuracy in predicting the strain fields on the surface of notched tensile tests. As well as good predictions of the force–displacement curves in all mechanical tests. The in-plane loading results of uni-axial tensile and shear tests show slight deviations. However, the simulation results of the uni-axial tensile test lie within the scatter of all experimental results extracted in different rolling directions. The shear test results underestimate the force level slightly, which is caused by the Hershey exponent. With the coarser 0.2 mm and 0.5 mm meshes, the out-of-plane loading test results were initially overestimating the force level at high displacements. This was remedied by using a more expensive integration method without the artificial stiffness method for hourglass control, leading to excellent results.
- The fracture behavior of the core layer model was calibrated from the results of the in-plane loading tests and the wide specimen 3-point bending test for mesh sizes of 0.1 mm, 0.2 mm and 0.5 mm. The simulated stress state traces of these tests were used to calibrate the modified Mohr–Coulomb fracture surface. The result was validated by simulating the core-only specimen tests with a 0.1 mm mesh, which shows good results. The surface layer fracture model is a shifted version of the core layer fracture model, in which the shift was calculated with the fracture investigation results of the wide specimen 3-point bending test. To accurately simulate the fracture results for all mechanical tests a non-linear hardness-driven mixing rule had to be used. This rule was calibrated with the traces of the wide specimen 3-point bending test simulation results with a 0.1 mm mesh. After calibration, simulations were performed to validate the fracture model which showed good accuracy.
- The fracture properties are non-linearly related to the hardness properties, unlike the elastic and plastic properties, which are linearly related. A fracture model with a linear hardness-driven mixing rule was unable to accurately predict the fracture in out-of-plane bending tests. This is because fracture is a more local effect, meaning it is also influenced by material defects. The norm DIN 50150 contains tables linking the hardness values to tensile strength, but no such norms are available for hardness values and fracture properties. Together with the relationship found in this report between fracture and hardness, this does call into question the validity of using a hardness-driven modeling approach for fracture. Instead a different through thickness property might be used to drive the through thickness fracture properties, in which the link with fracture can be explained with a more physical description. However, the fracture predictions are very accurate with this non-linear hardness-driven mixing rule. Therefore, no other through thickness property-driven mixing rules were investigated.

In Chapter 5, the calibrated hardness-driven model was validated with an L-section compression test. The following conclusion is drawn from Chapter 5:

- To accurately simulate the L-section compression test, two different FE models were used with straight and rotated base plates. The simulation results show that the calibrated material model accurately predicted the force–displacement curves and lack of fracture in the bends and folds. The material model was also able to predict the occasional occurrence of shear fracture near the clamp. The plastic deformation modes were also accurately predicted.

## 6.2 Recommendations

Based on the work performed and presented in this thesis, the following recommendations are made for future work:

- The uni-axial tensile test results showed a large amount of scatter. It is recommended to investigate the influence of the heat treatment and rolling process on the through thickness properties. The heat treatment investigation should focus on whether the sheet was fully-quenched or heated. The rolling process investigation should focus on the presence of inclusions in the weld between the base steels and the uneven distribution of base steels through the thickness during rolling.
- To improve the hardening curve of the plasticity model at high strains, it could be considered to add the experimental results of the bulge test to the inverse FEM optimization, similar to Eller [11, 13]. The measured total strain curves of the bulge test should be added to the objective function. Computing bulge test simulations is still relatively expensive, because of the fine mesh required through the thickness. However, a quarter FE model was seen to suffice if attention was paid to concentricity of the punch, specimen and specimen clamp during testing.
- The hardness-based modeling approach should be validated. This could be done by trying to simulate experimental results of Tribond 1400. The material model would require the hardness curve of Tribond 1400 to simulate the experimental tests. Alternatively, some other composite steel might be used to validate the hardness-based modeling approach. This steel would have to have the same base steels as Tribond 1200. The results should show the validity of modeling composite steel sheets with differing distributions according to their through thickness hardness curve.
- With the eye on the future, an alternative calibration method for the material model might be tested. Similar to the ThyssenKrupp modeling method, material models could be calibrated for the base steels and then combined into a single material model for Tribond. This approach requires steel sheets of the base materials, which were not available for this work. This approach would lend itself for implementation in the parameter identification procedure (PIP), allowing the calibration of composite steels directly from a database of base steels. The model would then define transition zone properties based on a hardness curve measurement of the composite steel. This method is not necessarily better as it ignores testing the transition zone between welded base steels. However, this might be improved upon by using transition zone testing by removing for example the core layer.
- To investigate the pure shear stress state the shear tests as developed by Greve [16] was used. The gauge section of this test requires milling away the surface layer. An alternative shear test is the so called “smiley” shear test developed by Roth [28]. This test does not require changing the specimens thickness in the gauge section and would test the complete thickness of a full-Tribond specimen.

The hardness-driven material model for Tribond 1200 calibrated in this work focused on detailed modeling with solid elements. Before this material model can be used in crash simulations, some amendments need to be made. Ultimately, the finished model will be used by the Volkswagen Group Development to simulate complex geometries with welds and tailored sections in crash simulations. These crash simulations will be performed with shell element models and need to predict the material deformation at high strain rates.

- A common welding method for sheet components in cars is resistance spot welding. The material model should account for the deteriorating effect of the softened heat-affected zone found around spot welds and the differing properties along its length introduced by tailored hardening [11]. This requires expanding the experimental work to investigate different heat treatments and augmenting the material model for not fully-hardened Tribond steel grades.
- For vehicle crash simulations, large components are modeled with a shell element FE model. Shell elements lend themselves perfectly to modeling sheet metal and require less simulation time than a solid element FE model when modeling similar components. Therefore, a shell element material model needs to be calibrated.
- The strain rate dependency should also be investigated and the material model augmented to account for this. The current model is calibrated for a quasi-static strain rate.

CONFIDENTIAL

## Appendix A

### Determination of the Lankford coefficients

To quantify the amount of anisotropy in a material, the Lankford coefficient is used. The Lankford coefficient is a ratio of plastic strains, also known as the  $r$ -value. The Lankford coefficients are calculated for Tribond from the uni-axial tensile test results extracted in  $0^\circ$ ,  $45^\circ$  and  $90^\circ$  angles to the sheet rolling direction. The  $r$ -values are calculated by:

$$r_\alpha = \frac{\varepsilon_{p,w}}{\varepsilon_{p,t}} \quad (\text{A.1})$$

in which  $\alpha$  represents the angle to the sheet rolling direction at which the specimens were removed from the sheet, so  $0^\circ$ ,  $45^\circ$  and  $90^\circ$ . The two strains are the true plastic strains in the width and thickness direction, the axial direction is the tensile test drawing direction.

To calculate the  $r$ -values, the measured strain fields of the uni-axial tensile tests are used. For the uni-axial tension stress state, the only non-zero stress is the true axial stress  $\sigma_{ax}$ . The strain field results are calculated in Aramis from the 2D DIC data measured during testing. Aramis gives the true total strains in axial ( $\varepsilon_{ax}$ ) and width ( $\varepsilon_w$ ) direction on the front surface of the specimen. The true elastic strains in axial ( $\varepsilon_{e,ax}$ ) and width ( $\varepsilon_{e,w}$ ) directions are:

$$\varepsilon_{e,ax} = \frac{1}{E} [\sigma_{ax} - \nu (\sigma_t + \sigma_w)] = \frac{\sigma_{ax}}{E} \quad (\text{A.2})$$

$$\varepsilon_{e,w} = \frac{1}{E} [\sigma_w - \nu (\sigma_{ax} + \sigma_t)] = -\nu \frac{\sigma_{ax}}{E} \quad (\text{A.3})$$

where  $E$  is the Young's modulus and  $\nu$  is the Poisson's ratio. For Tribond these are:

$$E = 190 \text{ GPa}, \nu = 0.3.$$

With the total and elastic true strain known, the plastic true strains in axial ( $\varepsilon_{p,ax}$ ) and width ( $\varepsilon_{p,w}$ ) directions can be calculated. These are:

$$\varepsilon_{p,ax} = \varepsilon_{ax} - \varepsilon_{e,ax} \quad (\text{A.4})$$

$$\varepsilon_{p,w} = \varepsilon_w - \varepsilon_{e,w} \quad (\text{A.5})$$

Assuming plastic incompressibility, the true plastic strain in thickness direction ( $\varepsilon_{p,t}$ ) can be calculated. This is:

$$\varepsilon_{p,t} = -\varepsilon_{p,ax} - \varepsilon_{p,w} \quad (\text{A.6})$$

Now Equation A.1 can be solved. Figure A.1 shows the  $r$ -values in all three specimen directions plotted over the true plastic axial strain. The results level out as the true strain increases, because the  $r$ -value is initially a ratio of two very small values which makes it more sensitive to the measurement accuracy. The values after the cutoff are used to calculate the mean  $r$ -values. Table A.1 shows the mean values and standard deviations for the different specimen directions.

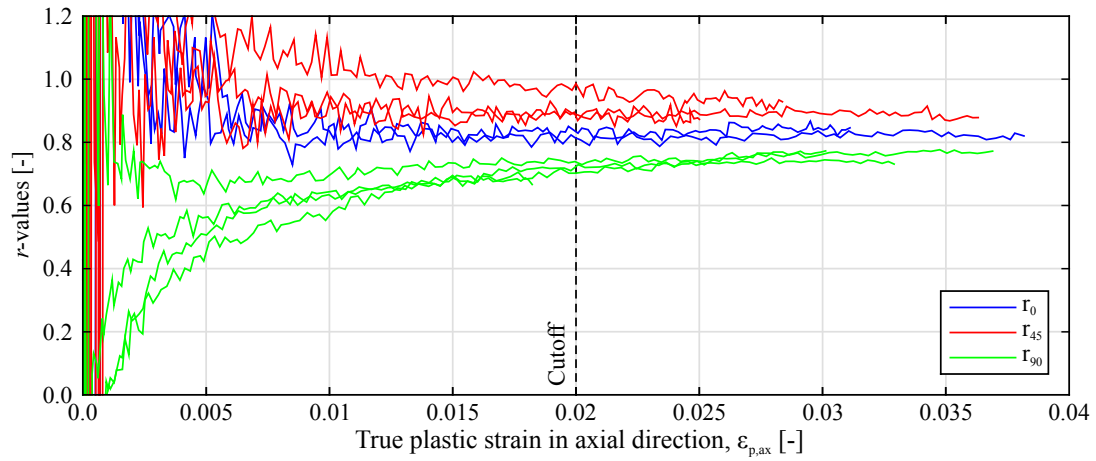


**Figure A.1** The calculated  $r$ -values for specimens extracted at  $0^\circ$ ,  $45^\circ$  and  $90^\circ$  angles relative to the sheet rolling direction.

**Table A.1** The mean  $r$ -values and standard deviations for the three different specimen directions after the cutoff,  $\epsilon_{p,ax} = 0.02$ .

	$r_0$	$r_{45}$	$r_{90}$
Mean	0.812	0.903	0.746
SD	0.073	0.081	0.009

## Appendix B

### Determination of the true stress–true equivalent plastic strain

In this appendix, the method for calculating the true stress and true equivalent plastic strain from the measured force–displacement data is described. It also extends to the true stress–true equivalent plastic strain calculation for the hardening curve. The true stress  $\sigma$  is defined as:

$$\sigma = \frac{F}{A}. \quad (\text{B.1})$$

Using the definition for the engineering stress, this can be rewritten:

$$\sigma = \frac{F}{A} \cdot \frac{A_0}{A_0} = \frac{F}{A_0} \cdot \frac{A_0}{A} = \sigma_{\text{eng}} \cdot \frac{A_0}{A}. \quad (\text{B.2})$$

Assuming incompressibility gives:

$$Al = A_0l_0 \rightarrow \frac{A_0}{A} = \frac{l}{l_0}. \quad (\text{B.3})$$

Together this gives:

$$\sigma = \sigma_{\text{eng}} \cdot \frac{l}{l_0} = \sigma_{\text{eng}} \left( \frac{l_0 + \Delta l}{l_0} \right) = \sigma_{\text{eng}} \left( 1 + \frac{\Delta l}{l_0} \right). \quad (\text{B.4})$$

Here, the engineering strain can be recognized. This gives for the true stress:

$$\sigma = \sigma_{\text{eng}} (1 + \epsilon) \quad (\text{B.5})$$

in which  $\epsilon$  is the engineering strain. The true strain, also called the logarithmic strain, is calculated with:

$$\epsilon = \ln(1 + \epsilon). \quad (\text{B.6})$$

For the calculation of the hardening curve, the true equivalent plastic strain needs to be known. This is:

$$\bar{\epsilon}_p = \bar{\epsilon} - \bar{\epsilon}_e \quad (\text{B.7})$$

in which the true equivalent elastic strain  $\bar{\epsilon}_e$  is defined as:

$$\bar{\epsilon}_e = \frac{\sigma}{E} \quad (\text{B.8})$$

This gives for the true equivalent plastic strain:

$$\bar{\epsilon}_p = \ln(1 + \epsilon) - \frac{\sigma}{E} \quad (\text{B.9})$$



Appendix C  
Specimen drawings

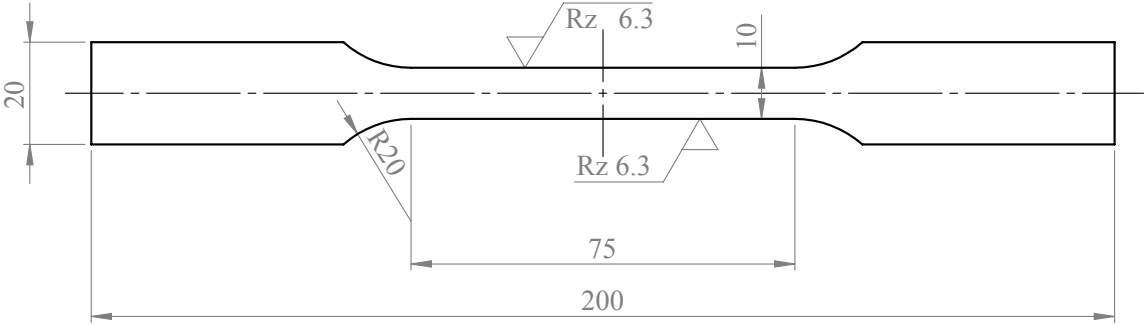


Figure C.1 Uni-axial tensile test specimen geometry (dimensions in mm).

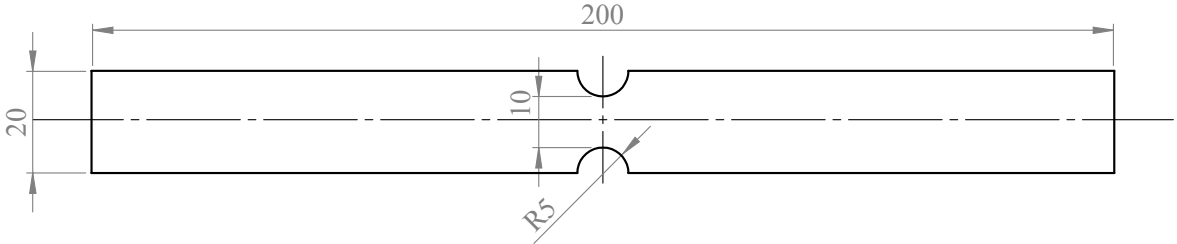


Figure C.2 Notched tensile test specimen geometry (dimensions in mm).

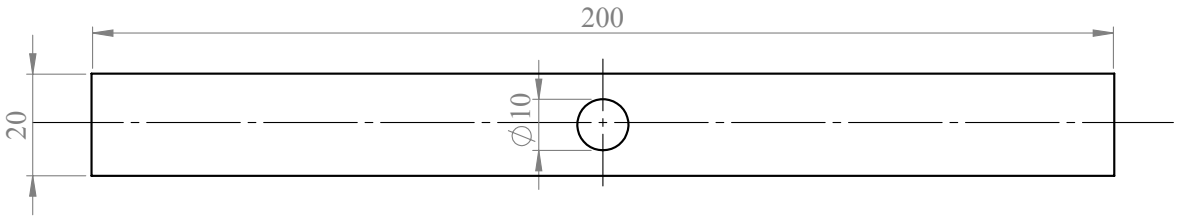
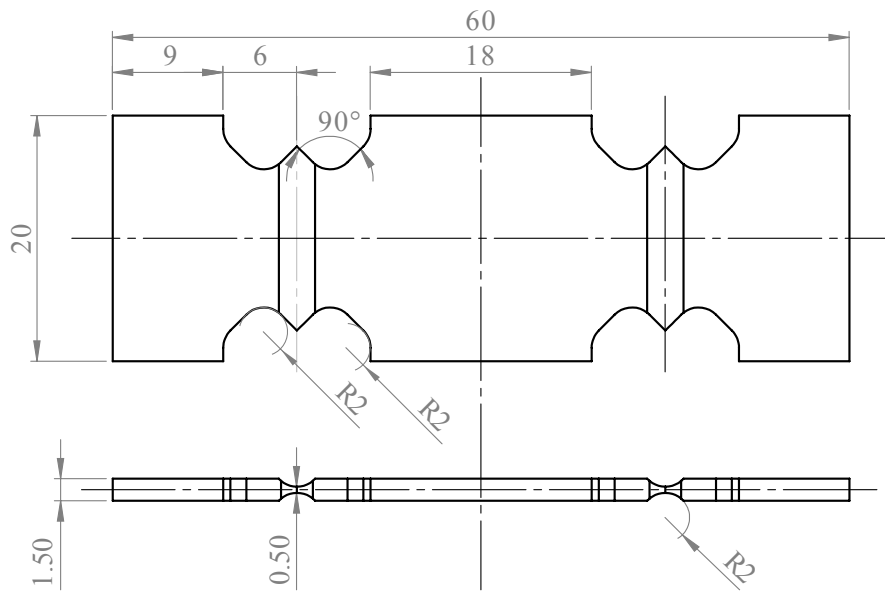
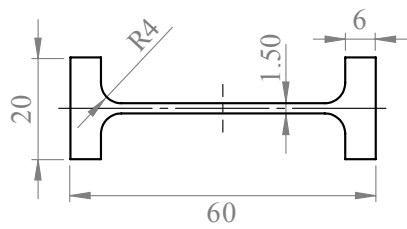


Figure C.3 Central hole tensile test specimen geometry (dimensions in mm).



**Figure C.4** Shear test specimen geometry (dimensions in mm).



**Figure C.5** Narrow 3-point bending test specimen geometry (dimensions in mm).

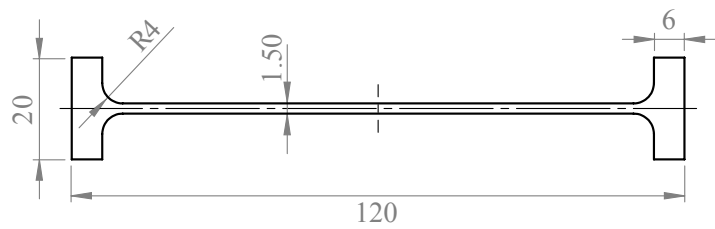


**Figure C.6** Narrow buckling bending test specimen geometry (dimensions in mm).

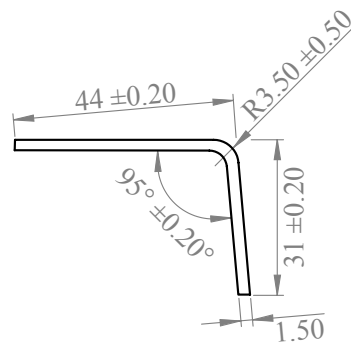


**Figure C.7** L-section compression test specimen cross section (dimensions in mm). Total length was 120 mm.

**Appendix D**  
**Test setup images**

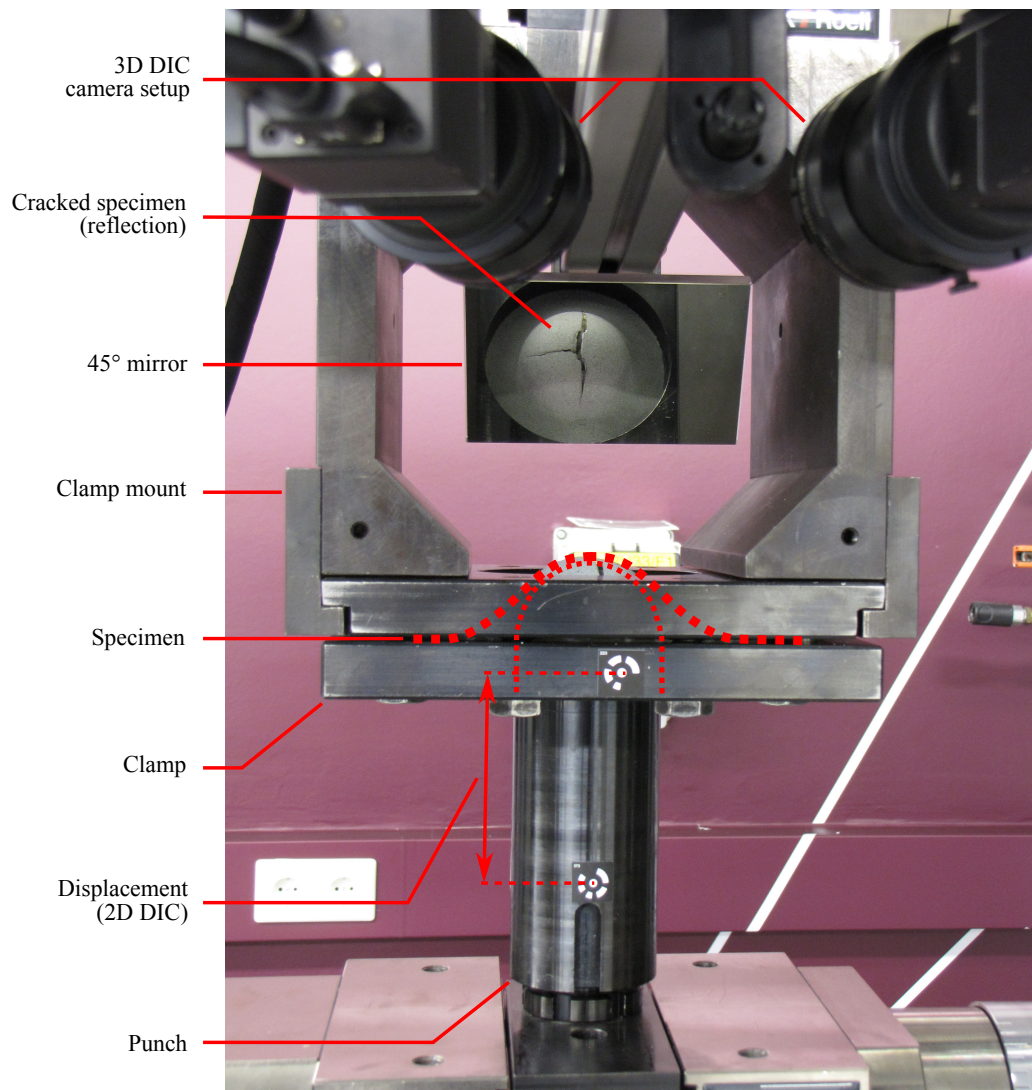


**Figure D.1** *Picture of the bulge test with 3D DIC camera setup and mirror to capture the strain fields, adapted from Eller [11].*

## Appendix E

### Stress state traces of the BE20 test

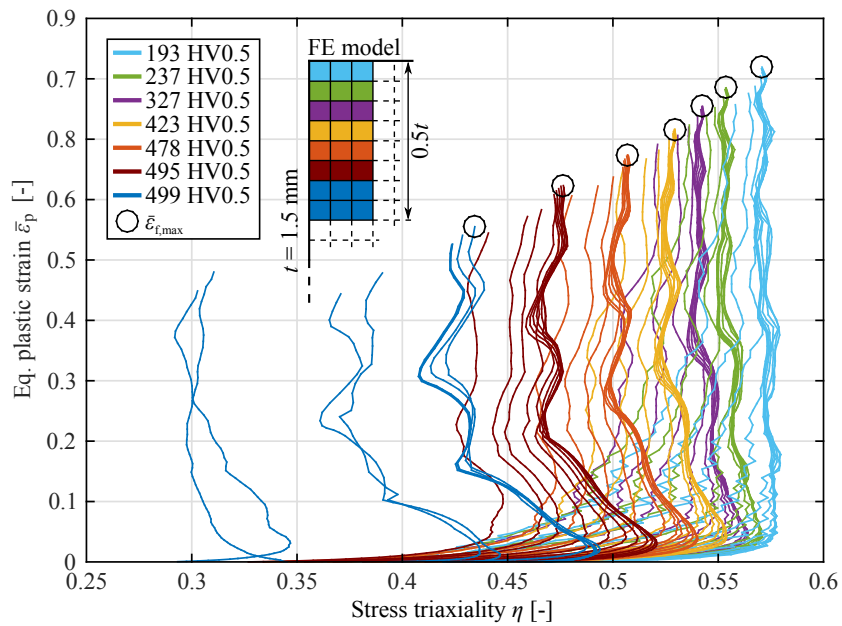


**Figure E.1** Simulated stress state traces of the BE20 fracture candidates in the  $(\eta, \bar{\epsilon}_p)$ -plane. Separated according to their hardness properties, circled is the maximum fracture strain of each set of traces.

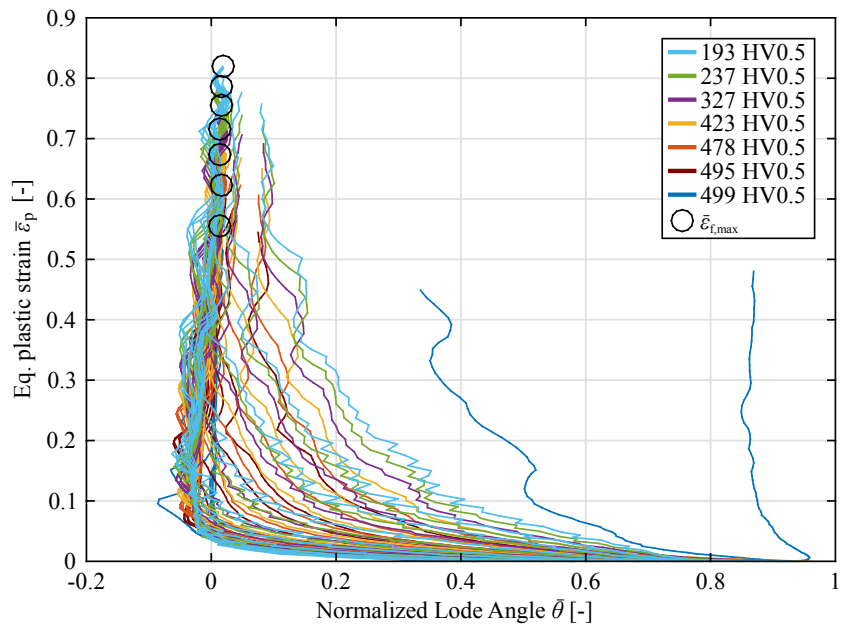


**Figure E.2** Simulated stress state traces of the BE20 fracture candidates in the  $(\bar{\theta}, \bar{\epsilon}_p)$ -plane. Separated according to their hardness properties, circled is the maximum fracture strain of each set of traces.

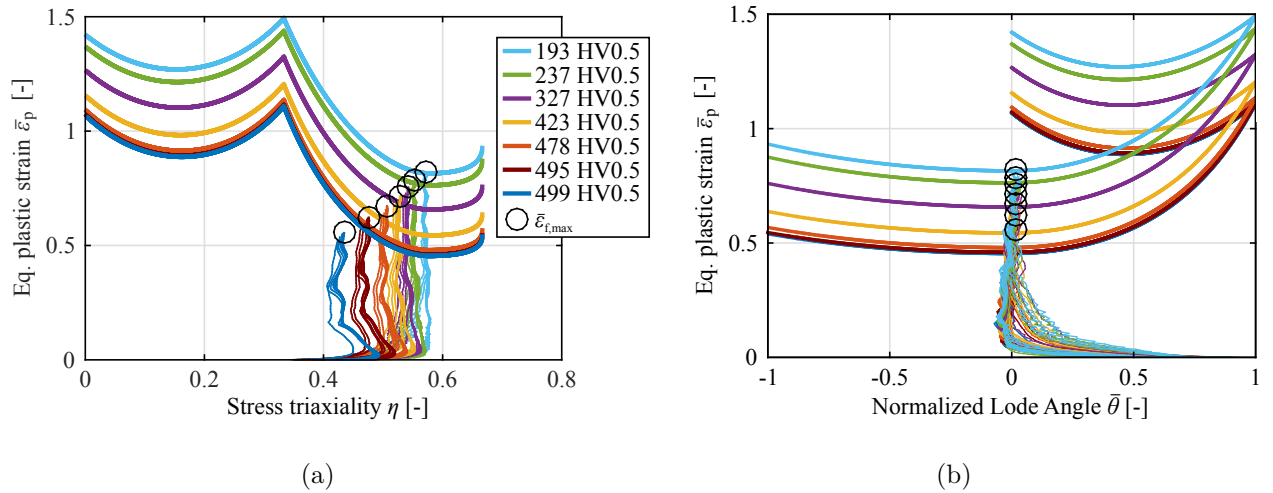


**Figure E.3** Plane stress fracture curves for all hardness layers of a 0.1 mm mesh and linear mixing rule, with the stress state traces in the  $(\eta, \bar{\epsilon}_p)$ -plane (a) and the  $(\bar{\theta}, \bar{\epsilon}_p)$ -plane (b).

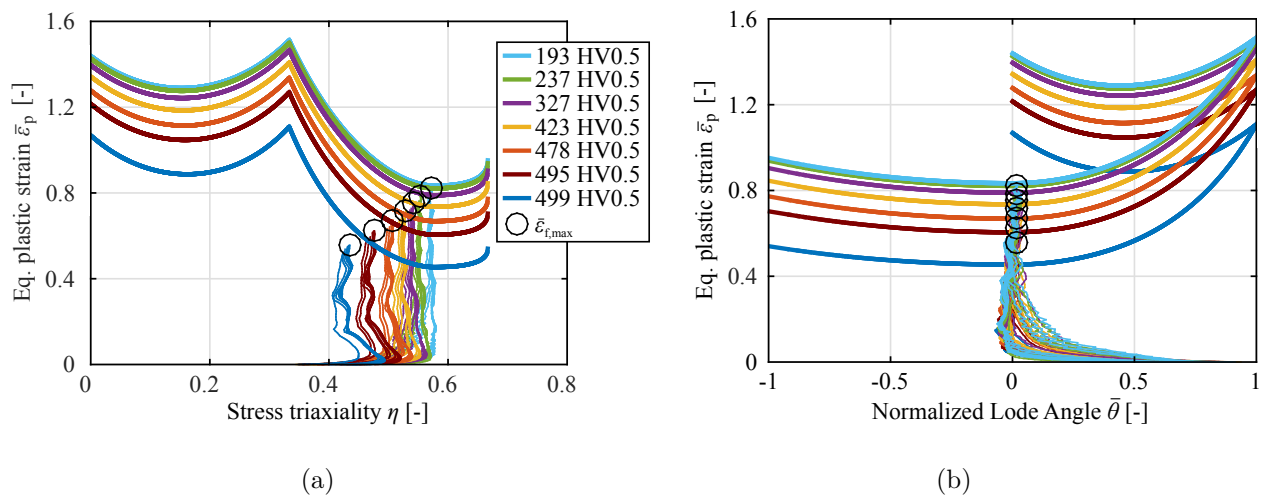


**Figure E.4** Plane stress fracture curves for all hardness layers of a 0.1 mm mesh and non-linear mixing rule, with the stress state traces in the  $(\eta, \bar{\epsilon}_p)$ -plane (a) and the  $(\bar{\theta}, \bar{\epsilon}_p)$ -plane (b).

CONFIDENTIAL

Appendix F  
Fracture plots

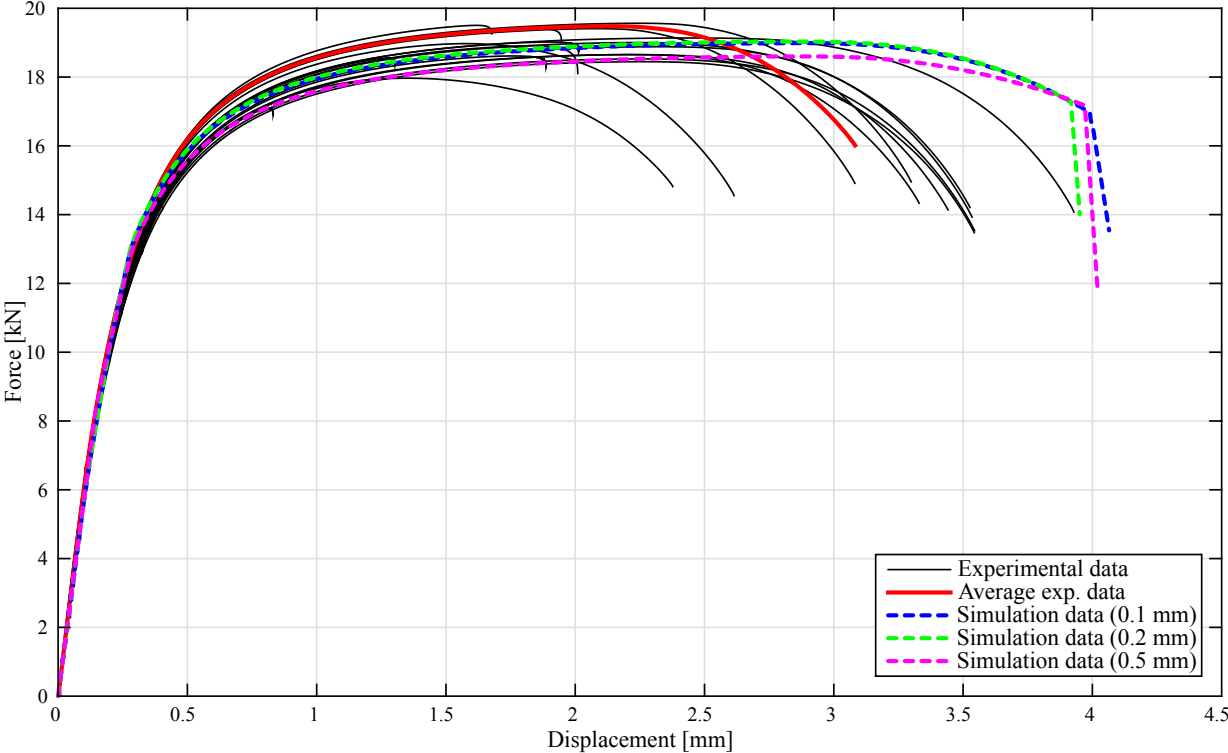
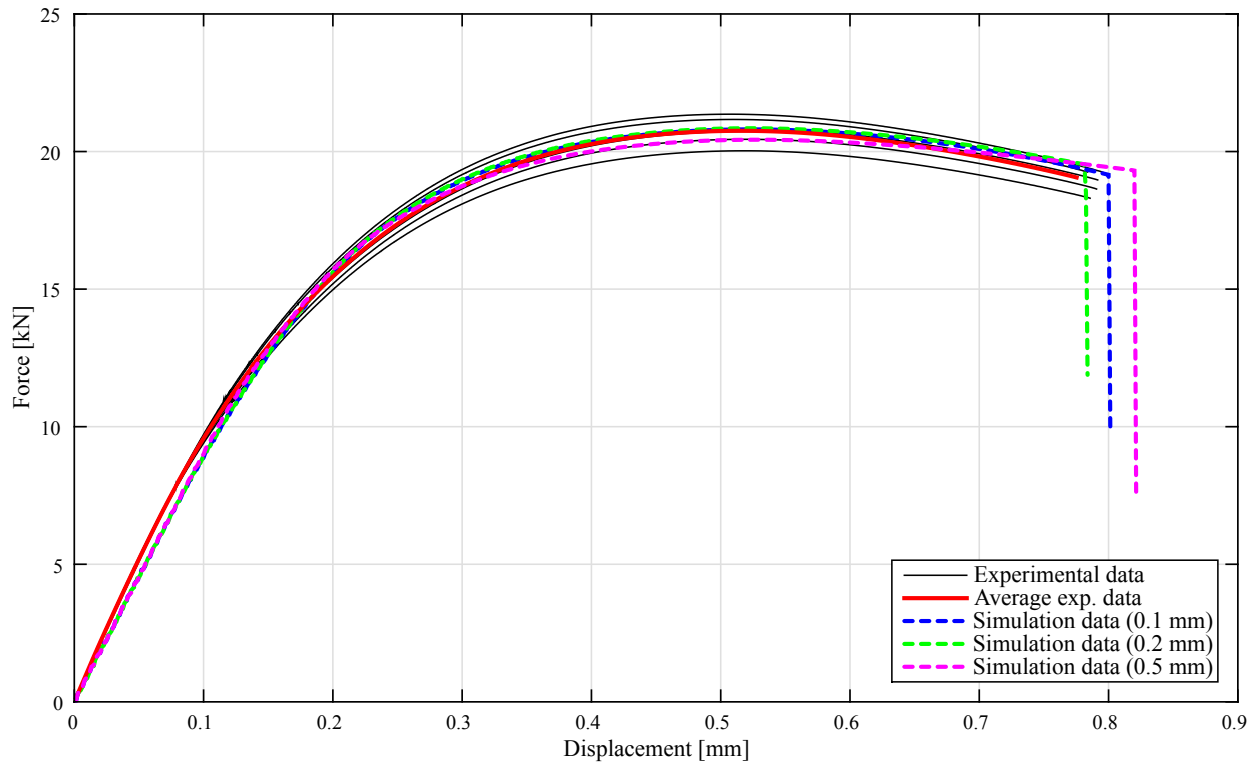
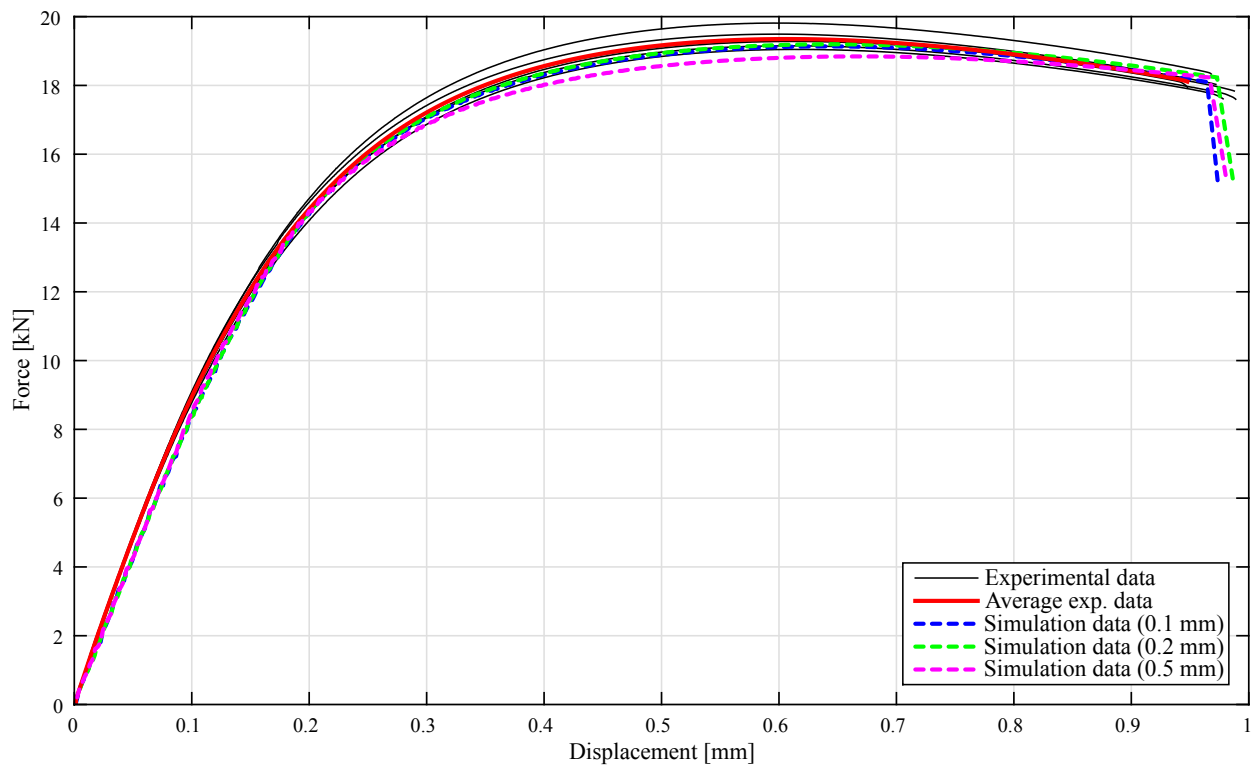


Figure F.1 Simulation results of the uni-axial tensile test for 0.1 mm, 0.2 mm and 0.5 mm mesh sizes.



**Figure F.2** Simulation results of the notched tensile test for 0.1 mm, 0.2 mm and 0.5 mm mesh sizes.



**Figure F.3** Simulation results of the central hole tensile test for 0.1 mm, 0.2 mm and 0.5 mm mesh sizes.

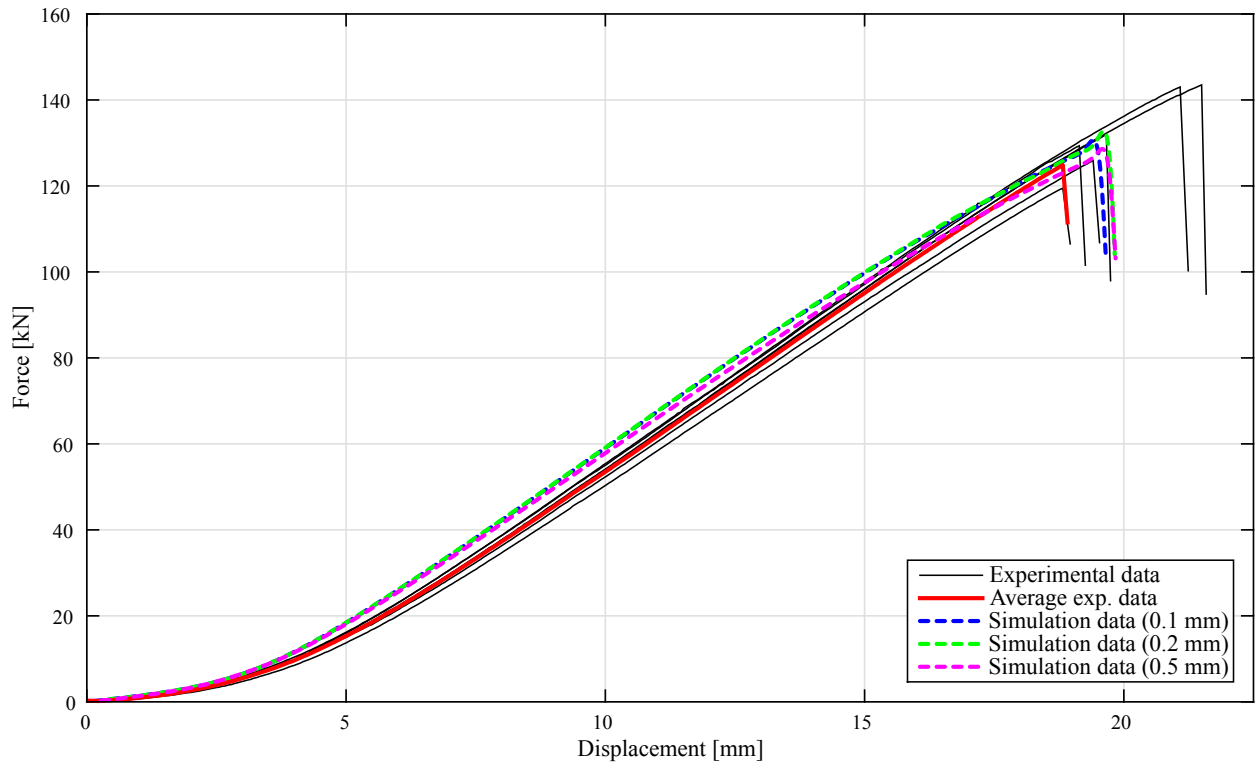


**Figure F.4** Simulation results of the bulge test for 0.1 mm, 0.2 mm and 0.5 mm mesh sizes.

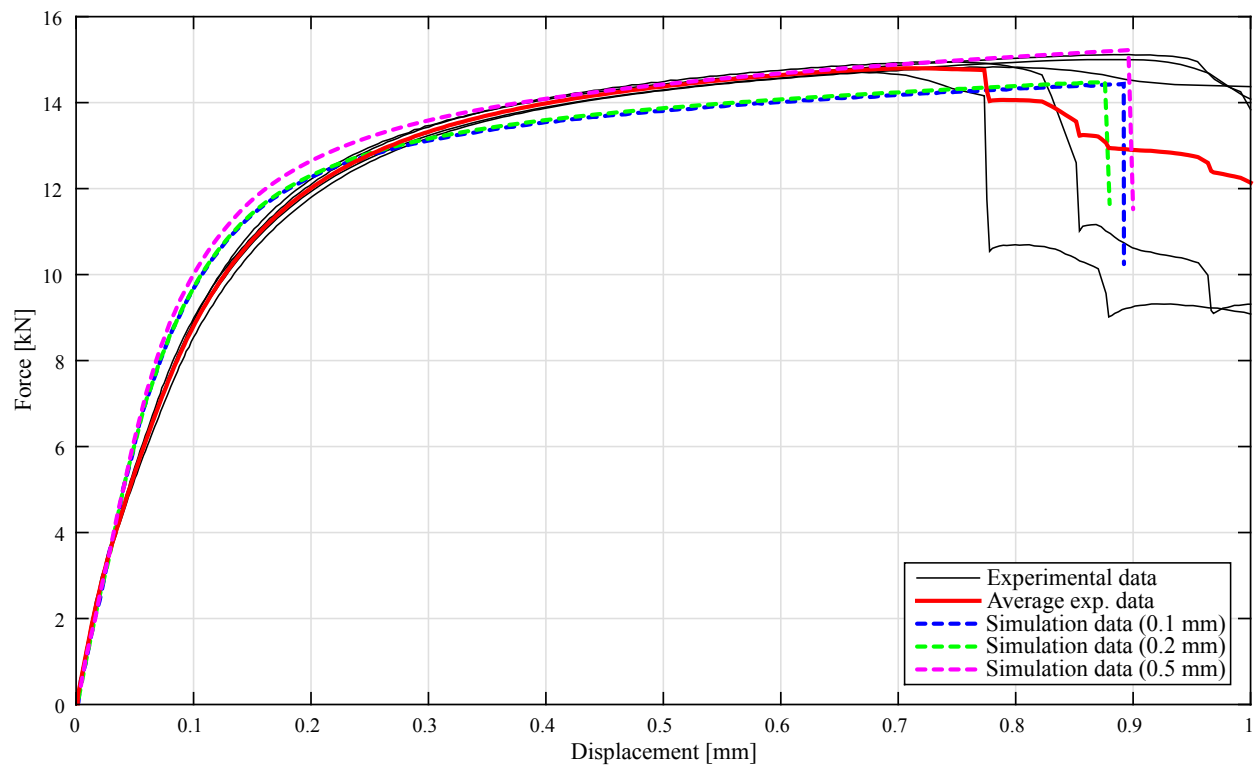


**Figure F.5** Simulation results of the shear test for 0.1 mm, 0.2 mm and 0.5 mm mesh sizes.

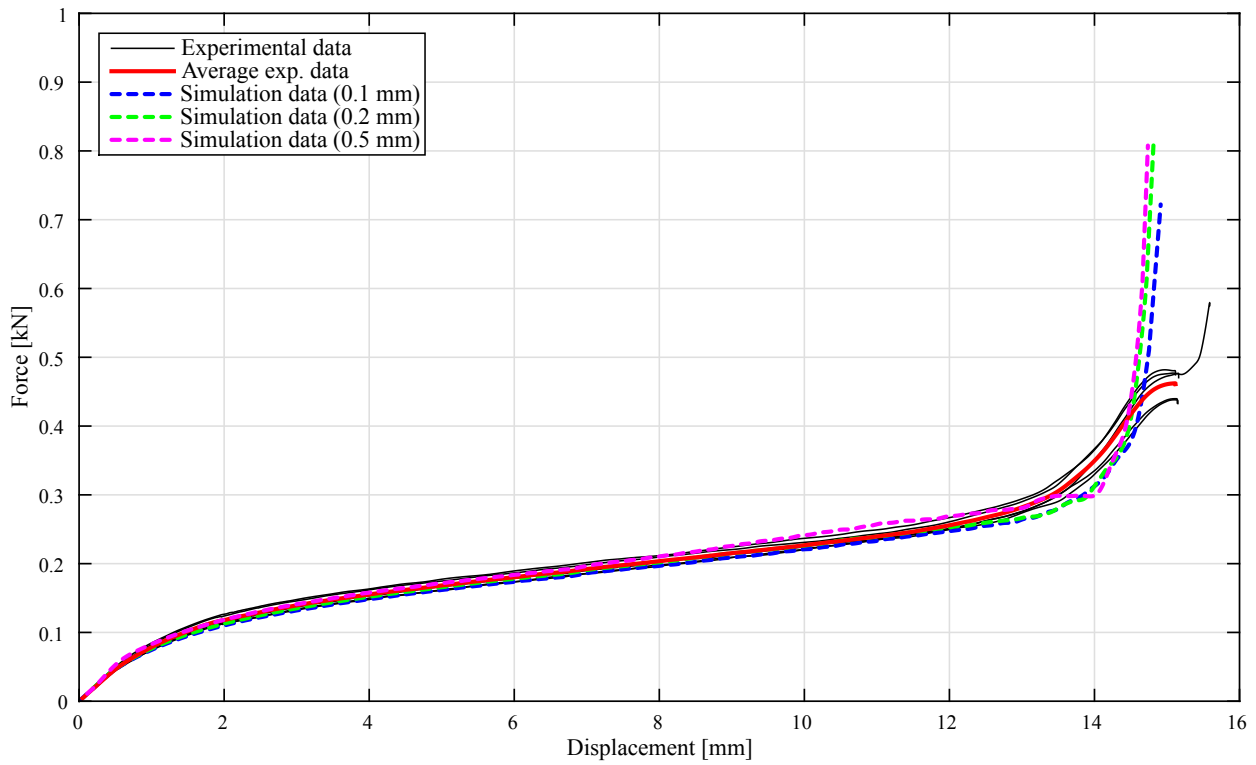


**Figure F.6** Simulation results of the narrow specimen 3-point bending test for 0.1 mm, 0.2 mm and 0.5 mm mesh sizes.

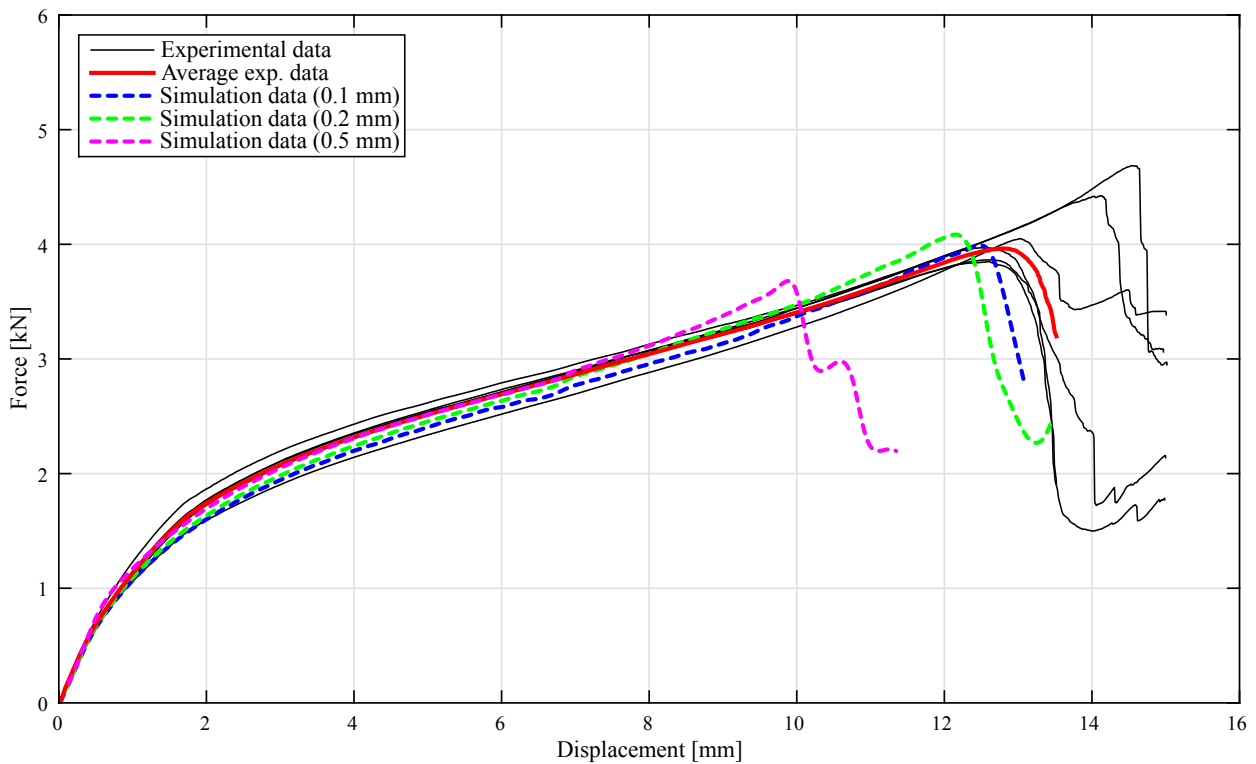


**Figure F.7** Simulation results of the wide specimen 3-point bending test for 0.1 mm, 0.2 mm and 0.5 mm mesh sizes.

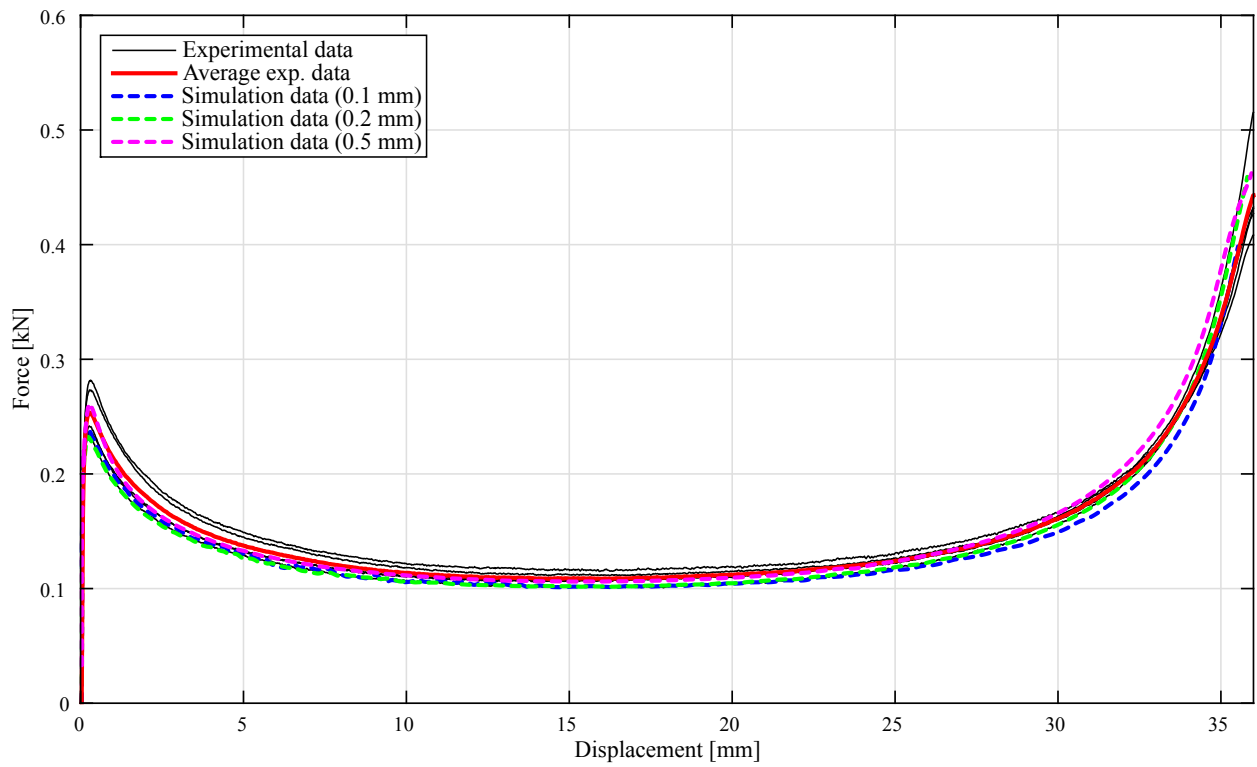


**Figure F.8** Simulation results of the narrow specimen buckling bending test for 0.1 mm, 0.2 mm and 0.5 mm mesh sizes.

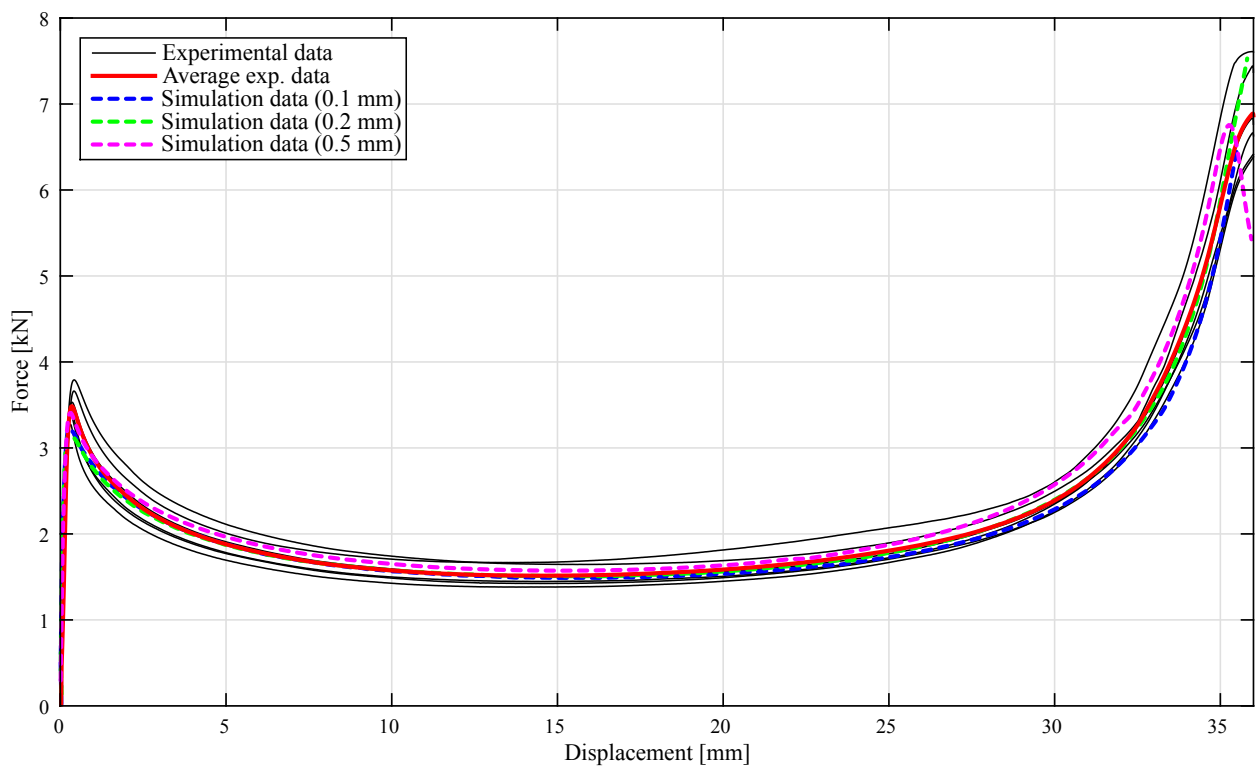


**Figure F.9** Simulation results of the wide specimen buckling bending test for 0.1 mm, 0.2 mm and 0.5 mm mesh sizes.



# Appendix G

## Fracture models

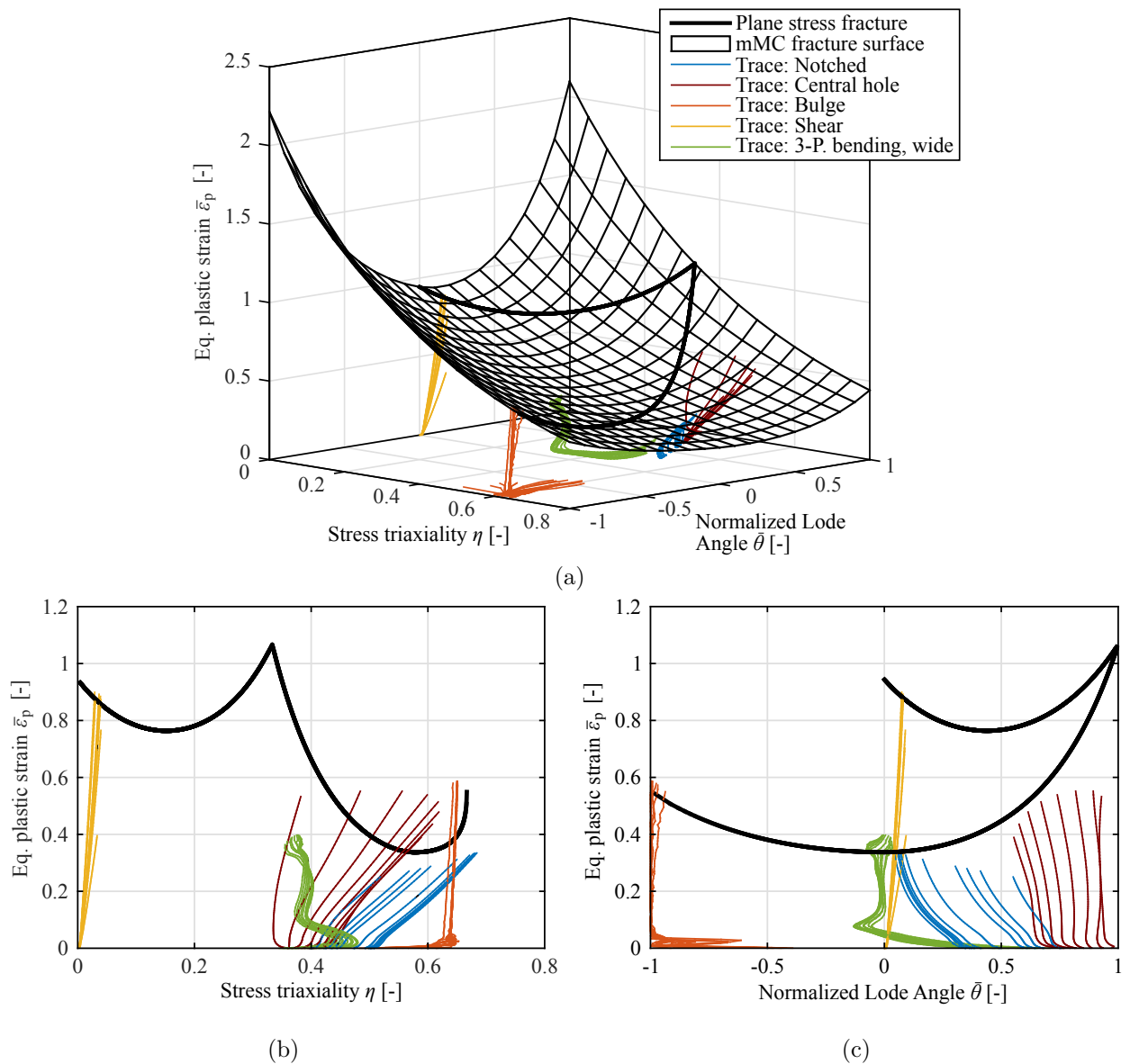


**Figure G.1** Calibrated core layer mMC fracture surface for a 0.2 mm mesh (a) and the plane stress fracture curve in the  $(\eta, \bar{\epsilon}_p)$ -plane (b) and the  $(\bar{\theta}, \bar{\epsilon}_p)$ -plane (c). With stress state traces of the candidate elements.

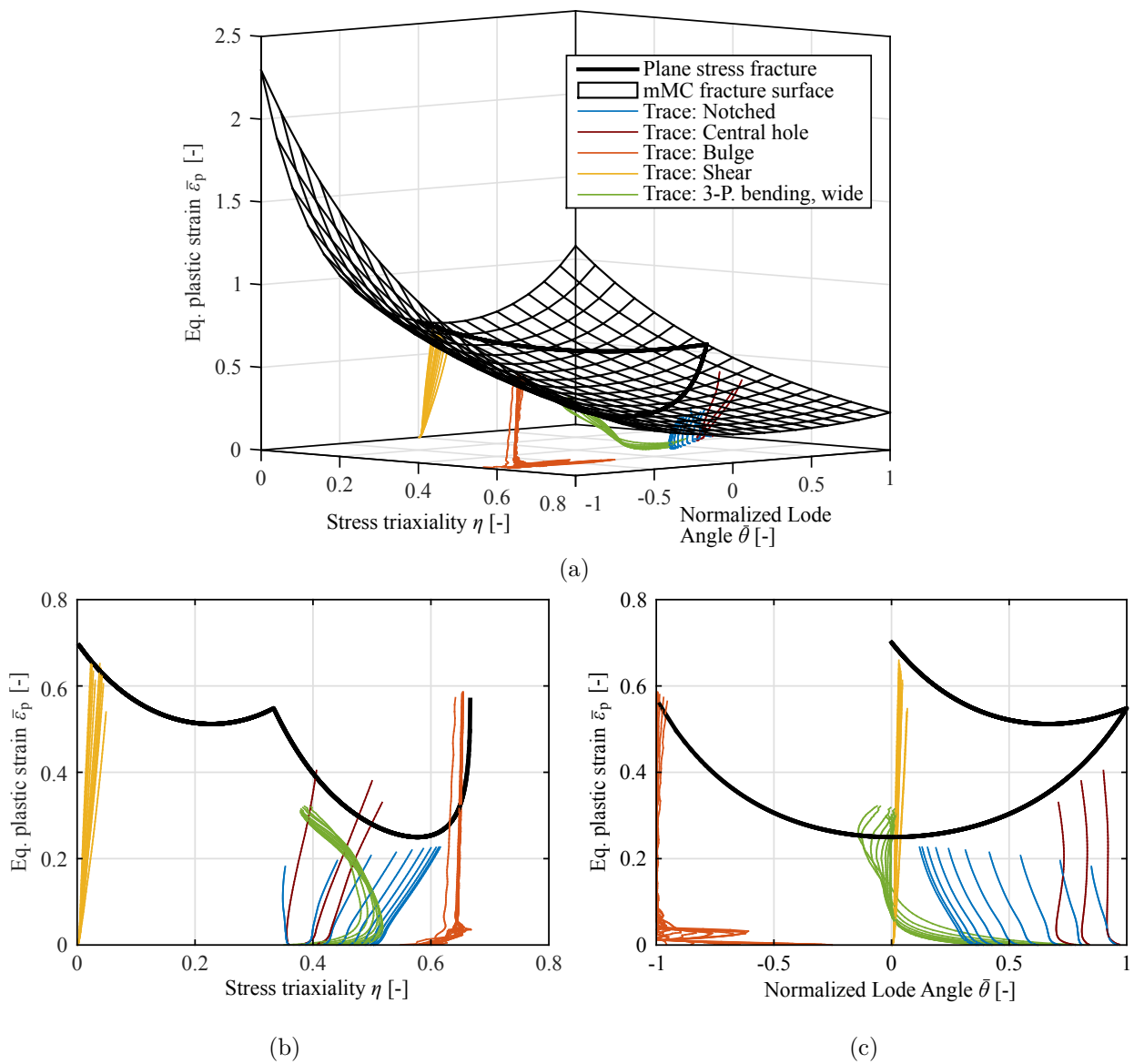


**Figure G.2** Calibrated core layer mMC fracture surface for a 0.5 mm mesh (a) and the plane stress fracture curve in the  $(\eta, \bar{\epsilon}_p)$ -plane (b) and the  $(\bar{\theta}, \bar{\epsilon}_p)$ -plane (c). With stress state traces of the candidate elements.

Appendix H

Side-by-side comparison L-section compression test

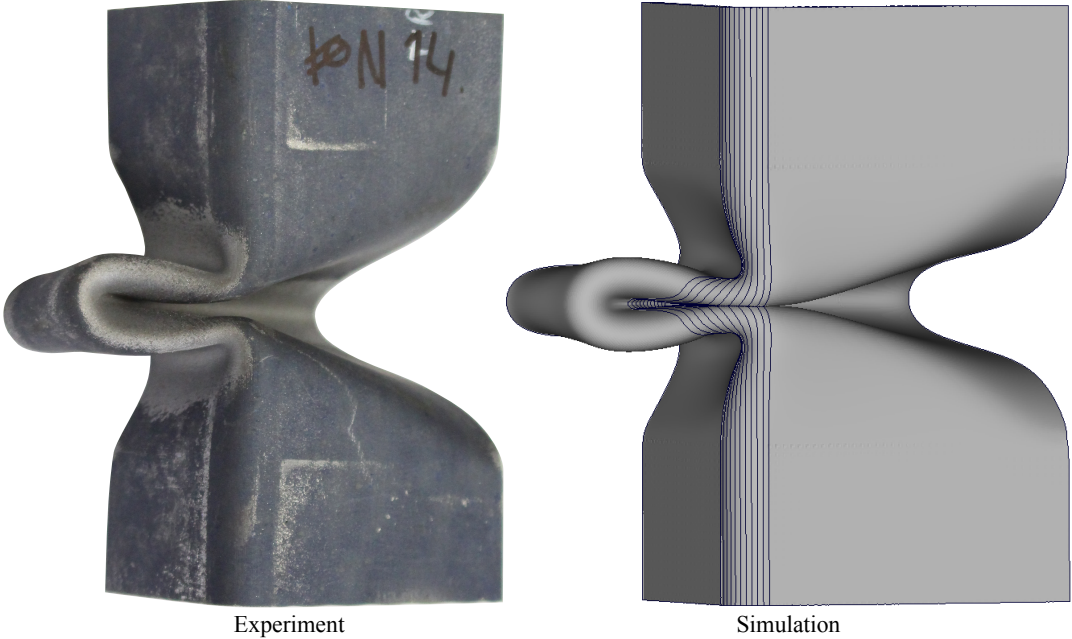


**Figure H.1** *Front view: side-by-side comparison of the compressed specimen and straight base plate FE model with an 0.2 mm mesh and SRI.*

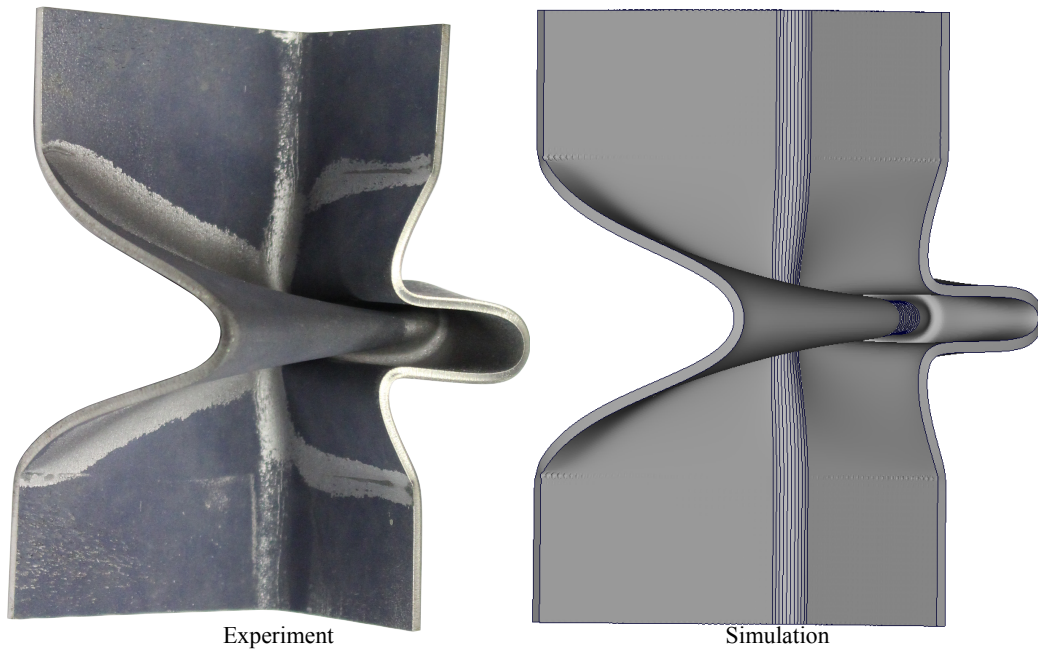


**Figure H.2** Rear view: side-by-side comparison of the compressed specimen and straight base plate FE model with an 0.2 mm mesh and SRI.

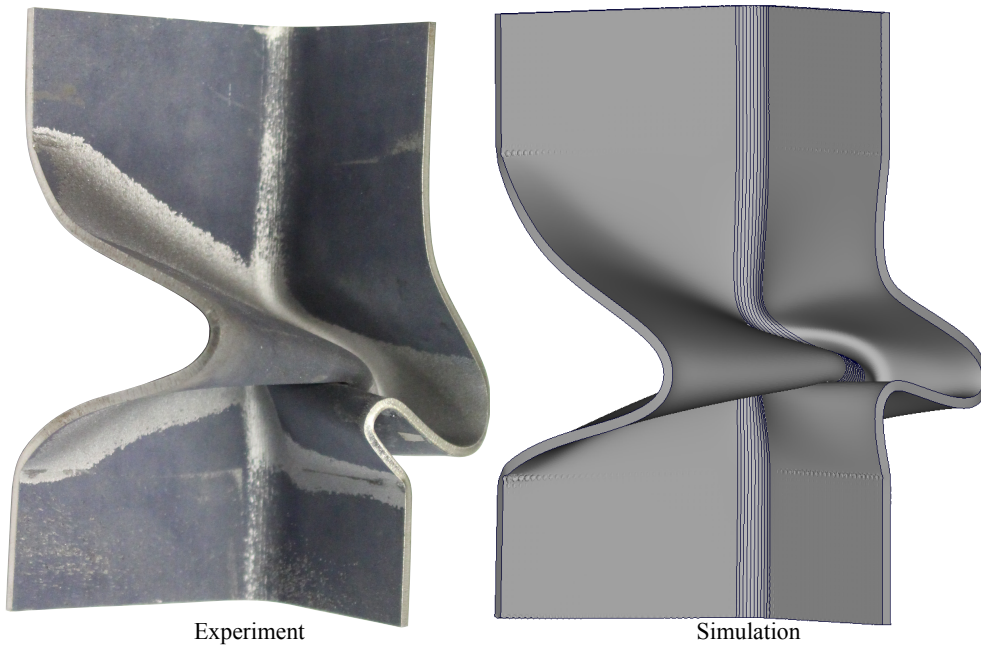


**Figure H.3** Rear view: side-by-side comparison of the asymmetrically folded, compressed specimen and rotated base plate FE model with an 0.2 mm mesh and SRI.

# Bibliography

- [1] Alloyed Quenched and Tempered Steel for Press Quenching – Uncoated or Pre-Coated. *Volkswagen Group Standard TL 4225*, Issue 2016–04.
- [2] Thyssenkrupp Steel Europe AG (2014). Manganese-boron steels MBW, for hot forming.
- [3] Thyssenkrupp Steel Europe AG (2015). Brochure for high-strength and high-ductile steel composite, Tribond.
- [4] Thyssenkrupp Steel Europe AG (2016). Product information for high-strength and high-ductile steel composite, Tribond.
- [5] Bai, Y. (2008). *Effect of Loading History on Necking and Fracture*. PhD thesis, Massachusetts Institute of Technology.
- [6] Bai, Y. and Wierzbicki, T. (2008). A new model of metal plasticity and fracture with pressure and Lode dependence. *International Journal of Plasticity*, 24:1071–1096.
- [7] Bai, Y. and Wierzbicki, T. (2010). Application of extended Mohr-Coulomb criterion to ductile fracture. *International Journal of Fracture*, 161:1–20.
- [8] Barlat, F., Brem, J. C., Yoon, J. W., Chung, K., Dick, R. E., Lege, D. J., Pourboghrat, F., Choi, S.-H., and Chu, E. (2003). Plane stress yield function for aluminum alloy sheets - part 1: theory. *International Journal of Plasticity*, 19:1297 – 1319.
- [9] Becker, J. U. and Myslowicki, S. (2013). Stahlverbundwerkstoff Tribond. Thyssenkrupp Steel Europe AG presentation, Duisburg.
- [10] Christensen, R. M. (2008). Note: Observations on the definition of yield stress. *Acta Mech*, 196:239–244.
- [11] Eller, T. K. (2016). *Modeling of tailor hardened boron steel for crash simulation*. PhD thesis, University of Twente.
- [12] Eller, T. K., Greve, L., Andres, M. T., Medricky, M., Hatscher, A., Meinders, V. T., and van den Boogaard, A. H. (2014). Plasticity and fracture modeling of quench-hardenable boron steel with tailored properties. *Journal of Materials Processing Technology*, 214:1211–1227.
- [13] Eller, T. K., Greve, L., Andres, M. T., Medricky, M., Meinders, V. T., and van den Boogaard, A. H. (2016). Determination of strain hardening parameters of tailor hardened boron steel up to high strains using inverse FEM optimization and strain field matching. *Journal of Materials Processing Technology*, 228:43–58.
- [14] Flanagan, D. P. and Belytschko, T. (1981). A uniform strain hexahedron and quadrilateral with orthogonal hourglass control. *International Journal for Numerical Methods in Engineering*, 17:679–706.
- [15] George, R., Bardelcik, A., and Worswick, M. J. (2012). Hot forming of boron steels using heated and cooled tooling for tailored properties. *Journal of Materials Processing Technology*, 212:2386–2399.
- [16] Greve, L. (2012). Modulare Materialmodellierung für die Simulation von Deformations- und Bruchvorgängen. In *CrashMAT Conference 2012–6. Freiburg Workshop zum Werkstoff- und Strukturverhalten bei Crashvorgängen*.

- [17] Haddadi, H. and Belhabib, S. (2012). Improving the characterization of a hardening law using digital image correlation over an enhanced heterogeneous tensile test. *International Journal of Mechanical Sciences*, 62:47–56.
- [18] Henn, P. (2015a). Statusbericht zum Promotionsprojekt Duktilitätscharakterisierung. Audi AG – Neckarsulm.
- [19] Henn, P. (2015b). Validierung von Materialmodellen zur Charakterisierung des Werkstoffversagens von Aluminiumlegierungen. Master’s thesis, Universität Stuttgart.
- [20] Hershey, A. (1954). The plasticity of an isotropic aggregate of anisotropic face centred cubic crystals. *Journal of Applied Mechanics*, 21:241–249.
- [21] Hill, R. (1948). A theory of the yielding and plastic flow of anisotropic metal. In *Proceedings of the Royal Society, Series A*. 193:281–297.
- [22] Höhle, S. (2013). Influence of material modelling parameters on the prediction of bending loads in sheet metal forming simulation. *Advanced Materials Research*, 769:165–173.
- [23] Hosford, W. F. (1972). A Generalized Isotropic Yield Criterion. *Journal of Applied Mechanics*, 39:607–609.
- [24] Karbasian, H. and Tekkaya, A. E. (2010). A review on hot stamping. *Journal of Materials Processing Technology*, 210:2103–2118.
- [25] Linares Arregui, I. and Alfredsson, B. (2013). Non-linear elastic characterisation of a high strength bainitic roller bearing steel. *International Journal of Mechanical Sciences*, 68:1–15.
- [26] Mohr, D. and Ebnoether, F. (2009). Plasticity and fracture of martensitic boron steel under plane stress conditions. *International Journal of Solids and Structures*, 46:3535–3547.
- [27] Pieronek, D. and Myslowicki, S. (2014). Tribond: Simulationsmethode für die Crashsimulation, konvertierung nach PAM-Crash. Thyssenkrupp Steel Europe AG presentation, Dortmund.
- [28] Roth, C. C. and Mohr, D. (2016). Ductile fracture experiments with locally proportional loading histories. *International Journal of Plasticity*, 79:328–354.
- [29] Suehiro, M., Kusumi, K., Miyakoshi, T., Maki, J., and Ohgami, M. (2003). Properties of Aluminium-coated Steels for Hot-forming. *Nippon Steel Technical Report*, 88:295–415.
- [30] Swift, H. (1952). Plastic instability under plane stress. *Journal of the Mechanics and Physics of Solids*, 1:1–18.
- [31] VDA (2010). Plate bending test for metallic materials. *VDA 238-100*.
- [32] Voce, E. (1955). A practical strain-hardening function. *Metallurgica*, 51:219–226.

# Acknowledgments

The work presented in this master thesis was performed at the headquarters of the Volkswagen Group located in Wolfsburg, Germany. This work is performed in partial fulfillment of the requirements for the degree: Master of Science in Mechanical Engineering. The work was performed in collaboration with the University of Twente in Enschede, The Netherlands.

I would like to express my gratitude to the University of Twente and Volkswagen Group for the opportunity to learn and work at the Volkswagen Group Research. Many individuals from both facilitated me during my thesis, the quality of this report is for a large part the result of their efforts. I wish I could thank everyone, but I will have to settle for thanking those whose help I could not have done without.

First of all, I would like to thank my supervisors Dr. Ir. Tom Eller (Volkswagen AG) and Dr. Ir. Javad Hazrati (University of Twente). Tom, your knowledge of material science and clear explanations really taught me a lot and your diligence allowed me to keep working and meant the research always kept moving forwards. Javad, your academic and insightful perspective lead to meaningful research and I truly appreciate the effort you made to guide me, regardless of the distance between Enschede and Wolfsburg. I am indebted to you both for your valuable review of my final work. I must also thank my colleagues Dr. Michael Andres and Dr.-Ing. Lars Greve (Volkswagen AG). Michael, I am always amazed at your knowledge of the modeling procedures and skill at programming, your efforts meant that any new idea or modeling method was quickly implemented and ready for use. Lars, your extensive knowledge of material science are a boon for all around you and after presenting the final results to you, I got a much better understanding of those results. I must also thank Prof. Dr. Ir. Ton van den Boogaard (University of Twente) who is the head of the Chair Nonlinear Solid Mechanics. Ton, thank you for your efforts in arranging my thesis and challenging me during a progress meeting at the University of Twente.

Last, but by no means least, I would like to thank the entire CAE-department at Volkswagen for their support and company, because of you I never felt like I was doing this alone. The support of my family and friends is also deeply appreciated.